BLACK HOLE MASSES, METALLICITIES, AND EMISSION LINE PROPERTIES OF QUASARS

By

CRAIG D. WARNER

A DISSERTATION PRESENTED TO THE GRADUATE SCHOOL
OF THE UNIVERSITY OF FLORIDA IN PARTIAL FULFILLMENT
OF THE REQUIREMENTS FOR THE DEGREE OF
DOCTOR OF PHILOSOPHY

UNIVERSITY OF FLORIDA

2004

Copyright 2004

by

Craig D. Warner

ACKNOWLEDGMENTS

I am grateful to Fred Chaffee, Anca Constantin, Craig Foltz, Vesa Junkkarinen, and Joe Shields for their direct participation in reducing or acquiring some of the ground-based spectra used in this work and to Marianne Vestergaard for providing the UV Fe emission template for this study. I thank Bassem Sabra for his useful comments on some of my manuscripts and for being available when I had questions. I am also thankful to Rafael Guzman, Gary Ihas, Beverly Sanders, and Vicki Sarajedini for being on my committee.

I would like to thank Matthias Dietrich for his endless work in compiling and calibrating our large sample of AGN spectra, his calctemplate fortran program to calculate composite spectra, his many useful comments on our manuscripts and posters, and all the questions he has answered and help he has given me.

I would like to give special thanks to my adviser, Fred Hamann, for all his help and support working with me the past four years. I am grateful to him for getting me started on studying emission lines in quasars, always being available when I had questions, and financial support both as a research assistant and for attending meetings. I am also thankful that because of his many, many useful comments on our manuscripts, by the time they were reviewed, the referees generally had very few revisions to suggest.

I thank Catherine Garland for her comments on some of my manuscripts and her help and support both through classes and during my doctoral research. I am also grateful to Eric McKenzie for his careful proofreading of my manuscripts, his comments on them, and his help and support through classes and during my doctoral research. I would like to thank Kyle Padgett for his help in getting

through undergraduate physics, especially E&M II, and for all of his support the past eight years. Finally, I would like to thank my parents, Richard and April Warner, for all of their support.

I acknowledge financial support from the NSF via grant AST99-84040 and NASA via grant NAG5-3234.

TABLE OF CONTENTS

page

ACKNOWLEDGMENTS iii

LIST OF TABLES viii

LIST OF FIGURES ix

ABSTRACT xvi

CHAPTER

1 INTRODUCTION 1

2 THE METALLICITY OF THE REDSHIFT 4.16 QUASAR BR2248-1242 8

- 2.1 Introduction 8
- 2.2 Data and Analysis 10
- 2.3 Results 15
- 2.4 Discussion 18

3 A RELATION BETWEEN SUPERMASSIVE BLACK HOLE MASS AND QUASAR METALLICITY? 20

- 3.1 Introduction 20
- 3.2 SMBH Mass Determinations 23
- 3.3 Data and Analysis 26
- 3.4 C IV vs. Hβ as a Mass Diagnostic 34
- 3.5 Results 35
  - 3.5.1 SMBH Mass vs. Redshift, Luminosity, and FWHM 35
  - 3.5.2 Line Properties versus SMBH Mass 40
  - 3.5.3 Metallicity versus SMBH Mass 40
  - 3.5.4 Do N III] and N V Disagree? 44
- 3.6 Discussion 46
- 3.7 Summary and Conclusions 48

4 ACTIVE GALACTIC NUCLEI EMISSION-LINE PROPERTIES VERSUS EDDINGTON RATIO 51

- 4.1 Introduction 51
- 4.2 Eddington Ratio Determinations 53
- 4.3 Data and Analysis 56
- 4.4 Results and Comparisons 63

4.4.1 L/L_{edd} and Super-Eddington Accretion 63
4.4.2 Correlations with L/L_{edd} 63
4.4.3 Surprising Emission-Line Behaviors 67
4.4.4 Metallicities 73
4.5 Discussion 76
4.6 Summary and Conclusions 78

5 BLACK HOLE MASSES, METALLICITIES, AND THE BALDWIN EFFECT 81

5.1 Introduction 81
5.2 Data and Analysis 83
5.3 Composite Spectra 85
5.4 Results and Comparisons 89
5.4.1 Metallicities 89
5.4.2 Line Peak Heights and the Baldwin Effect 92
5.5 Discussion 96
5.5.1 BLR Metallicities 96
5.5.2 The Baldwin Effect 98
5.6 Summary and Conclusions 99

6 ON THE RELATIONSHIP BETWEEN METALLICITY AND EMISSION LINE VELOCITY WIDTHS IN AGNS 101

6.1 Introduction 101
6.2 Data & Analysis 103
6.3 Composite Spectra 104
6.4 Results & Discussion 106
6.5 Summary & Conclusions 108

7 SUMMARY AND CONCLUSIONS 110

APPENDICES

A DETAILS OF LINE FITTING PROCEDURE 113

B LINE FITTING WITH GATORPLOT 116

C GATORPLOT DOCUMENTATION 119

C.1 Overview 119
C.2 Plotting Files 121
C.3 Titles, Labels, Symbols, and Offsets 124
C.4 Buttons 125
C.5 GPFIT 128
C.6 Commands, Images, and More 139
C.7 Default Columns, Colors, and Linestyles 142
C.8 More Options 143

C.9 GPScript 145

D DETAILS OF CREATING COMPOSITE SPECTRA 158

E POSTERS 163

REFERENCES 168

BIOGRAPHICAL SKETCH 175

LIST OF TABLES

Table page

2–1 Emission Line Data 12

2–2 Emission Line Components 13

2–3 Emission Line Ratios 15

3–1 Composite Parameters 27

3–2 Emission Line Data 33

4–1 Composite Parameters 59

4–2 Emission Line Data 68

5–1 Composite Parameters 86

6–1 Composite Parameters 105

LIST OF FIGURES

Figure page

2–1 Spectrum of BR2248-1242 with our fit to the continuum overplotted (dashed line). The spectrum has been corrected for extinction. . . . 10

2–2 Gaussian fits of emission lines of BR2248-1242. The continuum is normalized by the power law fit shown in Figure 2-1. The continuum (at unity) and composite line fits are plotted as solid curves. The individual components of the fits are shown as dotted and dashed lines. 12

2–3 Comparison of flux ratios measured in BR2248-1242 to theoretical results from Figure 5 of Hamann et al. (2001). Comparisons of our measured line ratios to the theoretical model represented by the solid line yield our preferred estimates for metallicity. The solid line is obtained from the model in Hamann et al. that uses a segmented powerlaw for the photoionizing continuum shape, which is a good approximation to the average observed continuum in quasars. The dotted line corresponds to the model that uses an incident spectrum defined by Matthews & Ferland (1987), while the dashed line corresponds to a powerlaw with index $\alpha = -1.0$ across the infrared through X-rays 16

3–1 Normalized composite spectra are shown for all five SMBH mass bins. The spectra were normalized by a power law continuum fit. The horizontal dashed lines indicate the continuum level for the individual normalized composite spectra, which were vertically shifted for better display. The normalized continuum strength is shown for the spectrum at the bottom of the figure. This same vertical scale applies to all other spectra, although the tick marks for '0' and '1' are not labelled. The mean SMBH mass of each spectra is listed to the right. The Baldwin Effect is clearly seen in these spectra. . . . 30

3–2 Same as Fig. 3-1, but with an expanded vertical scale to display the dependence of the relative strength of weaker emission lines as a function of SMBH mass. Strong emission lines with flat tops are truncated for easier display. 31

3–3 Multi-component Gaussian fits (smooth solid curves) to observed emission lines (jagged solid curves) for a composite spectrum of $M \sim 10^8$ $M_\odot$. The continuum is normalized by a power law continuum fit. The continuum (at unity) and composite line fits are plotted. The individual Gaussian components of the fits are shown for the fit to N III] as dotted lines. In the other panels, the dashed and dotted lines represent the sum contribution of each labelled emission line. There is an unidentified bump at ~1070 Å that is not attributed to O VI (see Hamann et al. 1998). 32

3–4 Comparison of the measured FWHM of C IV to that of $H\beta$ for all objects in our sample with observations of both lines. In five cases, obvious narrow $H\beta$ emission was subtracted prior to measuring its FWHM. The open boxes represent five composite spectra created from objects in selected ranges of SMBH mass. The error bars drawn on the boxes represent the $\pm\ 1\sigma$ ranges for the FWHMs of C IV and $H\beta$ for these composite spectra. The filled diamonds represent averages of objects in selected ranges of C IV FWHM (< 2000 km/s, 2000–3000 km/s, 3000–4000 km/s, and 4000–6000 km/s). The dotted line is a 1:1 ratio and the dashed line is the expected ratio of FWHM(C IV) = $\sqrt{2}$ FWHM($H\beta$). 36

3–5 Comparison of the SMBH mass derived from C IV to that derived from $H\beta$ for all objects in our sample with observations of both lines. The filled diamonds represent averages of objects in selected SMBH mass ranges. The dotted line is a 1:1 ratio (the RMS scatter about the 1:1 relationship is 0.39 for the individual objects and 0.17 for the averages). For composite spectra of many objects, both methods yield approximately the same mass. 37

3–6 Redshift distribution of the AGN sample as a function of SMBH mass. The filled diamonds represent radio-quiet quasars and the open diamonds represent radio-loud quasars. There is clearly no trend in SMBH mass with redshift (for $z \gtrsim 0.3$). 38

3–7 Continuum luminosity versus SMBH mass. There is a very strong correlation with little scatter. Symbols as in Fig. 3-6. 39

3–8 The FWHM of C IV versus SMBH mass. A trend is seen, but with a large amount of scatter. Symbols as in Fig. 3-6. 39

3–9 Emission line equivalent widths as a function of SMBH mass. We calculated linear fits to the EWs for the entire SMBH mass range using a chi-square minimization routine (dotted lines). The slopes of these fits are given in the upper right hand corner of each plot. . . 41

3–10 Metallicities derived from comparisons of different line ratio diagnostics to theoretical results from Figure 5 in Hamann et al. (2002) are shown as a function of SMBH mass. The average includes N III]/C III], N III]/O III], N V/C IV, and N V/O VI. 43

3–11 Emission line ratios are shown as a function of the FWHM of C IV. . . 45

4–1 Distribution of the two measured quantities. The dotted lines represent constant L/L_{edd} ratios, with values indicated at the right. We created composite spectra for each of the seven ranges in Eddington ratio shown above. The filled diamonds represent radio-quiet quasars, the open diamonds represent radio-loud quasars, and the asterisks represent NLS1s. 58

4–2 Composite spectra, sorted by L/L_{edd}, with the mean L/L_{edd} values indicated at the right. The top spectrum is a composite spectrum created only from objects identified in the literature as NLS1s. The horizontal dashed lines and tick marks indicate the normalized continuum levels for each composite spectrum. The scaled height of the normalized continua above zero flux, as indicated for the bottom spectrum, is the same for all spectra plotted. 61

4–3 Multi-component Gaussian fits (smooth solid curves) to observed emission lines (jagged solid curves) for a composite spectrum of $< L/L_{edd} >\sim 0.58$. The continuum is normalized by a power law continuum fit. The continuum (at unity) and composite line fits are plotted. The individual components of the fits are shown for the fit to N III] as dotted lines. In the other panels, the dotted lines represent the sum contribution of each labelled emission line. There is an unidentified bump at ~1070 Å that is not attributed to O VI (see Hamann et al. 1998). 62

4–4 Distribution of estimated Eddington ratio, L/L_{edd}. The two arrows are the median (0.59) and mean (0.89) L/L_{edd} of the entire sample. About 27% of the objects have $L/L_{edd} > 1$. 64

4–5 Symbols as in Fig. 4-1. The dashed lines represent slopes from the L/L_{edd} equation (not fits). The positive correlation with L and negative correlation with FWHM(C IV) may be attributed largely to our derivation of L/L_{edd} from these quantities (see Equation 4.4). 65

4–6 Symbols as in Fig. 4-1. In bins of narrow luminosity ranges, there is no apparent trend between L/L_{edd} and redshift. Our sample, though, does seem to have a selection effect for more higher luminosity objects at higher redshifts. This, combined with the trend for higher luminosity objects to have higher L/L_{edd}, explains the slight trend that seems to exist in Fig. 4-5 between L/L_{edd} and redshift. 66

4–7 The diamonds represent the L/L_{edd} composites and the triangle represents the NLS1 composite. REWs are in angstroms. The dotted lines are linear fits to the L/L_{edd} composites, with slopes given in the upper right. The uncertainties shown are the 1σ standard deviations in the REWs based on repeated estimates with the continuum drawn at different levels (see §4.3). 69

4–8 Normalized composite spectra sorted by L/L_{edd} (top left, identical to Fig. 4-2 without the NLS1 composite) are compared to normalized composite spectra computed from different ranges in bolometric luminosity (top right, in units of ergs/sec), SMBH mass (bottom left, in $M_\odot$), and FWHM(C IV) (bottom right, in km/sec). Dashed lines and tick marks as in Fig. 4-2. The L, SMBH mass, and FWHM composite spectra all clearly show trends for decreasing line equivalent widths and peak heights as luminosity, SMBH mass, and FWHM(C IV) increase. The composite spectra sorted by FWHM(C IV) even exhibit this trend despite spanning less than half an order of magnitude in average luminosity, a much narrower range than in the L/L_{edd} composites (see Table 4-1). However, the L/L_{edd} composites show nearly constant peak heights and decreasing FWHMs with increasing L/L_{edd}. 71

4–9 Composite spectra sorted by L/L_{edd} for a narrow range in SMBH mass of $10^8 M_\odot < M_{\rm SMBH} < 10^9 M_\odot$ (left) are compared to ones sorted by L/L_{edd} for narrow range in luminosity of 10^{47} ergs/s $< L < 10^{48}$ ergs/s (right). The spectra are shown prior to normalization to the continuum. The composite spectra at nearly constant $M_{\rm SMBH}$ show the same emission-line behavior as the L/L_{edd} composites created from our entire sample: nearly constant peak heights and decreasing FWHMs with increasing L/L_{edd}. In contrast, the composite spectra at nearly constant L do not share this behavior and show a trend similar to the Baldwin Effect: decreasing peak heights and equivalent widths with increasing $M_{\rm SMBH}$. 72

4–10 Metallicities derived from comparisons of different line ratio diagnostics to theoretical results from Figure 5 in Hamann et al. (2002) are shown as a function of L/L_{edd}. The average includes N III]/C III], N III]/O III], and N V/(C IV+O VI). Symbols as in Fig. 4-7. 74

4–11 Symbols as in Fig. 4-7. Our best estimates of the overall metallicity of each spectrum are shown for the L/L_{edd}, SMBH mass, and luminosity composite spectra. The NLS1 composite, plotted in all three panels as a filled triangle, has a metallicity that is slightly high for its SMBH mass and luminosity, but still well below the metallicities of most luminous quasars. 75

5–1 Normalized composite spectra sorted by SMBH mass in narrow ranges of luminosity (top left and right) and FWHM(C IV) (bottom left) are compared to normalized composite spectra sorted by luminosity in a narrow range of SMBH mass (bottom right). The mean values of SMBH mass ($M_\odot$) and luminosity (ergs s^{-1}) are indicated to the right. The horizontal dashed lines and tick marks indicate the normalized continuum levels for each composite spectrum. The scaled height of the normalized continua above zero flux, as indicated for the bottom spectrum in each panel, is the same for all spectra plotted. The composite spectra sorted by SMBH mass all show a trend for decreasing line equivalent widths and peak heights as SMBH mass increases. However, the composites sorted by luminosity at nearly constant SMBH mass show nearly constant C IV peak heights and increasing Lyα peak heights with increasing luminosity. 88

5–2 Emission line ratios diagnostic of metallicity are plotted versus SMBH mass and luminosity for three of the composite spectra shown in Fig. 5-1. The dotted lines are linear fits to the data, with slopes given in the upper right. All of the ratios indicate a strong trend between metallicity and SMBH mass, but no trend between metallicity and luminosity. 90

5–3 Emission line REWs (in angstroms) versus SMBH mass and luminosity for the same three composite spectra in Fig. 5-2. The dotted lines are linear fits to the data, with slopes given in the upper right. O VI, Lyα, and C IV all show much stronger anti-correlations between REW and SMBH mass than between REW and luminosity. N V shows a positive correlation between REW and SMBH mass but an anti-correlation between REW and luminosity. 94

5–4 Emission line peak heights versus SMBH mass and luminosity for the same three composite spectra in Fig. 5-2. The peak heights decrease sharply with increasing SMBH mass, but remain constant or increase with increasing luminosity. The dotted lines are linear fits to the data with slopes given in the upper right. 95

5–5 Average metallicity versus SMBH mass for the two sets of composite spectra that span a range in SMBH mass at nearly constant luminosity. The composites with $46.5 < \log L < 47.5$ ergs s^{-1} are represented by filled diamonds and the composites with $47.0 < \log L < 47.5$ ergs s^{-1} are represented by open triangles. The average metallicity is obtained by comparing individual line ratios to theoretical predictions in Hamann et al. (2002) and then averaging the results of N III]/O III], N V/He II, and N V/(C IV+O VI). The dotted line is a linear fit to all seven datapoints with the slope given in the upper right. 97

6–1 Composite spectra of NLS1s with narrow and broad C IV λ1549 lines (top) and composite spectra created from our entire sample for different ranges in FWHM(C IV)/FWHM(Hβ λ4861) (bottom). In both comparisons, the N V λ1240 and N III] λ1751 lines stay nearly constant, while the objects with broader C IV *compared to Hβ* have much weaker C IV, He II λ1640, O III] λ1665, and C III] λ1909 emission lines. 107

6–2 Emission line ratios diagnostic of metallicity are plotted (without error bars for clarity) versus FWHM(C IV)/FWHM(Hβ) for various composite spectra (see §6.3 and Table 6-1). The filled triangle represents our overall NLS1 composite while the open triangles represent the separate NLS1 composites created from objects with narrow and broad C IV lines. The squares represent the composites created from objects with 2000 km s^{-1} < FWHM(Hβ) < 4000 km s^{-1} and sorted by FWHM(C IV)/FWHM(Hβ). The ×'s represent the composites created from our entire sample for different ranges in FWHM(C IV)/FWHM(Hβ). All sets of composite spectra show a trend for higher metallicities when C IV is broader compared to Hβ. 108

C–1 GatorPlot v4.4 plotting the rest-frame UV region of a composite spectrum. 120

C–2 GatorPlot's export window listing your choices of file formats. 123

C–3 GatorPlot's maths window demonstrating one of the above examples. 126

C–4 An example of a linear fit to the range 500–650 and 712.5–842 Å. . . 129

C–5 An example of a multiple Gaussian fit to the wavelength range 1450–1720 Å. The continuum in the spectrum being fit has been normalized to unity, so 1 is entered as the constant. An input file contains the initial parameters. 132

C–6 An example of a multiple Gaussian fit to the wavelength range 1450–1720 Å of a normalized composite spectrum. C IV is fit with three Gaussian profiles, and N IV], He II, and O III] are all fit with C IV profiles. The plot has been exported using the Screenshot .PS option in the Export menu. 134

C–7 An example of a user-defined fit of the function $Y = a\ sin(bX) + c$. . 139

E–1 Poster from the January 2003 AAS meeting in Seattle. 164

E–2 Poster from the July 2003 "AGN Physics With the SDSS" meeting. . 165

E–3 Poster from the January 2004 AAS meeting in Atlanta. 166

E–4 Poster from the June 2004 AAS meeting in Denver. 167

Abstract of Dissertation Presented to the Graduate School
of the University of Florida in Partial Fulfillment of the
Requirements for the Degree of Doctor of Philosophy

BLACK HOLE MASSES, METALLICITIES, AND EMISSION LINE PROPERTIES OF QUASARS

By

Craig D. Warner

August 2004

Chair: Fred Hamann
Major Department: Astronomy

I analyze rest-frame UV spectra for a large sample of 578 Type 1 active galactic nuclei (AGNs), spanning seven orders of magnitude in luminosity, five orders of magnitude in supermassive black hole (SMBH) mass, and a redshift range from $0 \leq z \leq 5$. I estimate SMBH masses by applying the virial theorem to the C IV λ1549 emission line and estimate metallicities by comparing several emission line ratios involving nitrogen to previous theoretical predictions. I perform the most comprehensive emission-line abundance analysis of a $z > 4$ quasar and find that even at this redshift, the gas close to quasars has a metallicity of solar or higher. This confirms previous estimates of solar or higher metallicities in these objects and suggests that an episode of vigorous star formation occurred before the observed epoch. Previous studies have found a correlation between luminoisty and metallicity in the broad emission-line region (BLR) and have hypothesized that host galaxy mass may be the parameter that determines metallicity. I test this hypothesis by making the first comparisons between BLR metallicity and SMBH mass, which has been shown correlate directly with host galaxy mass. I find a direct correlation between SMBH mass and BLR metallicity in AGNs, which can be understood in terms of more massive SMBHs residing in more massive host galaxies, combined with the well-known mass-metallicity relationship among galaxies. Neither luminosity, accretion efficiency, nor emission line FWHM shows any trend with metallicity at constant SMBH mass. Previous studies have hypothesized that the enhanced metallicities in Narrow Line Seyfert 1s (NLS1s), an unusual subclass of AGNs, may be linked to their high accretion efficiencies. I find that the enhanced metallicities in NLS1s are due to an unknown effect related to the ratio FWHM(C IV)/FWHM(Hβ), and not accretion efficiency. I also examine the Baldwin Effect, an inverse correlation between luminosity and the rest-frame equivalent widths (REWs) of emission lines. I find that emission line REWs and peak heights show a stronger inverse correlation with SMBH mass than with luminosity. I conclude that SMBH mass plays a critical role in defining the spectra of AGNs and that there is growing evidence for a close relationship between AGNs and their host galaxies.

CHAPTER 1
INTRODUCTION

Quasars are among the most distant and luminous objects in the universe. They are a subclass of active galactic nuclei (AGNs) distinguished by very high luminosities (typically $\gtrsim 10^{45}$ ergs s^{-1}) and broad emission lines ($\gtrsim$ 1000 km s^{-1}). Quasars, and AGNs in general, are compact objects that reside in the central regions of galaxies and are believed to be powered by supermassive black holes (SMBHs). Quasars, in particular, output a tremendous amount of energy: as much as thousands of times the energy our entire galaxy produces. Because quasars are so distant (redshifts range from $\sim$0.1 up to >5), observing them allows us to "look back" in time and provides valuable information on star formation and galaxy evolution. In particular, quasars at redshifts of $z \gtrsim 4$ allow us to study the universe when it was only $\sim$ 1 to 2 Gyr old (depending on cosmological models). Quasars consist of the central black hole and accretion disk of material spiralling inward, surrounded by gas clouds that compose the broad emission-line region (BLR). The BLR has a wide range of densities and ionization states and is radially stratified, such that higher ionization lines tend to form closer to the central engine than lower ionization lines (Peterson 1993).

The BLR is a useful probe of the central engines of quasars, and AGNs in general. First, the BLR is close enough physically that its bulk motions are almost certainly determined by the central SMBH via gravity and radiation pressure (Peterson 1993; Peterson & Wandel 2000). Secondly, the BLR is photoionized by the energy emitted by the central continuum source and it reprocesses this energy in the form of the quasar's emission-line spectrum (Peterson 1993). This emission-line spectrum also provides valuable information about the physical state and chemical composition of the gas close to quasars. If this gas was processed by stars in the surrounding host galaxy, then the metal abundances we measure are diagnostic of the star formation history in these environments (see Hamann & Ferland 1999; Hamann et al. 2002).

Emission line ratios involving nitrogen are particularly valuable in estimating the metallicity, Z, of the gas in the BLR because of the the expected "secondary" nitrogen production via the CNO cycle of nucleosynthesis in stars. In the CNO cycle, nitrogen is produced in the net from existing carbon and oxygen. The nitrogen abundance should therefore scale roughly as $Z^2 = (\mathrm{O/H})^2$ and N/O as $Z = \mathrm{O/H}$, providing a sensitive metallicity diagnostic even when direct measurements of Z are not available (Shields 1976; Hamann & Ferland 1992, 1993, 1999; Ferland et al. 1996; Hamann et al. 2002). Studies of both emission and absorption lines in quasars suggest that their metallicities are near or above the solar value (Osmer et al. 1994; Petitjean et al. 1994; Hamann 1997; Dietrich et al. 1999, 2000; Hamann & Ferland 1999; Constantin et al. 2001; Warner et al. 2002). These results are consistent with both theoretical simulations and observational studies that suggest metal abundances are dependent on the local density at any time in the universe (Cen & Ostriker 1999; Pettini 2001).

Furthermore, we expect quasars with more massive SMBHs to have higher metallicities. This can be understood in terms of more massive SMBHs residing in more massive host galaxies, combined with the well-known mass-metallicity relationship among galaxies. Many recent studies have demonstrated a direct correlation between the mass of the SMBH in AGNs and the mass of the host galaxy's bulge or spheroidal component (Magorrian et al. 1998; Laor 1998; Wandel 1999; Ferrarese & Merritt 2000, 2002; Gebhardt et al. 2000a; Tremaine et al. 2002). The overall mass of a galaxy's bulge or spheroidal component is also known to correlate with its metallicity (Faber 1973; Zaritsky et al. 1994; Jablonka et al.

1996; Trager et al. 2000). This relationship is attributed to more massive galaxies having deeper potential wells, making it harder for supernovae and stellar winds to expel matter from the region. The gas thus remains in the region longer and is reprocessed by new generations of stars, leading to higher metallicities.

SMBH masses in AGNs have been estimated by several indirect methods. One set of methods assumes that the gas in the BLR is in gravitational equilibrium with the SMBH and thus the SMBH mass can be estimated by applying the virial theorem, $M = rv^2/G$, to the line-emitting gas. Reverberation mapping studies have estimated the radial distance of the BLR from the SMBH, $R_{\rm BLR}$, based on the lag time between continuum variations and the emission-line response (Peterson 1993; Peterson 1997; Wandel et al. 1999; Kaspi et al. 2000). These studies have demonstrated an observed relation of approximately $R_{\rm BLR} \propto \lambda L_\lambda(5100\text{Å})^{0.7}$ that can be used to estimate $R_{\rm BLR}$, and thus SMBH masses, across a wide range of redshifts (Kaspi et al. 2000; McLure & Dunlop 2001; Vestergaard 2002; Warner et al. 2003). Other studies have estimated SMBH masses based on correlations between $M_{\rm SMBH}$ and i) the velocity dispersion of the host galaxy's spheroidal component (Ferrarese & Merritt 2000; Gebhardt et al. 2000a; Merritt & Ferrarese 2001; Tremaine et al. 2002), ii) a proxy of the velocity dispersion, such as the bulge luminosity (Magorrian et al. 1998; Laor 1998; Wandel 1999; McLure & Dunlop 2002; Erwin et al. 2002; Bettoni et al. 2003) or the width of the emission line [O III] λ5007 (Nelson 2000; Boroson 2003; Shields et al. 2003), or iii) the global structure of ellipticals and bulges (Graham et al. 2001; Erwin et al. 2002).

Each chapter in this dissertation is an article that has been or will be published in the *Astrophysical Journal* and the chapters are chronological. An important part of this work is the compilation of a large database of AGN spectra by Matthias Dietrich (see Dietrich et al. 2002), spanning 7 orders of magnitude in AGN luminosity, 5 orders of magnitude in SMBH mass, and a wide redshift range of $0 \lesssim z \lesssim 5$. This database is composed of both archival data and new observations by Fred Hamann, Joe Shields, Anca Constantin, and others. Of particular interest is the sample of 44 high-redshift ($z \gtrsim 4$) quasars discussed in Constantin et al. (2001).

I select a redshift 4.16 quasar, BR2248-1242, from this high-redshift sample and estimate its metallicity by comparing emission line ratios involving nitrogen to theoretical predictions from Hamann et al. (2002). BR2248-1242 was selected because it has unusually narrow emission lines with large equivalent widths, allowing us to measure weak intercombination lines such as N IV] λ1486, O III] λ1665, and N III] λ1751 and thus perform the most comprehensive emission-line abundance analysis to date for a $z > 4$ quasar. The narrow emission lines of BR2248-1242 imply that it has a low black hole mass for its luminosity and so may reside in a lower-mass, lower-metallicity host galaxy. Therefore, BR2248-1242 may yield a lower bound on the metallicity of luminous quasars.

The theory that AGN metallicity is dependent on the mass of the host galaxy is supported by previous results indicating a correlation between metallicity and AGN luminosity (Hamann & Ferland 1992, 1993, 1999). I test this theory by making the first comparisons between metallicity and SMBH mass, which correlates directly with host galaxy mass. I estimate SMBH masses for 578 objects in our database by applying the virial theorem to the line-emitting gas. Several previous studies have used this method to estimate black hole masses from the continuum luminosity and the FWHM of Hβ. I choose to use the C IV λ1549 emission line instead of Hβ because it is more readily observed across the entire redshift range from $z \sim 0$ to $z \sim 5$. I estimate SMBH masses from both C IV and Hβ for all 74 objects in our sample with observations of both lines and find approximately a 1:1 correlation. There can be significant deviations from this for individual objects, but the relation holds well for averages of many objects and measurements based on composite spectra. I create five composite spectra from different ranges in SMBH mass and measure the emission line ratios diagnostic of BLR metallicity. I find that the data are consistent with a trend between SMBH mass and BLR metallicity and the similarity between the slope of this trend and the slope of the galactic mass-metallicity relationship supports the premise that the gas in the BLR was processed/enriched by the surrounding host galaxy.

Our method of estimating SMBH masses is described in detail in §3.2. In particular, we estimate SMBH masses using FWHM(C IV) from Equation (3.4) and compare them to SMBH masses derived by applying equations (3.1) and (3.2) to Hβ. The uncertainties in the measurements of the FWHMs of C IV and Hβ are dominated by the theoretical uncertainties. Vestergaard (2002) calibrated mass estimates based on C IV and $\lambda L_\lambda(1450\text{Å})$ against mass estimates that use Hβ and a direct measurement of $R_{\rm BLR}$. She finds that SMBH mass estimates of individual objects derived from Equation (3.4) have a 1σ uncertainty of a factor of three when compared to derivations from Hβ and a direct measurement of $R_{\rm BLR}$. Our measurements of composite spectra should average over object-to-object variations, significanly reducing this uncertainty. There are additional uncertainties in that the slope of the $R_{\rm BLR}$–L relationship (Eqn. 3.2) is not known to an accuracy of better than about 0.15 (Netzer 2003) and the exact geometry and kinematics of the BLR are not precisely known (McLure & Dunlop 2001). However, any changes in either the powerlaw slope of the $R_{\rm BLR}$–L relationship or the assumption of random velocities in the BLR (see §3.2) affect only the absolute SMBH masses and not general trends involving SMBH mass.

While my results show a direct correlation between SMBH mass and BLR metallicity, I could not rule out luminosity or accretion efficiency as the fundamental parameter driving BLR metallicity. Accretion efficiency can be estimated by the Eddington ratio, $L/L_{edd} \propto \dot{M}_{acc}/M_{\rm SMBH}$, where $\dot{M}_{acc}$ is the accretion rate.

Narrow Line Seyfert 1s (NLS1s) are a subclass of AGNs that exhibit distinct and unusual properties including very narrow emission lines (FWHM(Hβ) $<$ 2000 km s^{-1}). Some studies have suggested that NLS1s have unusually high metallicities for their luminosities (Mathur 2000; Shemmer & Netzer 2002). These studies have hypothesized that high Eddington ratios may be responsible for the enhanced metallicities in NLS1s. I examine the relationships between SMBH mass, accretion efficiency, and emission line properties including the metallicity diagnostics. I find that at constant SMBH mass, composite spectra sorted by L/L_{edd} show an unusual emission-line behavior of nearly constant peak heights and decreasing FWHMs with increasing L/L_{edd}. One implication of this behavior is that derived metallicities show no trend with L/L_{edd}. I find that the NLS1s do exhibit a metallicity that is slightly high for their SMBH masses and luminosities, but the objects with the highest L/L_{edd} values, luminous, narrow-lined quasars, do not have enhanced metallicities. Therefore, I conclude that there must be some secondary effect, unrelated to L/L_{edd}, that is enhancing the metallicities in NLS1s.

Because SMBH mass and AGN luminosity are tightly correlated, I was unable to rule out luminosity as the parameter driving BLR metallicity in my previous study. Therefore, in order to isolate SMBH mass and luminosity, I create composite spectra that i) span a range in SMBH mass at nearly constant luminosity and ii) span a range in luminosity at nearly constant SMBH mass. All of the emission line ratios diagnostic of metallicity show a strong trend with SMBH mass in the composites at nearly constant L, but no trend with luminosity in the composites at nearly constant $M_{\rm SMBH}$. I conclude that host galaxy mass, coupled to the central SMBH mass, is the main determinant of AGN metallicities.

I finally reexamine the enhanced metallicities in NLS1s. I find that only NLS1s with broad ($>$ 3000 km s^{-1}) C IV lines exhibit enhanced metallicities. NLS1s with narrow C IV have metallicities consistent with other AGNs of similar $M_{\rm SMBH}$. Furthermore, examination of our entire AGN sample shows that this result is part of a general trend: rare objects with broad C IV *compared to Hβ* have higher metallicities than those with small or intermediate ratios of FWHM(C IV)/FWHM(Hβ).

Another important aspect of this study is the Baldwin Effect, an observed inverse correlation between AGN luminosity and the rest-frame equivalent widths (REWs) of emission lines such as Lyα, C IV, and O VI λ1034 (Baldwin 1977; Espey et al. 1993; Wills et al. 1993; Zheng & Malkan 1993; Osmer et al. 1994; Osmer & Shields 1999; Croom et al. 2002; Dietrich et al. 2002). I find that the REWs of these emission lines actually show a stronger inverse correlation with SMBH mass than with luminosity.

Finally, emission line fitting and the development of GatorPlot are important parts of this study (see Appendices). GatorPlot is a software package I developed in the IDL language that performs all of my plotting, fitting, and data manipulation. GatorPlot allows me to fit AGN emission lines much faster and more reliably than previous software and it provides more versatile fitting options.

CHAPTER 2
THE METALLICITY OF THE REDSHIFT 4.16 QUASAR BR2248-1242

2.1 Introduction

The prominent emission line spectra of quasars provide valuable information on the physical state and chemical composition of the gas close to the quasars. If this gas was processed by stars in the surrounding host galaxy, then the abundances we measure from the emission lines are a diagnostic of the star formation history in these environments (see Hamann & Ferland 1999 for a general review). At redshifts $z \gtrsim 4$, when the universe was only ~1 to 2 Gyr old (depending on cosmological models, see Figure 1 in Hamann & Ferland 1999), the results are especially interesting because they provide information about very early star formation, galaxy evolution, and chemical enrichment (Ostriker & Gnedin 1997; Friaca & Terlevich 1998).

Ratios of emission lines involving nitrogen, N, are valuable in determining the metallicity, Z, because of the expected "secondary" N production via the CNO cycle (Shields 1976). The nitrogen abundance therefore scales as $Z^2 = (\mathrm{O/H})^2$ and N/O scales as $Z = \mathrm{O/H}$, providing a sensitive metallicity diagnostic even when direct measures of $Z = \mathrm{O/H}$ are not available (Shields 1976; Ferland et al. 1996; Hamann & Ferland 1992, 1993, 1999). Observations of H II regions indicate that secondary nitrogen production dominates for $Z \gtrsim 0.2\ \mathrm{Z}_\odot$(Van Zee et al. 1998; Vila-Costas & Edmunds 1993). When secondary nitrogen production dominates, the N abundance is given by

$$[\mathrm{N/O}] \;\approx\; [\mathrm{O/H}] - q \;\approx\; \log(Z/\mathrm{Z}_\odot) - q \tag{2.1}$$

where the square brackets indicate logarithmic ratios relative to solar (Hamann et al. 2001). In environments with high star formation rates and short enrichment times, chemical evolution models predict that nitrogen production should be delayed relative to oxygen and carbon. In Equation (2.1), q is the logarithmic offset caused by this delay. It is believed to range from ~0.0–0.1 for "slow" chemical evolution, such as in H II regions, to ~0.2–0.5 for rapid evolution that may occur in massive galactic nuclei (Hamann et al. 2001).

Studies of both emission and absorption lines in quasars suggest that their metallicities are near or above the solar value (Dietrich et al. 1999, 2000; Osmer et al. 1994; Constantin et al. 2001; Petitjean et al. 1994; Hamann 1997; Hamann & Ferland 1999; Hamann et al. 2001). These metallicities are consistent with both observational studies (Pettini 2001) and theoretical simulations (Cen & Ostriker 1999) showing that metal abundances at any time in the universe are dependent on the local density. At every epoch, higher density regions, such as the central regions of galaxies where quasars reside, should have much higher metallicities than lower density regions such as galactic halos or the intergalactic medium. This dependence of metallicity on density seems to be stronger than any relationship to age (i.e., old does not necessarily mean metal poor). Evidence that density affects metallicity much more than age is found even in our own galaxy, where the central bulge contains many old but metal rich stars (McWilliam & Rich 1994; Idiart et al. 1996).

Much of the previous emission line analysis relied on the line ratios of N V λ1240/He II λ1640 and N V/C IV λ1549. Ratios of various weak intercombination lines can be used to test that analysis. In this paper, we measure the emission lines in the rest frame UV spectrum of the high redshift ($z = 4.16$) quasar BR2248-1242 (Storrie-Lombardi et al. 1996), and we examine line ratios involving nitrogen to estimate the metallicity. We selected BR2248-1242 from a sample of 44 $z \gtrsim 4$

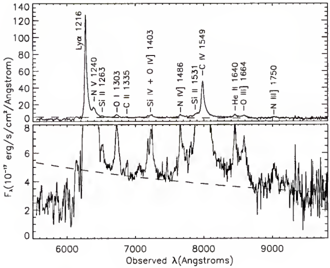

Figure 2–1 Spectrum of BR2248-1242 with our fit to the continuum overplotted (dashed line). The spectrum has been corrected for extinction.

quasars in Constantin et al. (2001) because it has unusually narrow emission lines with large equivalent widths, making the weak intercombination lines, such as N IV] λ1486, O III]λ1665, and N III] λ1750, easier to detect. This is the most comprehensive emission-line abundance analysis so far for a $z > 4$ quasar.

2.2 Data and Analysis

The spectrum of BR2248-1242 was obtained at the MMT Observatory with the Red Spectrograph on September 11, 1994. The full width at half maximum (FWHM) spectral resolution is ~10 Å which yields a difference of only ~10% between the observed and actual FWHM of even the most narrow component. The wavelength range was chosen to span the redshifted Lyα λ1216 to N III] λ1750 interval. This corresponds to an observed wavelength range of ~5500 Å to nearly 10,000 Å. The observation and data reduction details are discussed in Constantin et al. (2001). Figure 2-1 shows the observed spectrum.

We measured the emission lines using tasks in the IRAF[1] software package. We obtained the Galactic H I column density (Dickey & Lockman 1990) and calculated a reddening of $E_{B-V} = 0.0693$. We then performed a reddening correction and used the task NFIT1D to fit the continuum with a powerlaw of the form $F_\nu \propto \nu^\alpha$. The fit has a spectral index, $\alpha = -1.09$ (see Figure 2-1) and is constrained by the flux in wavelength intervals between the emission lines, namely 6913–6991 Å, 8733–8898 Å, and 9278–9777 Å. We next used the task SPECFIT (Kriss 1994), which employs a χ^2 minimization routine, to fit each line with one or more Gaussian profiles. Figure 2-2 shows the fits. Table 2-1 lists the line fluxes and rest-frame equivalent widths (REWs) as measured above the fitted continuum. The fluxes, REWs, and FWHMs given in Table 2-1 are from the total fitted profiles, which can include several multiplet components and up to 3 Gaussian profiles per component (see below). Table 2-2 lists the rest wavelength, flux, REW, and FWHM of each individual Gaussian profile. We calculate the emission line redshift to be $z = 4.156$ based on the narrow Gaussian profiles fit to Lyα and C IV. We use this redshift to calculate the rest wavelength for each component.

We fit C IV $\lambda1549$ with three Gaussian profiles, including a very broad profile (FWHM $\approx$ 22500 km s^{-1}). This broad pedestal includes the unidentified ~1600 Å emission feature that has been noted in earlier studies (Laor et al. 1994; Boyle 1990; Wilkes 1984). We ignore the doublet splitting in C IV because it is small compared to the observed line widths. N IV] $\lambda1486$, He II $\lambda1640$, and O III] $\lambda1665$ are all fit with one Gaussian profile. Each component of the Si II $\lambda\lambda1527, 1533$ and Si IV$\lambda\lambda1393, 1403$ doublets is fit with one Gaussian profile. The fluxes of these

---

[1] The Image Reduction and Analysis Facility (IRAF) is distributed by the National Optical Astronomy Observatories, which is operated by the Association of Universities for Research in Astronomy, Inc. (USRA), under cooperative agreement with the National Science Foundation.

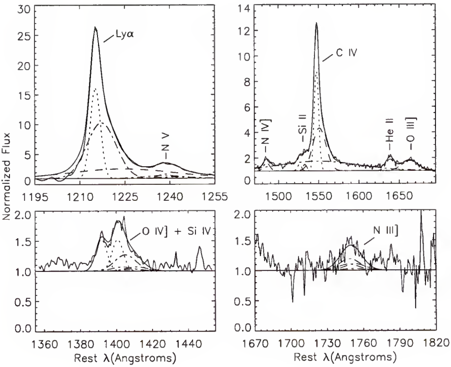

Figure 2–2 Gaussian fits of emission lines of BR2248-1242. The continuum is normalized by the power law fit shown in Figure 2-1. The continuum (at unity) and composite line fits are plotted as solid curves. The individual components of the fits are shown as dotted and dashed lines.

Table 2–1 Emission Line Data

Line	λ^a_{obs}	Flux^b	Flux/Lyα	REW^a	FWHM^c
Lyα λ1216	6270.3	6040	1.000	246	1450
N V λ1240	6396.6	420	0.070	18	2380
Si II λ1263	6509.9	90	0.014	4	3660
O I λ1303	6728.7	250	0.041	10	3020
C II λ1335	6874.2	30	0.005	1	1270
Si IV λ1397	7204.5	180	0.029	8	3490
O IV] λ1403	7254.8	140	0.023	7	3240
N IV] λ1486	7663.9	130	0.021	6	1910
Si II λ1531	7892.1	120	0.020	6	2450
C IV λ1549	7984.8	2400	0.398	122	1620
He II λ1640	8455.3	210	0.035	11	2200
O III] λ1665	8580.6	350	0.059	19	4200
N III] λ1751	9029.2	160	0.026	9	3530

[a] In units of Å

[b] In units of 10^{-17} ergs cm^{-2} s^{-1}

[c] In units of km s^{-1}

Table 2–2 Emission Line Components

Component	λ^{a}_{rest}	Flux[b]	REW[a]	FWHM[c]
Lyα 1	1216.1	1580	64	970
Lyα 2	1218.1	2780	112	2810
Lyα 3	1225.1	1690	69	10020
N V 1	1240.2	140	6	1280
N V 2	1240.6	280	12	3710
Si II	1262.8	90	4	3390
O I	1305.0	250	10	3020
C II	1333.2	30	1	1230
Si IV	1397.3	180	8	1570
O IV]	1407.1	140	7	3000
N IV]	1486.3	130	6	1910
Si II	1530.7	120	6	1140
C IV 1	1548.6	1070	55	1280
C IV 2	1552.2	1330	68	3710
C IV 3	1551.0	1820	93	22570
He II	1639.9	210	11	2200
O III]	1664.2	350	19	4200
N III]	1751.2	160	9	3390

[a] In units of Å

[b] In units of 10^{-17} ergs cm^{-2} s^{-1}

[c] In units of km s^{-1}

components are tied to a 1:1 ratio because this yields a better fit than a 2:1 ratio. In every multiplet fit, we fix the ratio of the central wavelengths to the known ratio of the rest wavelengths and tie together the FWHMs of each component. The N III] λ1750 and O IV] λ1403 multiplets are fit with one Gaussian profile for each of their 5 components. The flux component ratios in these cases are tied to the ratio of the statistical weight *g* times the *A* value for each transition, using atomic data obtained from the National Institute of Standards and Technology (http://aeldata.phy.nist.gov/PhysRefData/contents-atomic.html) and Nussbaumer & Storey (1982). Lyα λ1216 is fit with three Gaussian components, with only the red side used for χ^2 minimization because of contamination by the Lyα forest on the blue side. Each component of the N Vλ1240 doublet is fit with two Gaussian profiles with FWHMs fixed to the values obtained from the narrow and intermediate width profiles of our fit to C IV. This connection between C IV and N V can be justified because they are both high ionization lines with similar excitation and emission properties (Dietrich & Wilhelm-Erkens 2000). The relative fluxes of the two components of the N V doublet are set to 2:1 for each component, again because this yields a better fit than a 1:1 ratio. We fit the Si II λλ1260, 1264, 1265 triplet with one Gaussian profile for each of the three components. Because the flux of Si II is so much smaller than Lyα and N V, Si IIis not well defined by the χ^2 minimization.

The primary uncertainty in our flux measurements is the continuum location. Many of the lines are blended, which introduces more uncertainty, particularly for N V in the wing of Lyα. The broad component in the C IV fit introduces another uncertainty because it includes the ~1600 Å feature. We do not include this broad component in our calculated of flux ratios (§2.3 below) because it is believed to be an unrelated emission feature (Laor et al. 1994). We estimate the one σ standard deviation of our measurement of the flux of Lyα to be ~10% based on repeated

Table 2–3 Emission Line Ratios

Lines	Ratio	$Z/Z_\odot$
N III]/O III]	0.45	$1.74^{+0.16}_{-0.05}$
N IV]/O III]	0.36	$2.43^{+0.00}_{-1.20}$
N IV]/C IV	0.05	$1.55^{+0.16}_{-0.44}$
N V/He II	2.02	$3.07^{+3.94}_{-1.48}$
N V/C IV	0.18	$1.49^{+0.09}_{-0.25}$

measurements with the continuum drawn at different levels. By the same method, we estimate the uncertainty in C IV, N V, He II, and O III] to be ~15–20% and the uncertainty in the remaining lines with REW $\leq$ 10 Å to be ~25%.

2.3 Results

Table 2-3 lists various measured flux ratios and the metallicities inferred from comparisons to the theoretical results from Hamann et al. (2001). Our preferred estimates of the metallicity are obtained from the model in Hamann et al. that uses a segmented powerlaw for the photoionizing continuum shape (see Figure 2-3). This continuum shape is a good approximation to the average observed continuum in quasars (Zheng et al. 1997; Laor et al. 1997). The metallicity ranges in Table 2-3 represent the range of results obtained by comparisons to all three different continuum shapes calculated by Hamann et al. and shown in Figure 2-3. These theoretical uncertainties are in addition to any uncertainty in the measured line strengths (§2.2).

All of the line ratios in Table 2-3 yield a metallicity of $Z \approx 1$–$3\ Z_\odot$. From a theoretical viewpoint, N III]/O III] is the most reliable of the intercombination line ratios (Hamann et al. 2001). N V/He II is also a useful ratio, whereas N IV]/O III]and N IV]/C IV can be unreliable because they are more sensitive to non-abundance effects and generally yield a wider range of results than N III]/O III].

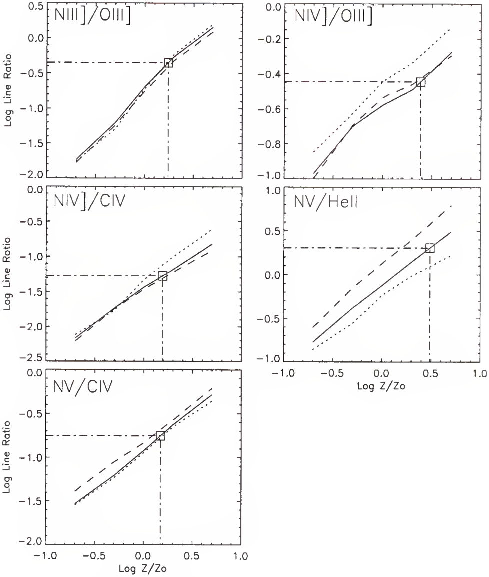

Figure 2–3 Comparison of flux ratios measured in BR2248-1242 to theoretical results from Figure 5 of Hamann et al. (2001). Comparisons of our measured line ratios to the theoretical model represented by the solid line yield our preferred estimates for metallicity. The solid line is obtained from the model in Hamann et al. that uses a segmented powerlaw for the photoionizing continuum shape, which is a good approximation to the average observed continuum in quasars. The dotted line corresponds to the model that uses an incident spectrum defined by Matthews & Ferland (1987), while the dashed line corresponds to a powerlaw with index $\alpha = -1.0$ across the infrared through X-rays .

Based on which ratios are most accurately measured, and which are most reliable from a theoretical viewpoint (Hamann et al. 2001), we estimate the overall metallicity of BR2248-1242 to be roughly $Z \approx 2\ \mathrm{Z}_\odot$.

It is important to note, however, that the actual metallicity of BR2248-1242 may be 2–3 times higher than $Z \approx 2\ \mathrm{Z}_\odot$ because the theoretical models we use assume $q \approx 0$ in Equation (2.1). For environments with rapid chemical evolution, such as massive galactic nuclei, $q \approx 0.2$–0.5 may be more appropriate (Hamann et al. 2001). Therefore, the metallicity of BR2248-1242 is broadly consistent with previous emission line results of $Z \approx 1$–$9\ \mathrm{Z}_\odot$ derived for other quasars (Hamann et al. 2001; Dietrich & Wilhelm-Erkens 2000; Hamann & Ferland 1999; Korista et al. 1998; Ferland et al. 1996).

For any appropriate q value, BR2248-1242 may still yield a lower bound on the metallicity of luminous quasars because it appears to have an unusually low black hole mass (and so may reside in a lower mass, lower metallicity galaxy). We estimate the black hole mass in BR2248-1242 to be $M_{BH} \approx 4.77 \times 10^8\ \mathrm{M}_\odot$, based on the measured FWHM of C IV and the formulae given in Kaspi et al. (2000)

$$R_{\mathrm{BLR}} = (32.9^{+2.0}_{-1.9}) \left[\frac{\lambda L_\lambda(5100\text{Å})}{10^{44}\ \mathrm{ergs\ s^{-1}}}\right]^{0.700\pm0.033} \quad \mathrm{lt-days} \qquad (2.2)$$

$$M = 1.464 \times 10^5 \left(\frac{R_{\mathrm{BLR}}}{\mathrm{lt-days}}\right)\left(\frac{v_{\mathrm{FWHM}}}{10^3\ \mathrm{km\ s^{-1}}}\right)^2 \ \mathrm{M}_\odot \qquad (2.3)$$

where R_{BLR} is the radius of the broad line region for $H\beta$, and $R_{\mathrm{BLR}}(\mathrm{C\,IV}) \approx 0.5\ R_{\mathrm{BLR}}(H\beta)$ is the radius of the C IV region (Peterson 2001). The FWHM of C IV (1620 km $\mathrm{s^{-1}}$) is represented by v_{FWHM} and M is the mass of the black hole. We derive $\lambda L_\lambda(1450\text{Å})$ from the observed flux (Dietrich et al. 2002) and use a powerlaw of the form $F_\nu \propto \nu^\alpha$ with $\alpha = -0.4$ to approximate the continuum shape and estimate $\lambda L_\lambda(5100\text{Å})$. We select $\alpha = -0.4$ based on average quasar spectra from Vanden Berk et al. (2001) and Dietrich et al. (2002). The derived black hole mass in BR2248-1242 is unusually low because of its unusually narrow emission lines. Previous studies suggest a correlation between black hole mass and the overall bulge/spheroidal component mass of the surrounding galaxy (Gebhardt et al. 2001; Ferrarese & Meritt 2000; Laor 2001; Wandel 1999). Together with the well known relationship between the mass and metallicity of galaxies (Faber 1973; Zaritsky et al. 1994; Jablonka et al. 1996), these results predict a relationship between the mass of the black hole and the metallicity surrounding the quasar (Warner et al. 2003). BR2248-1242 appears to have a low black hole mass, and so may be expected to have relatively low metal abundances.

2.4 Discussion

The result for $Z \gtrsim Z_\odot$ in BR2248-1242 suggests that an episode of rapid and extensive star formation occurred before the observed $z = 4.16$ epoch. The spectral similarity of BR2248-1242 to other $z > 4$ quasars (apart from the narrow line widths, see Constantin et al. 2001) suggests further that the result for $Z \gtrsim Z_\odot$ should apply generally. The time available for the chemical enrichment at $z = 4.16$ is only ~1.5 Gyr (for $H_0 = 65$ km s^{-1} Mpc^{-1}, $\Omega_m = 0.3$ and $\Omega_\Lambda \lesssim 1$). This star formation episode early in the history of the universe would be consistent with observations showing that the central regions of massive galaxies today contain old, metal rich stars (McWilliam & Rich 1994; Bruzual et al. 1997; Worthey et al. 1992; Idiart et al. 1996). This high redshift evolution would also be well within the parameters derived in some recent simulations, which show that the densest proto-galactic condensations can form stars and reach solar or higher metallicities at $z \gtrsim 6$ (Ostriker & Gnedin 1997; Haiman & Loeb, 2001). Recent observations of the highest redshift quasars suggest that reionization occurred around $z \sim 6$ (Becker et al. 2001; Djorgovski et al. 2001). If the reionization is due to stars, this would provide further evidence for substantial star formation beginning at $z \gtrsim 6$. Quasar abundance studies can provide observational tests of these evolution scenarios. The next step is clearly to extend the abundance analysis to the highest possible redshifts, and to compare the results across wide ranges in redshift, host galaxy types, and central black hole mass.

CHAPTER 3
A RELATION BETWEEN SUPERMASSIVE BLACK HOLE MASS AND QUASAR METALLICITY?

3.1 Introduction

Supermassive black holes (SMBHs) are believed to drive the tremendous energy output of quasars, and more generally, active galactic nuclei (AGNs). Recent studies have shown that the centers of all massive galaxies today harbor SMBHs (Gebhardt et al. 2000a; Ferrarese & Merritt 2002). Moreover, the mass of the black hole scales directly with the mass of the host galaxy, or more specifically, the mass of the host galaxy's bulge or spheroidal component. The early results were based on a correlation between SMBH mass and bulge luminosity, L_{bulge} (Magorrian et al. 1998; Laor 1998; Wandel 1999), which showed a large scatter, as much as two orders of magnitude in SMBH mass (Ferrarese & Merritt 2000). Subsequent studies focused on the relationship between the masses of SMBHs and the velocity dispersions, σ, of their host bulges or spheroids. This relation shows considerably less scatter than the $M_{\mathrm{SMBH}} - L_{\mathrm{bulge}}$ relation (Ferrarese & Merritt 2000; Gebhardt et al. 2000a; Merritt & Ferrarese 2001; Tremaine et al. 2002). There is also no significant difference between the relationships measured for active and quiescent galaxies (Gebhardt et al. 2000b; Ferrarese et al. 2001). Recently, SMBH mass has also been shown to correlate strongly with the global structure of ellipticals and bulges (e.g., more centrally concentrated bulges have more massive SMBHs). This relationship is as strong as the $M_{\mathrm{SMBH}} - \sigma$ relationship with comparable scatter (Graham et al. 2001; Erwin et al. 2002). Studies that carefully model the bulge light profiles of disk galaxies and thereby obtain more accurate values of L_{bulge} also show less scatter in $M_{\mathrm{SMBH}} - L_{\mathrm{bulge}}$, similar to that in the $M_{\rm SMBH} - \sigma$ relationship (McLure & Dunlop 2002; Erwin et al. 2002; Bettoni et al. 2003).

The overall mass of a galaxy is also known to correlate with its metallicity (Faber 1973; Zaritsky et al. 1994; Jablonka et al. 1996; Trager et al. 2000). This relationship is generally understood in terms of the gravitational binding energy. More massive galaxies have deeper potential wells, making it harder for supernovae and stellar winds to blow matter out of the region. Therefore, the gas remains in the galaxy longer, where it is further reprocessed by stars, leading to higher metallicities. This mass-metallicity relationship, combined with the relationship between SMBH mass and galaxy mass, suggests that there should be a relationship between SMBH mass and the metallicity of the gas clouds surrounding quasars (Hamann & Ferland 1993).

The metallicity of the gas in the broad emission line region (BLR) of quasars can be estimated by analyzing prominent emission lines. BLR metallicities should be representative of the gas in the central regions of galaxies if the BLR was enriched by stars in those environments. Previous studies have demonstrated that we cannot simply examine ratios of strong metal to hydrogen lines, such as C IV λ1549 / Lyα, to measure the C/H abundance. This is because strong collisionally excited lines like C IV play an important role in cooling the gas. Increasing the metallicity and thus C/H leads to lower gas temperatures and an almost constant C IV / Lyα ratio (Hamann & Ferland 1999). The best abundance diagnostics for the BLR involve ratios of lines that are i) not important in the cooling, and ii) have similar excitation/emission requirements (Hamann et al. 2002). Ratios of emission lines involving nitrogen, N, are especially valuable in determining the metallicity, Z, because of the expected "secondary" N production via the CNO cycle of nucleosynthesis in stars (Shields 1976; Hamann & Ferland 1992, 1993, 1999; Ferland et al. 1996; Hamann et al. 2002). In the CNO cycle, nitrogen is produced from existing carbon and oxygen. The nitrogen abundance should therefore scale roughly as N/H $\propto Z^2$ or N/O $\propto$ O/H $\propto Z$ (Tinsley 1980), providing a sensitive metallicity diagnostic even when direct measures of $Z =$ O/H are not available. Observations of H II regions indicate that secondary nitrogen production and N/O $\propto$ O/H scaling dominate for $Z \gtrsim 0.2 - 0.3$ Z$_\odot$ (van Zee et al. 1998; Pettini et al. 2002).

Some other studies suggest that there can be significant departures from the simple N/O $\propto$ O/H relationship owing to time-dependent or perhaps metallicity-dependent yields of N, O, and C (eg. Henry et al. 2000). These effects are often invoked to explain the observed object-to-object scatter in N/O versus O/H. However, there is a general consensus that large (solar or higher) N/O ratios indicate large (solar or higher) metallicities. Moreover, the most homogeneous and therefore most reliable H II region data (Pilyugin et al. 2002; Pettini et al. 2002) indicate that the scatter in N/O decreases and the validity of N/O $\propto$ O/H improves in the regime of roughly solar or higher metallicities. This is the regime of the gas near quasars, based on studies of both their broad emission and intrinsic narrow absorption lines (Constantin et al. 2001; Dietrich et al. 1999, 2003a; Hamann 1997; Hamann & Ferland 1999; Hamann et al. 2002; Osmer et al. 1994; Petitjean et al. 1994; Warner et al. 2002). In this paper, we simply assume that N/O $\propto$ O/H applies. We also note that our analysis of composite quasar spectra naturally averages over object-to-object variations. Any metallicity trends that we infer from the emission line ratios depend on this assumption of N/O $\propto$ O/H in addition to measurement and photoionization modeling uncertainties.

We have collected spectra of over 800 "Type 1" AGNs (quasars and Seyfert 1 galaxies) from the HST archives and various ground-based observing programs to examine trends in their emission line properties (Dietrich et al. 2002). 578 of these spectra span the rest-frame UV wavelengths needed for this study. We compute five composite quasar spectra from this sample, representing different intervals in SMBH mass from 10^6 to 10^{10} $M_\odot$. We present measurements of the emission lines in these composite spectra and investigate the relationship between SMBH mass and the metallicity of the BLR gas.

3.2 SMBH Mass Determinations

We estimated black hole masses by applying the virial theorem, $M_{\rm SMBH} = rv^2/G$, to the line-emitting gas, where v is the velocity dispersion and r is the radial distance away from the SMBH (Peterson & Wandel 2000). The relationship between v and the FWHM of the broad emission line profile depends on the kinematics and geometry, but can be expressed as $v = k \times$ FWHM, where k is a factor on the order of unity (McLure & Dunlop 2001; Vestergaard 2002). Kaspi et al. (2000) express the SMBH mass as

$$M = 1.464 \times 10^5 \mathrm{M}_\odot \left(\frac{R_{\rm BLR}}{\rm lt-days}\right)\left(\frac{\rm FWHM}{10^3\ \rm km\ s^{-1}}\right)^2 \tag{3.1}$$

FWHM applies to the broad emission line profile, and $R_{\rm BLR}$ is the radial distance between the BLR and the central mass/continuum source. Equation (3.1) assumes the gas in the BLR is gravitationally bound and BLR velocities are random. The exact geometry and kinematics are still debated (e.g., McLure & Dunlop 2001), but are unknown, so we take this approach of random velocities ($k = \sqrt{3}/2$) because it is the most basic and allows for comparison with most other work. Any offset in mass due to different geometric or kinematic assumptions would only affect the absolute SMBH masses and not any trends derived between metallicity and SMBH mass. We estimate $R_{\rm BLR}$ based on the observed relation between $R_{\rm BLR}$ for a particular line and the continuum luminosity (Kaspi et al. 2000; Vestergaard 2002; Wandel et al. 1999). A particular line must be specified because reverberation studies have shown that the BLR is radially stratified, such that higher ionization lines tend to form closer to the central engine than lower ionization lines (Peterson

1993). Kaspi et al. (2000) find

$$R_{\rm BLR}(H\beta) = (32.9^{+2.0}_{-1.9}) \left[\frac{\lambda L_{\lambda}(5100\text{Å})}{10^{44}\ \text{ergs s}^{-1}}\right]^{0.700\pm0.033} \quad \text{lt} - \text{days} \qquad (3.2)$$

where $R_{\rm BLR}(H\beta)$ is the radial distance between the central continuum source and the $H\beta$ emission line region and $\lambda L_{\lambda}(5100\text{Å})$ is the continuum luminosity at 5100 Å in the AGN rest frame. We choose to use the C IV $\lambda1549$ emission line instead of $H\beta$ to estimate the SMBH mass because it is more readily observed across the entire redshift range from $z \sim 0$ to $z \sim 5$. C IV may in fact yield a better estimate of SMBH mass than $H\beta$ because $H\beta$ can include a narrow line component that forms in a different region and thus must be subtracted before measuring the FWHM. C IV has no such narrow component (Wills et al. 1993, Vestergaard 2002). It has recently been suggested that Mg II $\lambda2798$ may be a better indicator of SMBH mass than C IV (McLure & Jarvis 2002). However, C IV is observable over a wider range of redshifts and is clearly the best choice among UV lines at shorter wavelengths. Significant blending effects are much less common for C IV than other strong lines in the rest-frame UV spectrum and absorption effects are much less common for C IV than for Lyα (Vestergaard 2002).

Several studies have noted that higher ionization lines, such as C IV, are blueshifted with respect to lower ionization lines such as $H\beta$ and Mg II (Tytler & Fan 1992; Richards et al. 2002). If this shift is large and the shift is caused by obscuration of the red side of the profile, then the measured FWHM of C IV could significantly underestimate the intrinsic FWHM. However, if the velocity of the blueshift is small compared to the FWHM of C IV (e.g., Tytler & Fan 1992), then the FWHM should still be a good measure of the virial speeds in the C IV region. Also, even in the highly blueshifted profiles, the average C IV FWHM is not significantly broader than in the non-blueshifted case, and therefore blueshifting does not present an obvious source of error. Finally, we will show (see §3.4) that the SMBH masses derived from C IV and $H\beta$ are approximately the same when averaged over quasar samples.

Reverberation studies indicate that the size of the broad emission line region for C IV is about half that of $H\beta$ (Stirpe et al. 1994; Korista et al. 1995; Peterson 1997; Peterson & Wandel 1999). We modify Equation (3.2) to account for this and we use a powerlaw of the form $F_\nu \propto \nu^\alpha$ with $\alpha = -0.4$ to estimate a conversion between the continuum luminosity at 5100 Å and 1450 Å. We select $\alpha = -0.4$ based on average quasar spectra from Brotherton et al. (2001), Vanden Berk et al. (2001), and Dietrich et al. (2002). This yields

$$R_{\rm BLR}({\rm CIV}) = 9.7 \left[\frac{\lambda L_\lambda(1450{\rm \AA})}{10^{44}\ {\rm ergs\ s^{-1}}}\right]^{0.7}\ \ {\rm lt-days} \tag{3.3}$$

Vestergaard (2002) finds that this technique of using the continuum luminosity and the FWHM of C IV yields an estimate of the central black hole mass that has a 1σ uncertainty of a factor of three when compared to reverberation mapping studies that use $H\beta$ to estimate SMBH masses. From Equations (3.1) and (3.3), we obtain

$$M = 1.4 \times 10^6 {\rm M}_\odot \left(\frac{\rm FWHM(CIV)}{10^3\ {\rm km\ s^{-1}}}\right)^2 \left(\frac{\lambda L_\lambda(1450{\rm \AA})}{10^{44}\ {\rm ergs\ s^{-1}}}\right)^{0.7} \tag{3.4}$$

This is essentially the same as (within 10% of) the mass relationship derived by Vestergaard using C IV and $\lambda L_\lambda(1350{\rm \AA})$ (For this comparison, we again assume the powerlaw index, $\alpha = -0.4$ between 1450 and 1350 Å.) The difference of ~ 10% between the two formulae is negligible compared to the 1σ uncertainty of a factor of three. See also Netzer (2003) and Corbett et al. (2003) for further discussion of the uncertainties.

While multi-epoch spectra are preferable (to average over variabilities), single-epoch spectra may be used if the signal-to-noise ratio is high enough because the FWHM of single-epoch spectra are generally consistent with the FWHMs of the mean and rms spectra obtained from multi-epoch observations (Vestergaard 2002).

It is important to accurately measure the FWHM because the uncertainties in SMBH mass are dominated by the uncertainties in the FWHM. Our composite spectra are each made up of single-epoch observations of multiple quasars and therefore should be approximately equivalent to multi-epoch observations of the same sources.

3.3 Data and Analysis

We have compiled a sample of more than 800 quasar spectra, spanning a redshift range from $0 \lesssim z \lesssim 5$ and six orders of magnitude in intrinsic luminosity. The spectra were obtained by several groups using various ground-based instruments, as well as the *International Ultraviolet Explorer (IUE)* and the *Hubble Space Telescope (HST)*. One unique aspect of this sample is that it contains new observations of faint quasars at redshift $z > 2.5$ (Dietrich et al. 2002). Thus we can avoid to some degree the bias toward higher luminosities at higher redshifts that affects other magnitude-limited samples. 578 of the spectra have UV wavelength coverage that encompasses the range $950 \lesssim \lambda \lesssim 2050$ Å. Each spectrum was transformed to the rest-frame using a redshift measured from the centroid of the upper 50% of the C IV λ1549 profile. See Dietrich et al. (2002) and Dietrich et al. (2003b) for more details on the AGN sample and how luminosities were obtained. Throughout this paper, we use the cosmological parameters $H_0 = 65$ km s^{-1} Mpc^{-1}, $\Omega_M = 0.3$, and $\Omega_\Lambda = 0$ (Carroll, Press, & Turner 1992). We used radio flux densities given in Véron-Cetty & Véron (2001) to determine the radio loudness for the quasars.

We use an automated program to estimate the FWHM of C IV in each spectrum. The program averages over noise by applying a smoothing routine that calculates the median of each five-pixel interval. It then fits a local linear continuum (contrained by the flux in 25 Å wide intervals centered around 1442.5 Å and 1712.5 Å) around C IV, measures the peak flux of the emission line (of the smoothed spectrum), and uses those to estimate the FWHM of the line.

Table 3–1. Composite Parameters

Log $M_{\rm SMBH}$ [$M_\odot$]	α	# Objects at C IV	FWHM(C IV) [km s^{-1}]	# Objects at $H\beta$	FWHM($H\beta$) [km s^{-1}]	Log λL_λ(1450Å) [ergs s^{-1}]	Log $M_{\rm mean}$ [$M_\odot$]
$6-7$	-0.98	7	2100	4	1400	44.0	6.78
$7-8$	-0.90	61	3300	31	2250	45.0	7.27
$8-9$	-0.71	198	3900	35	3000	46.2	8.65
$9-10$	-0.59	261	4900	6	3650	46.9	9.54
>10	-0.57	34	6500	1	4500	47.5	10.28

Comparisons between the FWHMs estimated by the program and those measured manually indicate an error of $\lesssim$ 10% in the estimates. Lines containing significant absorption are flagged by the program and their FWHMs are estimated manually (by manually interpolating across the absorption feature). We use the FWHM of C IV and the continuum luminosity, λL_λ(1450Å) to estimate the central SMBH mass of each quasar based on Equation (3.4).

We then sorted the quasars by SMBH mass into five bins: $10^6 - 10^7$ M$_\odot$, $10^7 - 10^8$ M$_\odot$, $10^8 - 10^9$ M$_\odot$, $10^9 - 10^{10}$ M$_\odot$, and $> 10^{10}$ M$_\odot$, and computed five composite spectra. Each composite spectrum is the average of all the quasar spectra in a bin (see Table 3-1 for data about each composite spectrum, including the powerlaw index, α, of the continuum fit, the number of objects contributing to the composite at and FWHM of C IV and $H\beta$, continuum luminosity, and mean SMBH mass). Calculating composite spectra increases the signal-to-noise ratio significantly, making it easier to measure weaker emission lines that may be lost in the noise in individual spectra.

Since narrow absorption features may influence the emission line profiles in composite spectra, we developed a method to detect strong narrow absorption features that exclude the contaminated spectral region of individual spectra from the calculation of the composite spectrum. The procedure is roughly as follows (see Dietrich et. al 2002 for more details). First, a preliminary mean spectrum is calculated from all of the spectra in a given mass bin. Each individual spectrum is then divided by this preliminary mean to derive a ratio spectrum. The ratio spectrum is smoothed with a running boxcar function, which provides in addition to the smoothed ratio also a root-mean-square (rms) value for each wavelength box. A narrow absorption line will cause a sharp increase in the rms spectrum. The contaminated spectral regions of individual spectra, identified by these rms spikes, are excluded from the calculation of the final composite spectra, and no interpolation has been applied (Dietrich et al. 2002).

We next corrected each composite spectrum for strong iron emission lines. To get a first estimate of the contribution of Fe emission, we used the empirical Fe emission template that was carefully extracted from I Zw 1 by Vestergaard & Wilkes (2001), which they very kindly provided for this study. The template is mostly Fe II emission but contains some Fe III emission as well. We have modified this Fe emission template in the UV range $\lambda\lambda 1200 - 1540\,\text{Å}$ in accordance with photoionization model calculations presented by Verner et al. (1999). Based on our analysis of quasar composite spectra (Dietrich et al. 2002), we found that the strength of Fe line emission in the wavelength range $\lambda\lambda 1420 - 1470\,\text{Å}$ is equal to ~2% of the integrated *pseudo continuum* flux in this wavelength range (Dietrich et al. 2002). Fe contributions vary for other wavelength ranges, but we scale the entire template to match the 2% contribution in the range 1420 – 1470 Å. This estimate of a 2% contribution is conservatively low to avoid over-subtraction of the Fe emission template. The spectral width of the Fe emission features was adjusted to a width corresponding to the FWHM of the C IV $\lambda 1549$ emission line profile of each quasar. The appropriate scaled Fe emission template was subtracted from the corresponding composite spectrum. In spite of its small contribution, the estimate of the Fe line emission improves particularly the measurements of N III]$\lambda 1750$ and lines such as He II $\lambda 1640$ near an unidentified $\lambda 1600\,\text{Å}$ emission feature (Laor et al. 1994; Vestergaard & Wilkes 2001).

We used the task NFIT1D in the IRAF[1] software package to fit the continuum of each Fe-subtracted spectrum with a powerlaw of the form $F_\nu \propto \nu^\alpha$. The fits were constrained by the flux in wavelength intervals between the emission lines, namely in 25 Å wide windows centered at 1460 Å, 1770 Å, and 2000 Å. The spectral indices overall differ from $\alpha = -0.4$ because the powerlaw fit is to a narrower wavelength range than, for example, Dietrich et al. (2002) or Vanden Berk et al. (2001). However, there is a significant trend for steeper (softer) UV spectra in the low-mass sources (see Table 3-1). Figures 3-1 and 3-2 show the final Fe II-subtracted composite spectra normalized by the continuum fits.

To measure the broad emission lines, we use the spectral fitting routine SPECFIT (Kriss 1994), which employs χ^2 minimization. We fit each line with one or more Gaussian profiles, with the understanding that each individual Gaussian component may have no physical meaning by itself. Our goal in fitting the lines is simply to measure the total line strengths free of blends. Our strategy is to obtain the best fit with the least number of free parameters and, when necessary, to use the profile of strong unblended lines, such as C IV, to constrain the fits to weaker or more blended lines. Figure 3-3 shows an example of these fits. Appendix A provides details of our fitting procedure for different lines/blends. Table 3-2 lists the resulting line fluxes relative to Lyα, plus the rest-frame equivalent widths (REWs) as measured above the fitted continuum, and the FWHM of each line. The fluxes, REWs, and FWHMs given in Table 3-2 are from the total fitted profiles, which can include several multiplet components and up to three Gaussian profiles per component (as described in Appendix A).

---

[1] The Image Reduction and Analysis Facility (IRAF) is distributed by the National Optical Astronomy Observatories, which is operated by the Association of Universities for Research in Astronomy, Inc. (USRA), under cooperative agreement with the National Science Foundation.

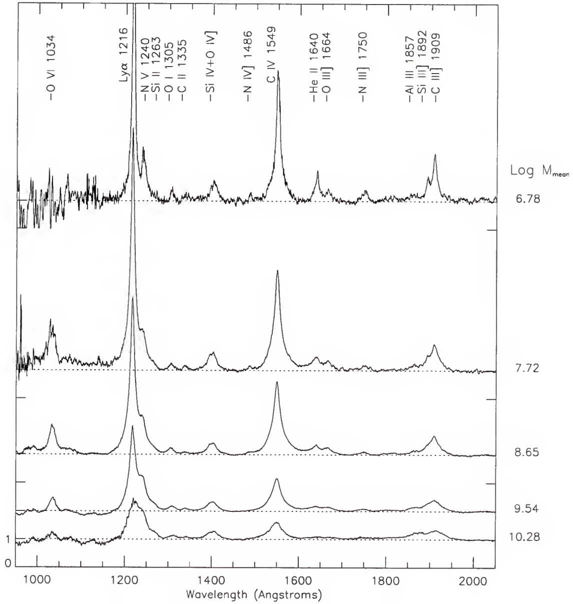

Figure 3–1 Normalized composite spectra are shown for all five SMBH mass bins. The spectra were normalized by a power law continuum fit. The horizontal dashed lines indicate the continuum level for the individual normalized composite spectra, which were vertically shifted for better display. The normalized continuum strength is shown for the spectrum at the bottom of the figure. This same vertical scale applies to all other spectra, although the tick marks for '0' and '1' are not labelled. The mean SMBH mass of each spectra is listed to the right. The Baldwin Effect is clearly seen in these spectra.

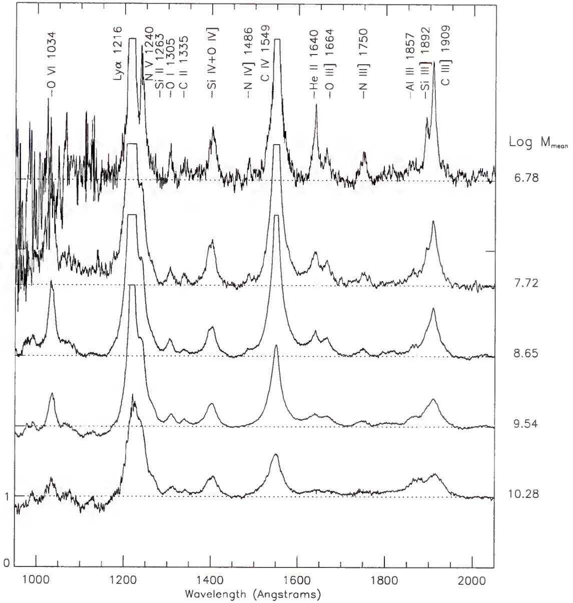

Figure 3–2 Same as Fig. 3-1, but with an expanded vertical scale to display the dependence of the relative strength of weaker emission lines as a function of SMBH mass. Strong emission lines with flat tops are truncated for easier display.

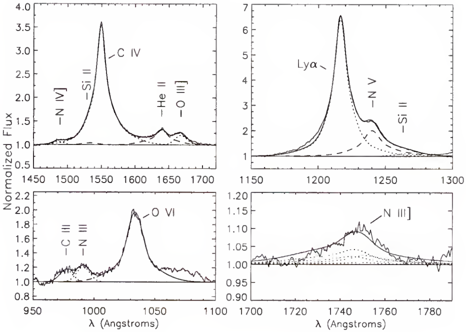

Figure 3–3 Multi-component Gaussian fits (smooth solid curves) to observed emission lines (jagged solid curves) for a composite spectrum of $M \sim 10^8$ M$_\odot$. The continuum is normalized by a power law continuum fit. The continuum (at unity) and composite line fits are plotted. The individual Gaussian components of the fits are shown for the fit to N III] as dotted lines. In the other panels, the dashed and dotted lines represent the sum contribution of each labelled emission line. There is an unidentified bump at ~1070 Å that is not attributed to O VI (see Hamann et al. 1998).

Table 3–2. Emission Line Data

	$10^6 M_\odot$			$10^7 M_\odot$			$10^8 M_\odot$			$10^9 M_\odot$			$10^{10} M_\odot$		
Line	Flux/Lyα	REW[a]	FWHM[b]	Flux/Lyα	REW[a]	FWHM[b]	Flux/Lyα	REW[a]	FWHM[b]	Flux/Lyα	REW[a]	FWHM[b]	Flux/Lyα	REW[a]	FWHM[b]
C III λ977	–	–	–	–	–	–	0.023	2	3830	0.027	2	3170	–	–	–
N III λ991	–	–	–	–	–	–	0.029	3	3830	0.030	2	3170	0.057	2	3350
O VI λ1035	–	–	–	0.207	27	5800	0.242	24	4900	0.299	19	5700	0.396	16	8600
Lyα λ1216	1.000	125	1500	1.000	135	2500	1.000	102	3000	1.000	66	3800	1.000	42	6700
N V λ1240	0.191	24	2100	0.171	23	3100	0.264	27	3800	0.430	29	4700	0.597	25	6500
Si II λ1263	0.010	1	3070	0.012	2	3860	0.022	2	5010	0.026	2	4450	0.047	2	5340
O I λ1303	0.027	4	2000	0.027	4	4110	0.044	5	4650	0.052	4	4600	0.087	4	6320
C II λ1335	0.029	4	4140	0.015	2	3170	0.019	2	5380	0.027	2	4290	0.038	2	4360
Si IV λ1397	0.050	7	4240	0.045	7	5340	0.040	5	5890	0.046	4	6340	0.063	3	7250
O IV] λ1403	0.063	9	4240	0.063	10	5340	0.062	7	5890	0.087	7	6340	0.142	7	7250
N IV] λ1486	0.019	3	2100	0.015	2	3100	0.014	2	3800	0.016[u]	1[u]	4700	0.033[u]	2[u]	6500
Si II λ1531	0.004	1	3070	0.007	1	3640	0.008	1	5010	0.007	1	4450	–	–	–
C IV λ1549	0.556	87	2100	0.547	94	3100	0.597	80	3800	0.462	41	4700	0.500	28	6500
He II λ1640	0.076	13	2300	0.070	13	4200	0.069	10	4300	0.071	7	6500	0.047	3	6800
O III] λ1665	0.046	8	2000	0.049	9	3200	0.046	7	3800	0.049	5	5000	0.068	4	6300
N III] λ1751	0.041	7	2100	0.029	6	3100	0.023	4	3800	0.033	4	4700	0.069	5	6500
Al III λ1859	0.012	2	2050	0.021	4	3460	0.020	3	3630	0.034	4	4430	0.122	9	6690
Si III] λ1892	0.023	4	2050	0.007	1	3460	0.007	1	3630	0.008	1	4430	0.010	1	6690
C III] λ1909	0.192	37	2300	0.130	28	3800	0.125	22	4200	0.135	16	6800	0.203	16	6700

[a] In units of Å

[b] In units of km s^{-1}

[u] Upper limit for N IV]

The primary uncertainty in our flux measurements is the continuum location. We estimate the 1 σ standard deviation of our measurements of the fluxes of C IV and Lyα to be $\lesssim$10% based on repeated estimates with the continuum drawn at different levels. By the same method, we estimate the uncertainty in N V, N III], He II, O III], and other weaker lines to be ~10–20%. These estimates do not include the uncertainties due to line blending, which can be important for some of the weak lines and for N V in the wing of Lyα. The blending and continuum placement uncertainties are both greater for the higher mass spectra because of the broader profiles and generally lower REWs.

3.4 C IV vs. Hβ as a Mass Diagnostic

To test the hypothesis that $R_{\rm BLR}$ for C IV is typically half the value of that for $H\beta$, we compare the measured FWHM of C IV to that of $H\beta$ (see Figure 3-4). If the velocities are virialized and $R_{\rm BLR}$ for C IV is half that of $H\beta$ (§3.2), we expect the FWHM of C IV to be a factor of $\sqrt{2}$ larger than the FWHM of $H\beta$. FWHMs are estimated by an automated program as described in §3.3. There can be separate BLR and Narrow Line Region (NLR) contributions to $H\beta$ (Marziani et al. 1996, Hamann et al. 1997), so each $H\beta$ line is looked at individually. In 5 out of 74 cases, where there is obvious narrow $H\beta$ emission with the same redshift and profile as [O III]λ5007, this narrow emission is clipped off and the FWHM of $H\beta$ is manually estimated. There appears to be no real correlation between the two FWHMs for individual objects, but averages of objects in selected ranges of C IV FWHM fall generally between a 1:1 correlation and the expected $\sqrt{2}$:1 correlation (see Figure 3-4). It should be noted that observations of $H\beta$ and C IV for individual objects were not necessarily made simultaneously, which may contribute to the scatter in Figure 3-4. Five composite spectra, created from objects in selected ranges in SMBH mass (derived from C IV using Eqn. 3.4 and plotted as open boxes with error bars), do appear to be consistent with the expectation that FWHM(C IV) = $\sqrt{2}$ FWHM($H\beta$). All spectra contributing to the composite spectra contain C IV, but only some contain $H\beta$ (see Table 3-1). The narrow component of $H\beta$ was not subtracted from any spectrum before the composite spectra were created. In the composites, the narrow $H\beta$ contribution smoothly blends into the broad-line profile. Filled diamonds represent the averages of objects in selected ranges of C IV FWHM. These averages contain only the individual objects (plotted with + signs in the figure) that have data at both C IV and $H\beta$. Thus, while there is a large scatter among individual sources, the FWHMs of C IVand $H\beta$ generally scale as expected in both the composite spectra and the averages of individual objects. Also note that any offsets in Fig. 3-4 affect only the absolute SMBH masses, with an uncertainty of up to a factor of two, but do not affect any trends with SMBH mass.

We also estimate the SMBH mass derived from C IV and the SMBH mass derived from $H\beta$. Masses are derived from $H\beta$ using Eqns. 3.1 and 3.2. We compare the two masses for all objects in our sample that have observations of both lines (see Figure 3-5). Filled diamonds represent the averages of objects in selected ranges of SMBH mass (as derived from C IV). As in Fig. 3-4, these averages contain only the individual objects that have data at both C IV and $H\beta$. We find that that there is approximately a 1:1 correlation between the mass obtained from C IV and that obtained from $H\beta$. There can be significant deviations from this for individual objects, but the relation holds well for averages of many objects. Hereafter, we will discuss only the masses obtained from C IV.

3.5 Results

3.5.1 SMBH Mass vs. Redshift, Luminosity, and FWHM

Figure 3-6 shows the redshift distribution of the entire sample as a function of SMBH mass. The sample was designed to span the widest possible range of luminosity at each redshift, and the distribution of points in Fig. 3-6 closely

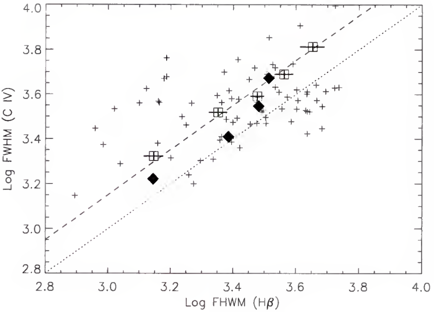

Figure 3–4 Comparison of the measured FWHM of C IV to that of $H\beta$ for all objects in our sample with observations of both lines. In five cases, obvious narrow $H\beta$ emission was subtracted prior to measuring its FWHM. The open boxes represent five composite spectra created from objects in selected ranges of SMBH mass. The error bars drawn on the boxes represent the ± 1σ ranges for the FWHMs of C IV and $H\beta$ for these composite spectra. The filled diamonds represent averages of objects in selected ranges of C IV FWHM (< 2000 km/s, 2000–3000 km/s, 3000–4000 km/s, and 4000–6000 km/s). The dotted line is a 1:1 ratio and the dashed line is the expected ratio of FWHM(C IV) = $\sqrt{2}$ FWHM($H\beta$).

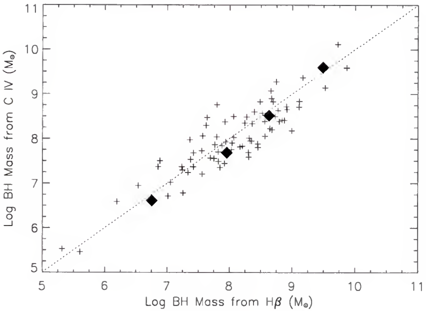

Figure 3–5 Comparison of the SMBH mass derived from C IV to that derived from $H\beta$ for all objects in our sample with observations of both lines. The filled diamonds represent averages of objects in selected SMBH mass ranges. The dotted line is a 1:1 ratio (the RMS scatter about the 1:1 relationship is 0.39 for the individual objects and 0.17 for the averages). For composite spectra of many objects, both methods yield approximately the same mass.

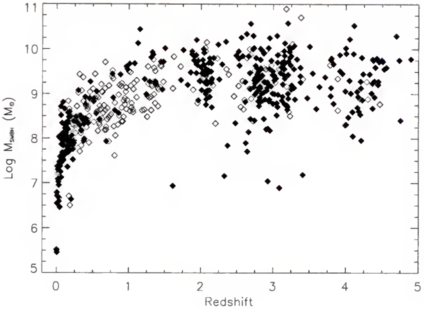

Figure 3–6 Redshift distribution of the AGN sample as a function of SMBH mass. The filled diamonds represent radio-quiet quasars and the open diamonds represent radio-loud quasars. There is clearly no trend in SMBH mass with redshift (for $z \gtrsim 0.3$).

follows the distribution in L vs. z (see Dietrich et al. 2002). There is no trend in SMBH mass with redshift. We expect SMBH mass to correlate with both continuum luminosity and FWHM because we derived our mass estimates from these quantities (Eqn. 3.4). Continuum luminosity is plotted as a function of SMBH mass in Figure 3-7, and shows the expected trend with little scatter. This relationship is much tighter than the relationship with the FWHM of C IV (see Figure 3-8), even though our SMBH mass estimates depend more sensitively on FWHM than luminosity. This may be due to the larger dynamic range in luminosity compared to FWHM (see Netzer 2003 for further discussion). In all three plots (Figs. 3-6, 3-7, and 3-8), no trend is seen based on radio loud vs. radio quiet objects.

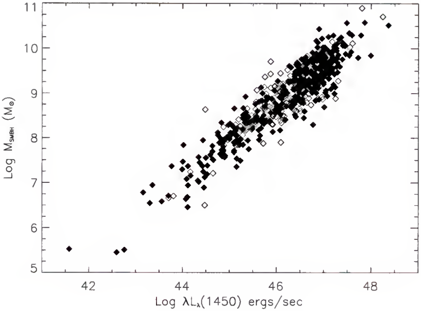

Figure 3–7 Continuum luminosity versus SMBH mass. There is a very strong correlation with little scatter. Symbols as in Fig. 3-6.

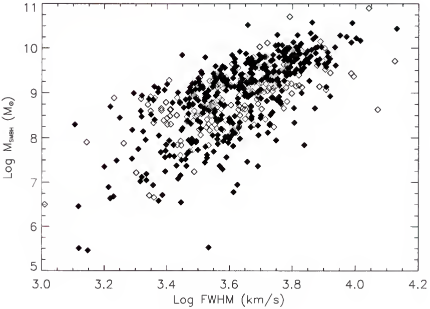

Figure 3–8 The FWHM of C IV versus SMBH mass. A trend is seen, but with a large amount of scatter. Symbols as in Fig. 3-6.

3.5.2 Line Properties versus SMBH Mass

The Baldwin Effect is an observed anti-correlation between continuum luminosity (and thus SMBH mass, since that is estimated based on luminosity) and the equivalent widths of emission lines such as C IV, Lyα, C III], and O VI (see Baldwin 1977; Croom et al. 2002; Dietrich et al. 2002; Espey et al. 1993; Osmer et al. 1994, Osmer & Shields 1999; Zheng & Malkan 1993). Interestingly, the Baldwin Effect is not seen in N V even though it seems to be present to some extent in N III]. Dietrich et al. (2002) discuss the Baldwin Effect of this same sample sorted by continuum luminosity. The Baldwin Effect is also evident in our spectra sorted by $M_{\rm SMBH}$. Figure 3-9 plots rest-frame equivalent widths as a function of SMBH mass (see also Figs. 3-1 & 3-2). Al III curiously does not show the Baldwin Effect in these composite spectra and, if anything, its equivalent width actually increases with SMBH mass. This is contrary to its behavior in Dietrich et al. (2002) when sorted by continuum luminosity. The rest of the lines plotted in Fig. 3-9 show generally the same behavior as in Dietrich et al. (2002). Dietrich et al. (2002) find that the slope of the Baldwin Effect becomes steeper in most lines at higher luminosities. We observe a similar trend for steeper slopes at higher SMBH masses with the notable exception of N III], which slightly increases in REW at higher SMBH masses.

3.5.3 Metallicity versus SMBH Mass

Figure 3-10 shows the metallicities inferred by comparing emission line flux ratios for each composite spectrum to the theoretical results in Hamann et al. (2002). We obtain our metallicity estimates by comparing the emission line flux ratios to plots of metallicity vs. line ratio based on theoretical models (see Figure 5 in Hamann et. al 2002 and Figure 3 in Warner et al. 2002). We prefer to estimate the metallicities based on the calculations in Hamann et al. that use a segmented powerlaw for the photoionizing continuum shape. This continuum shape is a

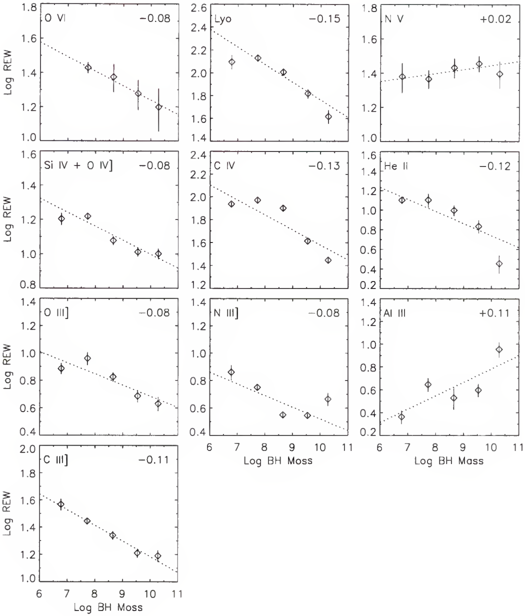

Figure 3-9 Emission line equivalent widths as a function of SMBH mass. We calculated linear fits to the EWs for the entire SMBH mass range using a chi-square minimization routine (dotted lines). The slopes of these fits are given in the upper right hand corner of each plot.

good approximation to the average observed continuum in quasars (Zheng et al. 1997; Laor et al. 1997). It also yields intermediate results for line ratios, such as N V/He II, that are sensitive to the continuum shape (see below).

The uncertainties in the metallicities shown in Figure 3-10 derive simply from the 1σ measurement uncertainties discussed in §3.3. They do not reflect the theoretical uncertainties in the technique we use to derive metallicities from the line ratios (see Hamann et al. 2002 for discussion). Also note that there is a larger statistical uncertainty in the lowest mass composite spectrum, because it is composed of only nine objects (the small number of spectra in this composite make it easier for one or two objects to dominate the composite).

Our best estimate of the overall metallicity from each spectrum (labeled as Average in Fig. 3-10) is obtained by averaging the results of N III]/C III], N III]/O III], N V/C IV, and N V/O VI. We select these ratios because we believe they are the most accurately measured ratios and the most reliable from a theoretical viewpoint (Hamann et al. 2002).

We believe the ratios involving N IV] are less reliable for several reasons. First, the N IV] flux is difficult to measure because this line is weak and in the wing of the much stronger C IV line profile. Second, ratios such as N IV]/C IV, which compare a permitted and intercombination line, are potentially more sensitive to uncertainties in the line optical depths and radiative transfer. Third, perhaps as a consequence of the greater uncertainties in N IV], there is more object-to-object scatter in the results derived from N IV] compared to N III] (Hamann et al. 2002). We also exclude N V/He II from our estimate of the average metallicity because i) this ratio compares a collisionally excited line (N V) to a recombination line (He II), and ii) it can yield (for this continuum shape) very high metallicities that are obtained by extrapolations beyond the theoretical results calculated by Hamann et al. (2002).

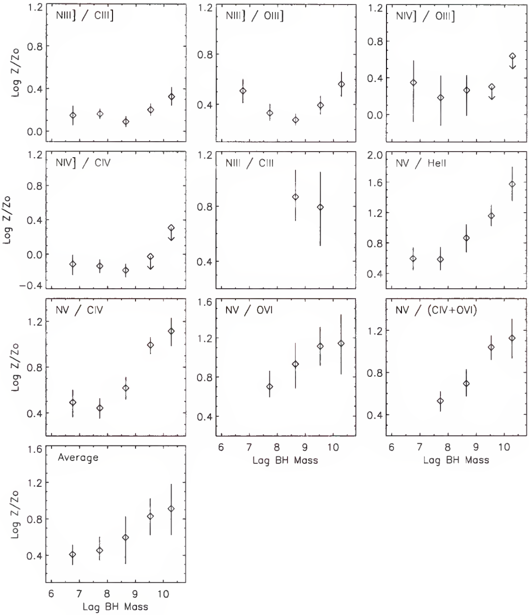

Figure 3–10 Metallicities derived from comparisons of different line ratio diagnostics to theoretical results from Figure 5 in Hamann et al. (2002) are shown as a function of SMBH mass. The average includes N III]/C III], N III]/O III], N V/C IV, and N V/O VI.

All of the line ratios involving N III] and N V show N/O and N/C ratios that are solar or greater. This implies a metallicity of $\gtrsim 1\ Z_\odot$ if N is mostly secondary.

3.5.4 Do N III] and N V Disagree?

All four ratios involving N V show a strong trend in metallicity with SMBH mass. The slope of this trend is not linear and seems to increase as mass increases. The ratios involving N III], however, show no apparent correlation between metallicity and SMBH mass. We believe that this apparent discrepancy between the two ratios may be due to the large FWHMs and small REWs of the emission lines in the composite spectra representing higher SMBH masses.

The spectra representing higher SMBH masses have broader lines because the mass derivation depends on the line FWHM (Eqn. 3.4). This may lead to systematic overestimating of the continuum if the wings of the lines blend together and never quite reach the continuum level. In particular, notice the interval around 1460 Å (see Figs. 3-1 and 3-2) that we used to constrain our continuum fits (see §3.3). In the higher mass spectra, C IV and Si IV + O IV] seem to blend together, never quite reaching the true continuum, and instead forming a "U" shape. This effect of overestimating the continuum could lead to underestimates of N III] and N IV] in the higher mass spectra and thus negate or weaken any real trend between SMBH mass and the flux ratios involving these lines. For example, we find that a drop in the continuum level of only 5% will more than double the measured flux in N III] and N IV], but increase the flux in stronger lines by only ∼ 15% to 30%.

In order to more thoroughly examine the effects of FWHM on the measured line fluxes, we sort the quasar spectra by the FWHM of C IV and create composite spectra for different ranges in FWHM. We then fit the continuum and measure the emission line fluxes as described in §3.3. The resulting line ratios are plotted in Figure 3-11. We find that the flux ratio of C III]/C IV remains roughly constant at different line widths, but N III]/N V declines as the lines get broader. Because of

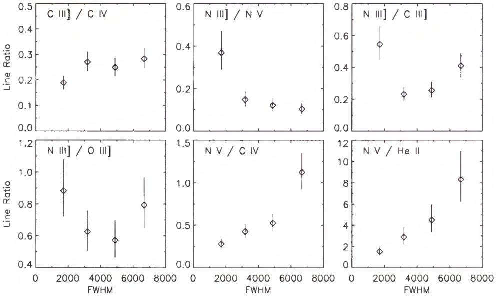

Figure 3–11 Emission line ratios are shown as a function of the FWHM of C IV.

this, we again see a discrepancy in metallicity trends between ratios involving N III] and those involving N V. The ratios involving N V indicate increasing metallicity with increasing line width. This is expected because objects with broader emission lines should have higher black hole masses and thus higher metallicities (§3.1). The N III] ratios, however, show a "U"-like behavior in Figure 3-11, with the narrowest lines having the highest metallicity. The composite spectrum with the narrowest lines is also the only one in which the metallicities derived from N III] ratios agree with those derived from N V ratios.

There are two possible explanations for the discrepancy between the line ratios. The first possibility is that N V is somehow enhanced in quasars with broader emission lines (and/or larger L and M_{SMBH}) by a process that we do not understand. Several studies have suggested that Lyα photons scattered in a broad absorption-line wind could enhance N V (Surdej & Hutsemekers 1987; Turnshek et al. 1988; Hamann et al. 1993; Turnshek et al. 1996; Krolik & Voit 1998). However, other studies have presented strong evidence that the scattering contributions to N V are typically small (Hamann & Korista 1996; Hamann et al. 2002). The second possibility is that we are systematically overestimating the continuum and thus underestimating the flux of N III] in spectra with broader lines. There is evidence supporting the latter hypothesis in that N III]/N V and C III]/C IV behave similarly in our overall quasar sample. In particular, when N III]/N V is larger/smaller than average, C III]/C IV is also larger/smaller by roughly the same factor. The intercombination lines scale roughly together compared to the permitted lines of the same element. The somewhat different behaviors of N III]/N V and C III]/C IV in Figure 3-11 (sorted by FWHM) therefore suggest that we are underestimating the weak N III] line in the broader line sources. The U-like shape of the N III]/O III] and N III]/C III] points in this figure could then be caused by an increasing underestimate of N III] as the FWHM increases from ~2000 km s^{-1} to ~5000 km s^{-1}, offset by the increasing N/O and N/C abundance ratios for FWHM $\gtrsim$ 5000 km s^{-1}. Thus, we believe this is the more likely scenario. This scenario may also explain the fact that the metallicities derived from all ratios agree for objects with narrow emission lines (see also Warner et al. 2002; Baldwin et al. 2003), in which the continuum is unlikely to be systematically overestimated.

3.6 Discussion

Our main result from §3.5 is that the data are consistent with a trend between BLR metallicity and SMBH mass. The hypothesis motivating this work (§3.1) was that there should be a trend between metallicity and SMBH mass with roughly the same slope as the mass-metallicity relation in elliptical galaxies if the BLR gas was enriched by stars in the AGN's host galaxy. We use a plot of Mg_2 index vs. velocity dispersion, σ, in Bender et al. (1993) to estimate the slope of the galactic mass-metallicity relation. Mg_2 index is a line strength parameter used to derive metallicities. Bender et al. (1993) derive $\log(Mg_2) \propto 0.41 \log(Z/Z_\odot)$ and $\log(Mg_2) \propto 0.20 \log(\sigma)$. Using these proportionalities, along with $M \propto \sigma^2$, we obtain an estimate of the slope of the mass-metallicity relation in log space,

$\Delta Z/\Delta M \sim 0.24$. We obtain a similar estimate ($\Delta Z/\Delta M \sim 0.34$) using a plot of [O/H] vs. absolute blue magnitude in Zaritsky et al. (1994) combined with a plot of $\log(L_B)$ vs. $\log(M)$ in van Albada et al. (1995). We also derive $\log(Z) \propto 0.38 \pm 0.07 \log(M_{\rm SMBH})$ from the $[Z/\rm{H}] \propto 0.76 \pm 0.13 \log(\sigma)$ relation given in Trager et al. (2000). We employ a χ^2 minimization routine to obtain linear fits to the plots of metallicity vs. SMBH mass shown in Figure 3-10. These fits yield a slope of $\Delta Z/\Delta M \sim 0.2 - 0.3$ for all ratios involving N V. This is consistent with the slope of the mass-metallicity relation in elliptical galaxies as expected. The slope for the average metallicity vs. SMBH mass is ~0.2, slightly lower than the slopes for the N V ratios. The slope for ratios involving N III] is ~0, but the slope from only the three highest mass spectra for these ratios is $\sim 0.1 - 0.2$. This may be a lower bound on the slope of metallicity vs. SMBH mass because in the highest mass spectra, the increasing N/O and N/C abundance ratios are starting to dominate the underestimation of N III] caused by the systematic overestimation of the continuum in spectra with broad lines.

It should be noted that the quasar-BLR metallicities are several times higher than the galactic values derived in the studies listed above. This apparent discrepancy can be understood in the context of normal galaxy evolution. Quasar BLRs sample an earlier evolutionary stage and frequently a different physical location in galaxies compared to the H II regions or average spectra of stars in present day galaxies (Hamann & Ferland 1999). However, the similar slope of the mass-metallicity relationship in both quasars and galaxies supports the premise that the gas in the BLR was processed/enriched by the surrounding stellar population.

The evidence presented here for a mass-metallicity relationship among quasars does not prove that SMBH mass is the fundamental parameter affecting BLR metallicity. However, in these composite spectra, sorted by SMBH mass, the slope of the trend between *luminosity* and metallicity is at least as steep as (and possibly marginally steeper than) the slope is for composite spectra sorted by luminosity (see Dietrich et al. 2002; Dietrich et al. 2003b). Also, composite spectra created from different ranges in Eddington ratio, L_{bol}/L_{edd}, show a slight trend with luminosity, but no trend with either SMBH mass or metallicity (see Warner et al. 2004). These results suggest that SMBH mass could be the fundamental parameter. Further support for mass as the fundamental parameter comes from the similarity of the mass-metallicity relationship among quasars to the corresponding relationship among galaxies. These ideas are also consistent with the growing evidence (e.g., Shields et al. 2003) for a close relationship between quasars and their host galaxies. In particular, the relationship between SMBH mass and host galaxy mass (see refs. in §3.1) indicates that i) SMBHs are a natural byproduct of galaxy formation, and ii) essentially all massive galaxies were at one time "active." Quasars at high redshifts are signposts of the last stages in the formation of these massive SMBHs in the cores of young galactic spheroids. The high metallicities near these objects reported here and elsewhere (Constantin et al. 2001; Dietrich et al. 1999, 2003; Hamann 1997; Hamann & Ferland 1999; Hamann et al. 2002; Osmer et al. 1994; Petitjean et al. 1994; Warner et al. 2002) imply that the gas has *already* (at the quasar epoch) been substantially processed/enriched by multiple generations of massive stars. This rapid evolution at high redshifts, though, is well within the parameters derived in some recent simulations, which show that the densest protogalactic condensations can form stars and reach solar or higher metallicities at $z \gtrsim 6$ (Gnedin & Ostriker 1997; Haiman & Loeb 2001).

3.7 Summary and Conclusions

We have investigated a large sample of 578 AGNs for a trend between metallicity and SMBH mass. The sample covers a redshift range from $0 \lesssim z \lesssim 5$, six orders of magnitude in luminosity, and five orders of magnitude in SMBH mass. We estimate SMBH masses using the virial theorem and formulae given in Kaspi et al. (2000). To improve the signal-to-noise ratio and average over object-to-object variations, we produce composite spectra representing each decade in SMBH mass. Composite spectra allow us to better measure weak emission lines and minimize the influence of irregularities in any individual quasar. After a powerlaw continuum fit, multi-component Gaussian profiles are fit to emission lines to measure their fluxes. Metallicities are then estimated by comparing emission line ratios involving nitrogen to theoretical predictions in Hamann et al. (2002). Our main results are as follows.

1) We estimate SMBH masses based on both C IV and $H\beta$ and find approximately a 1:1 correlation for averages of many objects (Fig. 3-5). We conclude that it is valid to use C IV instead of $H\beta$ to estimate average black hole masses in samples of AGNs.

2) There is no trend between SMBH mass and redshift, but as expected, SMBH mass shows a positive correlation with both luminosity and the FWHM of C IV.

3) We observe the usual Baldwin Effect in composite spectra representing different ranges in SMBH mass. In agreement with other studies (see Dietrich et al. 2002), N V does not show the Baldwin Effect even though it seems to be present to some extent in N III]. However, Al III curiously does not exhibit the Baldwin Effect either, and if anything, its REW actually increases with increasing SMBH mass.

4) We find a trend in metallicity with SMBH mass for emission line ratios involving N V, but not for those involving N III] or N IV]. This is consistent with the findings of Dietrich et al. (2002). They find a lack of a Baldwin Effect for N V, which in the present study leads to emission line ratios involving N V increasing with increasing luminosity. However, Dietrich et al. (2003a, 2003b) find that metallicities derived from ratios involving both N III] and N V yield results of solar or greater, for samples of 70 high redshift ($3.9 \lesssim z \lesssim 5.0$) quasars.

5) We conclude that the data are consistent with a trend between SMBH mass and metallicity and some of the data (N V ratios) indicate that there is a very strong trend. N III] seems to indicate no trend; however, upon further examination, we believe that the uncertainties in N III] and N IV] are too large to confirm or test any trend. We note that the correlation between SMBH mass and FWHM may lead to systematic overestimates of the continuum and thus underestimates of N III] and N IV] in the higher mass spectra.

6) We estimate the slope of the galactic mass-metallicity relationship in log space to be $\Delta Z/\Delta M \sim 0.2 - 0.3$ (see §3.6). This slope is consistent with linear fits to the plots of metallicity vs. SMBH mass in Fig. 3-10 that are derived from ratios involving N V, as well as the plot of "average" metallicity vs. SMBH mass. The similarity in the slope of the mass-metallicity relationship in both quasars and galaxies supports the premise that the gas in the BLR was processed/enriched by the surrounding stellar environment and contributes to the growing evidence for a close relationship between quasars and their host galaxies.

CHAPTER 4

ACTIVE GALACTIC NUCLEI EMISSION-LINE PROPERTIES VERSUS EDDINGTON RATIO

4.1 Introduction

The central engines of quasars, and more generally, active galactic nuclei (AGNs) are believed to be powered by supermassive black holes (SMBHs). Two of the fundamental properties of AGNs are the SMBH mass and the accretion rate of material onto the SMBH. Several indirect methods have been devised to estimate SMBH masses. One set of these methods assumes that the broad emission-line region (BLR) is in gravitational equilibrium with the central source, so that the SMBH mass can be estimated by applying the virial theorem, $M_{\rm SMBH} = rv^2/G$, to the measured line widths (Peterson 1993; Peterson 1997; Wandel et al. 1999; Kaspi et al. 2000; McLure & Dunlop 2001; Vestergaard 2002). In reverberation mapping studies, $R_{\rm BLR}$, the radial distance between the central source and the BLR can be estimated from the lag time between continuum variations and the emission-line response (Peterson 1993; Peterson 1997; Wandel et al. 1999; Kaspi et al. 2000). These reverberation mapping studies have demonstrated an observed relation of $R_{\rm BLR} \propto \lambda\, L_\lambda(5100\ \text{Å})^{0.7}$ that can be used to estimate R_{BLR} for AGNs over a wide range of redshifts (Kaspi et al. 2000; McLure & Dunlop 2001; Vestergaard 2002; Corbett et al. 2003; Warner et al. 2003). Netzer (2003) has argued that the slope is not known to an accuracy better than about 0.15.

A second set of methods is based on the tight correlation between the masses of SMBHs and the velocity dispersions, σ, of their host galaxy spheroidal components (Ferrarese & Merritt 2000; Gebhardt et al. 2000; Merritt & Ferrarese 2001; Tremaine et al. 2002). However, stellar velocity dispersions are not easy to measure for AGN hosts, especially at high redshifts. Because of this, methods have been devised using proxies of the velocity dispersion, such as the width of the narrow emission line [O III] λ5007 (Nelson 2000; Boroson 2003; Shields et al. 2003) or the bulge luminosity, L_{bulge} (Magorrian et al. 1998; Laor 1998; Wandel 1999). Early studies showed a large scatter, as much as two orders of magnitude between SMBH mass and L_{bulge} (Ferrarese & Merritt 2000). However, more recent studies that carefully model the bulge light profiles of disk galaxies and thus obtain more accurate values of L_{bulge} show less scatter in $M_{\rm SMBH} - L_{\rm bulge}$, similar to that in the $M_{\rm SMBH} - \sigma$ relationship (McLure & Dunlop 2002; Erwin et al. 2002; Bettoni et al. 2003). Recently, SMBH mass has also been shown to correlate strongly with the global structure of bulges and ellipticals, such that more centrally concentrated bulges have more massive SMBHs. This relationship is as strong as the $M_{\rm SMBH} - \sigma$ relationship with comparable scatter (Graham et al. 2001; Erwin et al. 2002).

Once the SMBH mass has been estimated, the Eddington luminosity can be calculated as $L_{edd} = 1.26 \times 10^{38} M_{\rm SMBH}$ ($\rm M_\odot$) ergs s^{-1} (e.g., Rees 1984; Peterson 1997). Eddington luminosity is the limit in which the inward gravitational force acting on the gas exactly balances the outward radiation force induced by electron scattering. It can be thought of as the maximum possible luminosity for an object of mass $M_{\rm SMBH}$ that is powered by *spherical* accretion (Peterson 1997). The Eddington luminosity can be exceeded if accretion is not spherically symmetric (see §4.5, also Osterbrock 1989; Begelman 2002; Collin et al. 2002; Wang 2003). AGN luminosities should be directly proportional to the accretion rate, $L \propto \dot{M}_{acc}$, and therefore the ratio, $L/L_{edd} \propto \dot{M}_{acc}/M$, is an indirect measure of the accretion rate relative to the critical Eddington value.

Narrow Line Seyfert 1s (NLS1s) are a subclass of Seyfert 1s that exhibit distinct and unusual properties: very narrow broad emission lines ($H\beta$ FWHM < 2000 km s^{-1}) with [O III] λ5007 / $H\beta$ ratios of less than 3 (to exclude Seyfert

2s), strong Fe II emission, and unusually strong big blue bumps (Osterbrock & Pogge 1985; Kuraszkiewicz et al. 2000; Constantin & Shields 2003). NLS1s also land at one extreme end of the Boroson & Green (1992) Principal Component 1 (PC1). It has been suggested that PC1 is strongly correlated with L/L_{edd} (Boroson & Green 1992; Boroson 2002; Shemmer & Netzer 2002; Constantin & Shields 2003). Several studies have suggested that NLS1s have low SMBH masses for their luminosities, and thus very high Eddington ratios, near 1 (Mathur 2000; Kuraszkiewicz et al. 2000; Shemmer & Netzer 2002; Shemmer et al. 2003). It has also been suggested that NLS1s have unusually high metallicities for their luminosities (see §4.4.4 and Figure 4-11 below, Mathur 2000; Shemmer & Netzer 2002; Shemmer et al. 2003). Shemmer & Netzer (2002) find that NLS1s depart from the nominal relationship between metallicity and luminosity in AGNs (Hamann & Ferland 1999; Dietrich et al. 2003b), with some NLS1s indicating metallicities as high as those measured in high-luminosity, high-redshift quasars. Because of their high metallicities and high Eddington ratios, Mathur (2000) proposed that NLS1s are analogs of high-redshift ($z \gtrsim 4$) quasars, in that they may both be in an early evolutionary phase, residing in young host galaxies.

We have collected a large sample of 578 spectra of "Type 1" AGNs (quasars and Seyfert galaxies with broad emission lines) that span the rest-frame UV wavelengths needed for this study (Dietrich et al. 2002). We compute composite spectra from different ranges in the Eddington ratio, L/L_{edd}. We include a composite spectrum produced from a subsample of 26 NLS1s for comparative analysis. We present measurements of the emission lines in these composite spectra and investigate their relationship to L/L_{edd}.

4.2 Eddington Ratio Determinations

We first estimate SMBH masses by applying the virial theorem, $M_{\rm SMBH} = rv^2/G$, to the line-emitting gas (for more details, see also Kaspi et al. 2000;

Peterson & Wandel 2000; McLure & Dunlop 2001; Vestergaard 2002; Corbett et al. 2003; Warner et al. 2003). Kaspi et al. (2000) express the SMBH mass as

$$M_{SMBH} = 1.5 \times 10^5 \mathrm{M}_\odot \left(\frac{R_{\mathrm{BLR}}}{\mathrm{lt-days}}\right) \left(\frac{\mathrm{FWHM}}{10^3 \mathrm{~km~s^{-1}}}\right)^2 \tag{4.1}$$

R_{BLR} is the radial distance between the BLR and the central source, and FWHM applies to the broad emission line profile. We estimate R_{BLR} based on the observed relation between R_{BLR} for a particular line and the continuum luminosity (Wandel et al. 1999; Kaspi et al. 2000; Vestergaard 2002; Corbett et al. 2003). A particular line must be specified because reverberation studies have shown that the BLR is radially stratified, such that higher ionization lines tend to form closer to the central engine than lower ionization lines (Peterson 1993).

We select the C IV λ1549 emission line instead of $H\beta$ to estimate SMBH masses because it is more readily observed across the entire redshift range from $z \sim 0$ to $z \sim 5$. We find that there is approximately a 1:1 correlation between the SMBH mass obtained from C IV and that obtained from $H\beta$. There can be significant deviations from this for individual objects, but the relation holds well for averages of many objects and for measurements based on composite spectra (see Vestergaard 2002; Warner et al. 2003 for further discussion).

Reverberation studies indicate that the radius of the BLR for C IV is about half that of $H\beta$ (Stirpe et al. 1994; Korista et al. 1995; Peterson 1997; Peterson & Wandel 1999). We therefore modify the equation given by Kaspi et al. (2000) to obtain

$$R_{\mathrm{BLR}}(\mathrm{CIV}) = 9.7 \left[\frac{\lambda L_\lambda(1450\text{Å})}{10^{44} \mathrm{~ergs~s^{-1}}}\right]^{0.7} \mathrm{~lt-days} \tag{4.2}$$

See Warner et al. (2003) for more details. From Equations (4.1) and (4.2), we derive

$$M_{SMBH} = 1.4 \times 10^6 \mathrm{M}_\odot \left(\frac{\mathrm{FWHM(CIV)}}{10^3 \mathrm{~km~s^{-1}}}\right)^2 \left(\frac{\lambda L_\lambda(1450\text{Å})}{10^{44} \mathrm{~ergs~s^{-1}}}\right)^{0.7} \tag{4.3}$$

Vestergaard (2002) calibrated mass derivations based on C IV against estimates using FWHM($H\beta$) and direct measurements of $R_{\rm BLR}(H\beta)$ from reverberation mapping. Her technique yields essentially the same mass relationship (within 10%) as Equation (4.3), which helps to confirm the factor of 2 scaling adopted here between $R_{\rm BLR}$(C IV) and $R_{\rm BLR}(H\beta)$. Vestergaard (2002) finds that SMBH masses estimated by applying this equation to single-epoch spectra of individual objects have a 1σ uncertainty of a factor of three when compared to studies that use $H\beta$ and a direct, reverberation measure of the BLR radius. Our composite spectra average over variabilities and object-to-object scatter, which should significantly reduce the uncertainties. See also Krolik (2001), Netzer (2003), Corbett et al. (2003), and Vestergaard (2004) for further discussion of the uncertainties.

We next estimate bolometric luminosities, L, based on an integration over a typical quasar continuum shape. We use the cosmological parameters $\rm H_0 = 65$ km $\rm s^{-1}$ $\rm Mpc^{-1}$, $\Omega_M = 0.3$, and $\Omega_\Lambda = 0$ (Carroll, Press, & Turner 1992) throughout this paper[1] . We assume a segmented powerlaw of the form $F_\nu \propto \nu^\alpha$ to approximate the continuum shape, with $\alpha = -0.9$ from 0.1 Å to 10 Å, $\alpha = -1.6$ from 10 Å to 1000 Å, and $\alpha = -0.4$ from 1000 Å to 100,000 Å (Zheng et al. 1997; Laor et al. 1997; Brotherton et al. 2001; Vanden Berk et al. 2001; Dietrich et al. 2002). It is now well established that the mean UV–IR slope is a function of luminosity (see Dietrich et al. 2002). For the luminosity range spanned by our sample, the average powerlaw index between 1000 Å and 100,000 Å ranges from $\sim$ -0.2 to $\sim$ -0.6 (M. Dietrich, private communication). This range could cause a scatter of $\sim$ 20% in our estimates of L.

---

[1] The use of this cosmology was motivated for comparison with earlier studies in the pre-WMAP era. Furthermore, the difference between our set of cosmological parameters and those suggested by WMAP results in a difference of less than 20% in luminosity for a wide redshift range of $0 < z < 4$.

Integrating this nominal spectrum over all wavelengths implies bolometric corrections of 4.36 and 9.27 for $\lambda L_\lambda(1450\text{Å})$ and $\lambda L_\lambda(5100\text{Å})$, respectively. These corrections are slightly lower than the correction of 11.8 to $\lambda L_\lambda(5100\text{Å})$ derived by Elvis et al. (1994), but in good agreement with more recent derivations (Kaspi et al. 2000; Vestergaard 2004). We use this bolometric correction and SMBH masses from Equation (4.3) to obtain Eddington ratios:

$$\frac{L}{L_{edd}} = 1.6\left(\frac{\text{FWHM(CIV)}}{10^3\ \text{km s}^{-1}}\right)^{-2}\left(\frac{L}{10^{44}\ \text{ergs s}^{-1}}\right)^{0.3} \tag{4.4}$$

4.3 Data and Analysis

Our sample is comprised of 578 Type 1 (broad-line) AGN spectra with rest-frame UV wavelength coverage that encompasses the range $950 \lesssim \lambda \lesssim 2050$ Å. The spectra were obtained by several groups using various ground-based instruments as well as the *Hubble Space Telescope (HST)* and the *International Ultraviolet Explorer (IUE)* (see Dietrich et al. 2002 and 2004, in prep for more details). The sample spans a redshift range from $0 \lesssim z \lesssim 5$, seven orders of magnitude in luminosity, and five orders of magnitude in SMBH mass. One unique aspect of this sample is that it contains new observations of faint quasars at redshift $z > 2.5$ (e.g., Steidel et al. 2002, Dietrich et al. 2002). Thus we can avoid to some degree the bias toward higher luminosities at higher redshifts inherent in magnitude-limited samples. The sample spans at least three orders of magnitude in luminosity at all redshifts (see Fig. 4-1 in Dietrich et al. 2002). We determined the radio loudness for the quasars using the radio flux densities given in Véron-Cetty & Véron (2001). We used the definition of radio loudness given by Kellermann et al. (1989). Our classifications of radio-loud quasars are consistent with classifications available in the literature (Wills et al. 1995; Bischof & Becker 1997; Wilkes et al. 1999; Stern et al. 2000).

We use an automated program to estimate the FWHM of C IV in each spectrum (see Warner et al. 2003 for details). Comparisons between the FWHMs estimated by the program and those measured manually indicate an error of $\lesssim 10\%$ in the automated results. Lines containing significant absorption are flagged by the program and their FWHMs are estimated manually (by interpolating across the absorption feature). We use the FWHM of C IV and the continuum luminosity, $\lambda L_\lambda(1450\text{Å})$, to estimate the central SMBH mass and L/L_{edd} for each quasar based on the equations given in §4.2.

We then sort the quasars by L/L_{edd} into seven bins (see Figure 4-1): $L/L_{edd} < 0.25$, $0.25 \leq L/L_{edd} < 0.33$, $0.33 \leq L/L_{edd} < 0.50$, $0.50 \leq L/L_{edd} < 0.67$, $0.67 \leq L/L_{edd} < 1.00$, $1.00 \leq L/L_{edd} < 2.00$, and $L/L_{edd} \geq 2.00$, and compute seven composite spectra. Each composite spectrum is the average of all the quasar spectra in a bin. Table 4-1 lists various parameters for the composites, including the mean values of $M_{\rm SMBH}$, L, FWHM(C IV), L/L_{edd}, and the redshift, z, as measured from the individual objects contributing to each composite. Also listed are the numbers of objects contributing at the wavelength of the C IV emission line. The spectral slopes, α, are measured from each composite spectrum and constrained by the flux in 20 Å wide windows centered at 1450 Å and 1990 Å.

Calculating composite spectra significantly improves the signal-to-noise ratio and averages over object-to-object variations. Since narrow absorption features may affect the emission line profiles in composite spectra, we developed a method to detect strong narrow absorption features. The contaminated spectral region of the individual spectrum is then excluded from the calculation of the composite spectrum. For more details about creating composite spectra, see Brotherton et al. (2001), Vanden Berk et al. (2001), Dietrich et al. (2002), and Warner et al. (2003)

For comparison with the L/L_{edd} composites, we also create composite spectra for different ranges in SMBH mass ($10^6 - 10^7$ M$_\odot$, $10^7 - 10^8$ M$_\odot$, $10^8 - 10^9$ M$_\odot$,

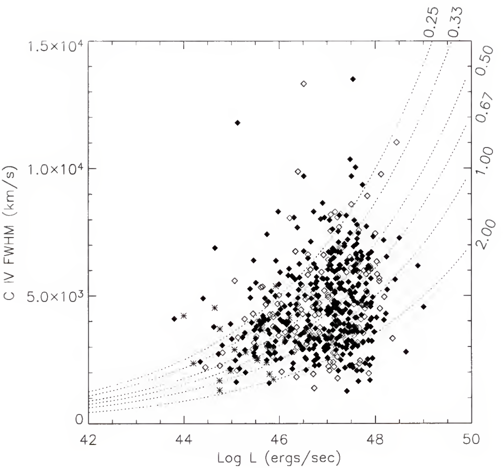

Figure 4–1 Distribution of the two measured quantities. The dotted lines represent constant L/L_{edd} ratios, with values indicated at the right. We created composite spectra for each of the seven ranges in Eddington ratio shown above. The filled diamonds represent radio-quiet quasars, the open diamonds represent radio-loud quasars, and the asterisks represent NLS1s.

Table 4–1 Composite Parameters

L/L_{edd}	α	# Objects at C IV	z	Log L [ergs s^{-1}]	FWHM(C IV) [km s^{-1}]	Log $M_{\rm SMBH}$ [$M_\odot$]
L/L_{edd} Composites						
0.17	-0.65	64	1.06	46.84	6900	9.48
0.30	-0.56	62	1.17	47.17	5600	9.60
0.41	-0.49	106	1.62	47.16	5100	9.44
0.58	-0.40	85	1.83	47.43	4600	9.56
0.83	-0.60	90	1.93	47.37	3900	9.36
1.38	-0.33	110	2.55	47.63	3400	9.42
3.41	-0.54	45	2.86	47.84	2400	9.26
NLS1s						
0.67	-0.93	18	0.06	45.53	2900	7.83
L Composites						
0.43	-0.73	15	0.57	44.73	3100	7.25
0.46	-0.66	90	0.37	45.69	3800	8.10
0.69	-0.36	155	1.39	46.62	4400	8.87
1.15	-0.47	278	2.63	47.52	4900	9.59
1.21	-0.24	20	3.01	48.32	5900	10.30
$M_{\rm SMBH}$ Composites						
0.61	-0.98	7	0.56	44.62	2500	6.78
0.69	-0.90	61	0.46	45.68	3000	7.27
1.08	-0.71	198	1.43	46.84	3800	8.65
0.84	-0.59	261	2.46	47.52	5200	9.54
0.58	-0.57	34	2.84	48.17	7500	10.28
FWHM(C IV) Composites						
3.94	-0.91	14	1.64	47.25	1700	8.35
1.24	-0.48	237	1.71	47.22	3100	8.87
0.58	-0.38	195	1.86	47.48	4900	9.43
0.38	-0.42	91	2.29	47.65	6700	9.84
0.17	-0.47	25	1.89	47.52	9300	10.07

$10^9 - 10^{10}$ $M_\odot$, and $\geq 10^{10}$ $M_\odot$; see also Warner et al. 2003), L ($10^{44} - 10^{45}$ ergs s^{-1}, $10^{45} - 10^{46}$ ergs s^{-1}, $10^{46} - 10^{47}$ ergs s^{-1}, $10^{47} - 10^{48}$ ergs s^{-1}, and $10^{48} - 10^{49}$ ergs s^{-1}), and FWHM(C IV) (< 2000 km s^{-1}, $2000 - 4000$ km s^{-1}, $4000 - 6000$ km s^{-1}, $6000 - 8000$ km s^{-1}, and ≥ 8000 km s^{-1}). See Table 4-1 for additional information.

We also create a composite spectrum of 26 NLS1s that were classified by others according to the criteria described in §4.1 (Kuraszkiewicz et al. 2000; Wang & Lu 2001; Constantin & Shields 2003). This subsample is drawn from the same overall sample used to create the other composites described above. Eighteen of these objects have data at C IV and they span a range in L/L_{edd} from ~ 0.1 to 2.

We correct each composite spectrum for strong iron emission lines using the empirical Fe emission template that was extracted from I Zw 1 by Vestergaard & Wilkes (2001), which they very kindly provided for this study (see Dietrich et al. 2002 and Warner et al. 2003 for more details). The Fe II contribution is generally small at wavelengths $\lesssim 2000$ Å, but the correction for this emission improves the measurements of weak lines such as N III] $\lambda1750$ and He II $\lambda1640$. We fit the continuum of each Fe-subtracted spectrum with a powerlaw of the form $F_\nu \propto \nu^\alpha$. Figure 4-2 shows the final Fe II-subtracted composite spectra normalized by the continuum fits.

To measure the broad emission lines, we use a spectral fitting routine developed in the IDL language, that employs χ^2 minimization. We fit each line with one or more Gaussian profiles, with the goal of simply measuring the total line strengths free of blends. When necessary, we use the profile of strong unblended lines, such as C IV, to constrain the fits to weaker or more blended lines (see Warner et al. 2003 and Appendix B for details of our fitting procedure). Figure 4-3 shows an example of our fits.

The continuum location is the primary uncertainty in our flux measurements. We estimate the 1σ standard deviation of our measurements of the fluxes of Lyα

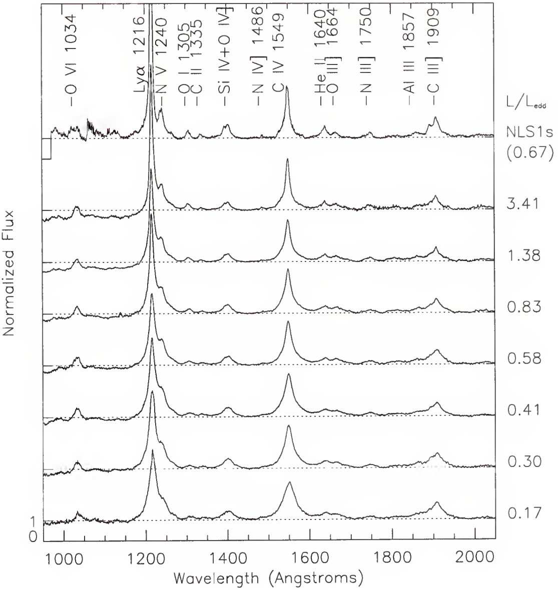

Figure 4–2 Composite spectra, sorted by L/L_{edd}, with the mean L/L_{edd} values indicated at the right. The top spectrum is a composite spectrum created only from objects identified in the literature as NLS1s. The horizontal dashed lines and tick marks indicate the normalized continuum levels for each composite spectrum. The scaled height of the normalized continua above zero flux, as indicated for the bottom spectrum, is the same for all spectra plotted.

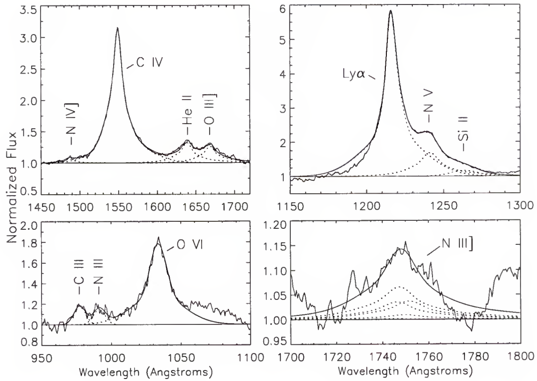

Figure 4–3 Multi-component Gaussian fits (smooth solid curves) to observed emission lines (jagged solid curves) for a composite spectrum of $< L/L_{edd} > \sim 0.58$. The continuum is normalized by a power law continuum fit. The continuum (at unity) and composite line fits are plotted. The individual components of the fits are shown for the fit to N III] as dotted lines. In the other panels, the dotted lines represent the sum contribution of each labelled emission line. There is an unidentified bump at ~1070 Å that is not attributed to O VI (see Hamann et al. 1998).

and C IV to be $\lesssim$10% based on repeated estimates with the continuum drawn at different levels. We estimate the uncertainty in weaker lines by the same method to be ~10–20%. There are also secondary uncertainties due to line blending, which can be important for some of the weak lines and for N V in the wing of Lyα.

4.4 Results and Comparisons

4.4.1 L/L_{edd} and Super-Eddington Accretion

Figure 4-4 shows the distribution of L/L_{edd} for the entire sample. A large fraction (27%) of the objects in our sample have $L/L_{edd} > 1$ (see also Fig. 4-1). This result is not precise because our mass estimates for individual objects have factor of ~3 uncertainties (§4.2), which are comparable to the width of the distribution in Figure 4-4. Nonetheless, it is interesting that the sample mean is close to the Eddington limit, with $< L/L_{edd} > \sim 0.9$ (Fig. 4-4). Also note that trends with L/L_{edd} that we discuss below are more reliable than the individual measurements because they rely on relative L/L_{edd}.

Consistent with previous studies (§4.1), we find that the NLS1s have generally high Eddington ratios for their luminosities, including several objects with $L/L_{edd} \gtrsim 1$. However, the NLS1s do not have the highest Eddington ratios in our sample. Quasars with high luminosities and narrow C IV emission lines often have $L/L_{edd} > 2$. The most extreme of these objects, such as BR2248-1242 (see Warner et al. 2002), can have derived Eddington ratios approaching 10 (see Figure 4-1).

4.4.2 Correlations with L/L_{edd}

Figure 4-5 shows the distributions in redshift, bolometric luminosity, FWHM(C IV), and SMBH mass as a function of L/L_{edd} for the entire sample. L/L_{edd} correlates positively with L and negatively with FWHM(C IV), but these correlations may be attributed largely to our derivation of L/L_{edd} from these quantities. In fact, the slopes in these correlations are matched well by the parameter relationships in Equation (4.4). In agreement with Woo & Urry (2002), we find

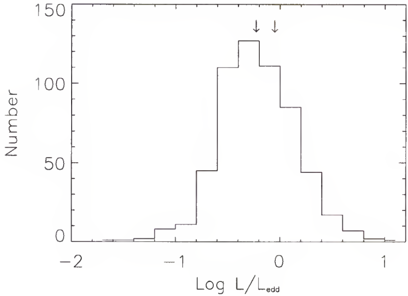

Figure 4–4 Distribution of estimated Eddington ratio, L/L_{edd}. The two arrows are the median (0.59) and mean (0.89) L/L_{edd} of the entire sample. About 27% of the objects have $L/L_{edd} > 1$.

no trend between L/L_{edd} and either redshift or SMBH mass. We find that the weak trend in Figure 4-5 between L/L_{edd} and redshift is due to i) a trend for larger L/L_{edd} with increasing L, and ii) a bias for more high L objects at higher redshifts in our sample. Sub-samples spanning narrow ranges in luminosity show that there is no trend between L/L_{edd} and redshift once these biases are removed (see Figure 4-6). In all four panels of Figure 4-5, there are no clear differences between radio loud and radio quiet objects.

Table 4-1 shows that there is no apparent trend between Eddington ratio and the slope of the UV continuum. The NLS1 composite, though, exhibits a steeper (softer) UV spectrum than the L/L_{edd} composites (see Table 4-1). This is consistent with findings that NLS1s in general have redder spectra than typical Type 1 AGNs (e.g., Crenshaw et al. 2002; Constantin & Shields 2003).

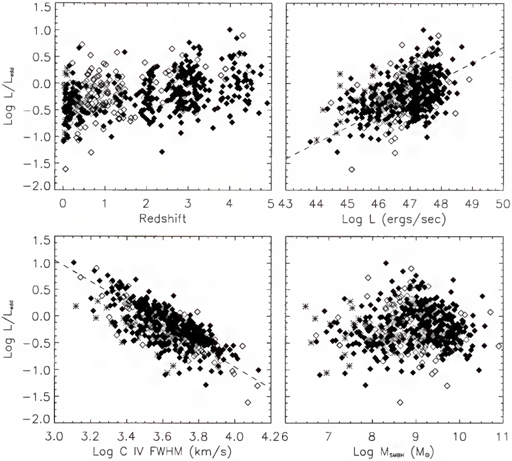

Figure 4–5 Symbols as in Fig. 4-1. The dashed lines represent slopes from the L/L_{edd} equation (not fits). The positive correlation with L and negative correlation with FWHM(C IV) may be attributed largely to our derivation of L/L_{edd} from these quantities (see Equation 4.4).

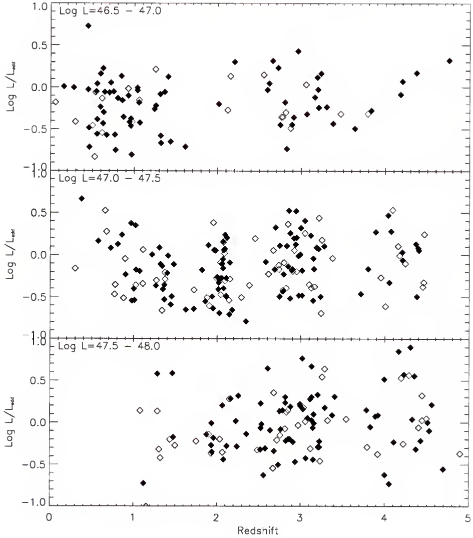

Figure 4–6 Symbols as in Fig. 4-1. In bins of narrow luminosity ranges, there is no apparent trend between L/L_{edd} and redshift. Our sample, though, does seem to have a selection effect for more higher luminosity objects at higher redshifts. This, combined with the trend for higher luminosity objects to have higher L/L_{edd}, explains the slight trend that seems to exist in Fig. 4-5 between L/L_{edd} and redshift.

Table 4-2 lists for each L/L_{edd} and NLS1 composite spectrum the line fluxes relative to Lyα, the rest-frame equivalent widths (REWs) as measured above the fitted continuum, and the FWHMs. Figure 4-7 plots the REWs of selected emission lines as a function of L/L_{edd}. The NLS1 composite spectrum is displayed (plotted as a triangle) for comparative purposes. The dotted lines are linear fits to the L/L_{edd} composite data (excluding the NLS1 composite). Interestingly, while most emission lines decrease in REW with increasing L/L_{edd}, Lyα and O VI exhibit a positive trend between REW and L/L_{edd}, and N III] shows no trend at all. O VI has larger measurement errors than most other emission lines, so it is unclear whether this positive trend between O VI REW and L/L_{edd} is real or not.

The REWs of emission lines in the NLS1 composite (represented by a triangle) generally do not match the trend fit to the L/L_{edd} composites in Figure 4-7. The NLS1 composite is above the fitted trend for some emission lines and below the fitted trend for others, regardless of the slopes of the trends.

4.4.3 Surprising Emission-Line Behaviors

The composite spectra sorted by L/L_{edd} show a surprising emission-line behavior: nearly constant peak heights and decreasing FWHMs with increasing L/L_{edd} (see Figure 4-2). This is in marked contrast to the emission-line behaviors in composite spectra sorted by luminosity, SMBH mass, and FWHM(C IV), which clearly show trends analagous to the Baldwin Effect: decreasing line peaks and equivalent widths with increasing luminosity, SMBH mass, and FWHM. Figure 4-8 compares the emission-line behaviors in these different composites (see also Wills et al. 1993; Croom et al. 2002; Dietrich et al. 2002; Warner et al. 2003). In particular, the composite spectra created from different ranges in FWHM(C IV) clearly show a trend analagous to the Baldwin Effect despite spanning a range of less than half an order of magnitude in average luminosity (Table 4-1). In contrast, the L/L_{edd} composites span a wide range in FWHM(C IV) and an order

Table 4.2. Emission Line Data

L/L_{edd}	Property	O VI λ1034	Lyα λ1216	N V λ1240	C IV λ1549	He II λ1640	O III] λ1665	N III] λ1750	C III] λ1909
0.17	Flux/Lyα	0.21	1.00	0.32	0.75	0.10	0.07	0.06	0.22
	REW[a]	16	80	26	80	12	9	7	32
	FWHM[b]	5500	4700	6900	6800	6800	6800	6900	4900
0.30	Flux/Lyα	0.17	1.00	0.21	0.57	0.08	0.06	0.04	0.13
	REW[a]	16	94	20	74	12	8	6	23
	FWHM[b]	5200	4300	5100	4800	4800	4800	5000	5000
0.41	Flux/Lyα	0.21	1.00	0.23	0.57	0.08	0.06	0.05	0.11
	REW[a]	19	95	22	76	12	9	7	20
	FWHM[b]	6200	4600	5300	4900	4900	4900	5100	4300
0.58	Flux/Lyα	0.28	1.00	0.24	0.57	0.08	0.06	0.05	0.14
	REW[a]	22	83	20	67	10	8	7	23
	FWHM[b]	6500	3800	4300	4000	4000	4000	4200	4900
0.83	Flux/Lyα	0.22	1.000	0.19	0.50	0.07	0.06	0.03	0.12
	REW[a]	20	96	18	65	10	9	5	20
	FWHM[b]	5200	3000	4300	3700	3700	3700	4000	4000
1.38	Flux/Lyα	0.26	1.00	0.21	0.47	0.07	0.05	0.04	0.11
	REW[a]	21	84	18	57	10	7	6	19
	FWHM[b]	5500	2800	3900	3300	3300	3300	3600	3500
3.41	Flux/Lyα	0.21	1.00	0.15	0.41	0.06	0.04	0.04	0.10
	REW[a]	20	100	15	57	9	7	7	19
	FWHM[b]	5100	2100	3000	2500	2500	2500	2800	3100
0.67 (NLS1s)	Flux/Lyα	–	1.00	0.14	0.29	0.06	0.03	0.03	0.13
	REW[a]	–	122	18	45	10	4	5	25
	FWHM[b]	–	2100	2800	2200	2200	2200	2700	3100

[a] In units of Å

[b] In units of km s^{-1}

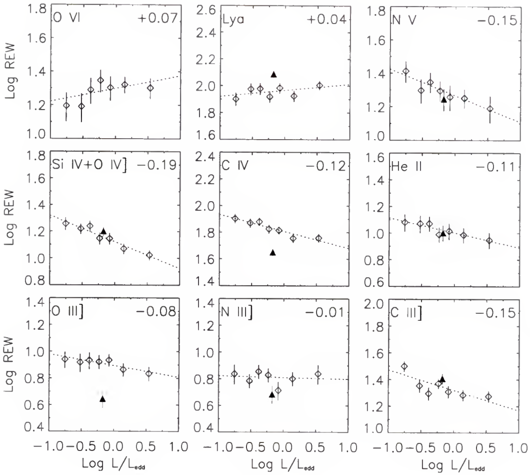

Figure 4–7 The diamonds represent the L/L_{edd} composites and the triangle represents the NLS1 composite. REWs are in angstroms. The dotted lines are linear fits to the L/L_{edd} composites, with slopes given in the upper right. The uncertainties shown are the 1σ standard deviations in the REWs based on repeated estimates with the continuum drawn at different levels (see §4.3).

of magnitude in average luminosity but do not show any behavior similar to the Baldwin Effect. This suggests that the Baldwin Effect may actually be related to SMBH mass (which correlates positively with both L and FWHM), since the L/L_{edd} composites have nearly constant $M_{\rm SMBH}$.

To illustrate this point further, Figure 4-9 compares L/L_{edd} composite spectra created for a narrow range in SMBH mass ($10^8{\rm M}_\odot < M_{\rm SMBH} < 10^9{\rm M}_\odot$) and a narrow luminosity range (10^{47} ergs/s $< L < 10^{48}$ ergs/s). Both sets of spectra are shown prior to normalization to the continuum. The emission line behavior described above (e.g., constant peak heights, etc.) is clearly evident in the L/L_{edd} composites at nearly constant $M_{\rm SMBH}$, but *not* in the composites with nearly constant L. The composites at nearly constant L show a trend for decreasing peak heights and equivalent widths with increasing $M_{\rm SMBH}$.

In composite spectra sorted by luminosity, SMBH mass, and FWHM(C IV), the Baldwin Effect is not seen in N V (see Figure 4-8, also Dietrich et al. 2002; Warner et al. 2003), leading to a higher N V / C IV ratio in objects with higher luminosities, SMBH masses, and FWHMs(C IV). However, in the L/L_{edd} composites created from our entire sample, N V clearly decreases in REW as L/L_{edd} increases, yielding a nearly constant N V / C IV ratio across the full range of L/L_{edd} (see Figure 4-10). Furthermore, the L/L_{edd} composites created from a narrow range in $M_{\rm SMBH}$ exhibit this behavior of nearly constant N V / C IV, while the composites created from a narrow range in L do not (see Fig. 4-9). The composites at nearly constant L show a trend for increasing N V / C IV toward lower L/L_{edd} (higher SMBH masses). The differences in emission-line behaviors at nearly constant $M_{\rm SMBH}$ and at nearly constant L have implications for the origin of the Baldwin Effect (see Warner, Hamann, & Dietrich 2004, in prep). Throughout the rest of this manuscript (including figures and tables), "L/L_{edd} composites" refer to the composite spectra created from our entire sample and sorted by L/L_{edd}.

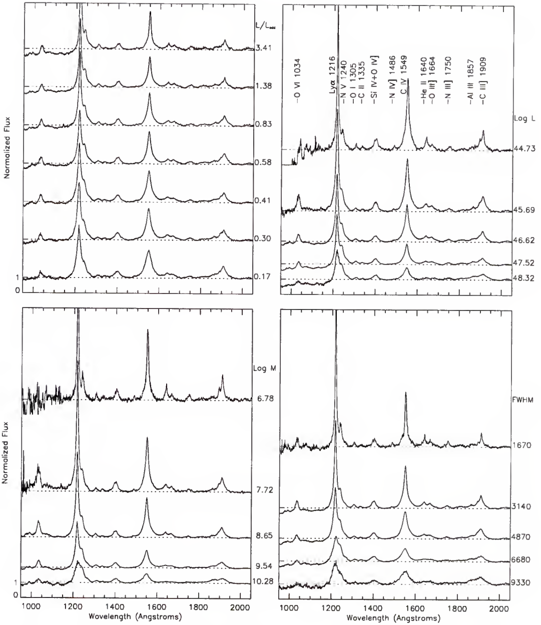

Figure 4–8 Normalized composite spectra sorted by L/L_{edd} (top left, identical to Fig. 4-2 without the NLS1 composite) are compared to normalized composite spectra computed from different ranges in bolometric luminosity (top right, in units of ergs/sec), SMBH mass (bottom left, in $M_{\odot}$), and FWHM(C IV) (bottom right, in km/sec). Dashed lines and tick marks as in Fig. 4-2. The L, SMBH mass, and FWHM composite spectra all clearly show trends for decreasing line equivalent widths and peak heights as luminosity, SMBH mass, and FWHM(C IV) increase. The composite spectra sorted by FWHM(C IV) even exhibit this trend despite spanning less than half an order of magnitude in average luminosity, a much narrower range than in the L/L_{edd} composites (see Table 4-1). However, the L/L_{edd} composites show nearly constant peak heights and decreasing FWHMs with increasing L/L_{edd}.

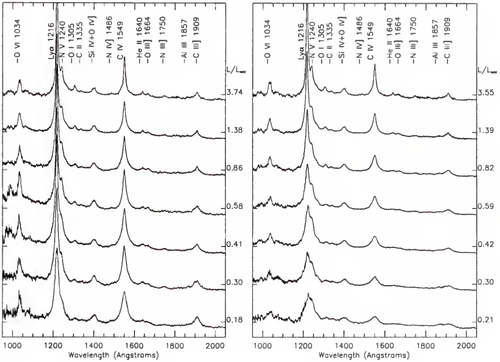

Figure 4–9 Composite spectra sorted by L/L_{edd} for a narrow range in SMBH mass of $10^8 M_\odot < M_{\rm SMBH} < 10^9 M_\odot$ (left) are compared to ones sorted by L/L_{edd} for narrow range in luminosity of 10^{47} ergs/s $< L < 10^{48}$ ergs/s (right). The spectra are shown prior to normalization to the continuum. The composite spectra at nearly constant $M_{\rm SMBH}$ show the same emission-line behavior as the L/L_{edd} composites created from our entire sample: nearly constant peak heights and decreasing FWHMs with increasing L/L_{edd}. In contrast, the composite spectra at nearly constant L do not share this behavior and show a trend similar to the Baldwin Effect: decreasing peak heights and equivalent widths with increasing $M_{\rm SMBH}$.

4.4.4 Metallicities

We compare emission line flux ratios to plots of metallicity vs. line ratio based on theoretical models (see Figure 5 in Hamann et al. 2002 and Figure 3 in Warner et al. 2002). Ratios involving nitrogen lines are especially valuable in estimating metallicity, Z, due to the expected "secondary" N production via the CNO cycle of nucleosynthesis in stars (Shields 1976; Hamann & Ferland 1992, 1993, 1999; Ferland et al. 1996; Hamann et al. 2002). In the CNO cycle, N is produced from existing carbon and oxygen and thus the nitrogen abundance scales as $\mathrm{N/H} \propto Z^2$ and $\mathrm{N/O} \propto \mathrm{O/H} = Z$ (Tinsley 1980), providing a sensitive metallicity diagnostic even when direct measurements of Z are not available (for more discussion, see Wheeler et al. 1989; Hamann & Ferland 1999; Henry et al. 2000; Hamann et al. 2003; Pilyugin 2003; Pilyugin et al. 2003). We prefer to base our metallicity estimates on the calculations in Hamann et al. (2002) that use a segmented powerlaw for the photoionizing continuum shape because this shape is a good approximation to the average observed continuum in quasars (Zheng et al. 1997; Laor et al. 1997) and it yields intermediate results for line ratios that are sensitive to the continuum shape, such as N V/He II.

Figure 4-10 shows metallicities inferred from several line ratios as a function of L/L_{edd}. The uncertainties shown in Figure 4-10 derive solely from the 1σ measurement uncertainties discussed in §4.3 and do not include the theoretical uncertainties in the technique we use to derive metallicities from the line ratios. Our best estimate of the overall metallicity from each spectrum (labeled as Average in Figure 4-10) is obtained by averaging the results of the line ratios that we believe are most accurately measured and most reliable from a theoretical viewpoint. Specifically, we average the metallicities derived from N III]/C III], N III]/O III], and N V/C IV (or when available, N V/(C IV+O VI)). See Hamann et al. (2002) and Warner et al. (2003) for further discussion.

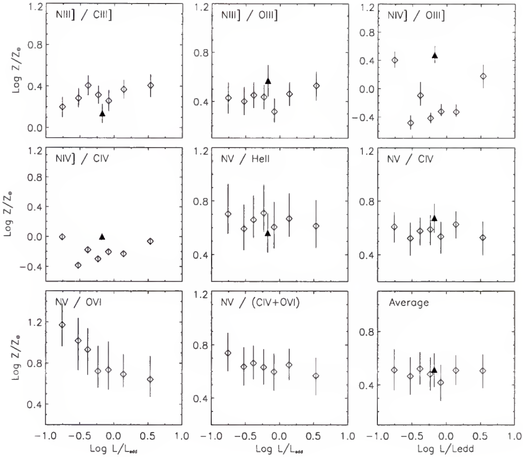

Figure 4–10 Metallicities derived from comparisons of different line ratio diagnostics to theoretical results from Figure 5 in Hamann et al. (2002) are shown as a function of L/L_{edd}. The average includes N III]/C III], N III]/O III], and N V/(C IV+O VI). Symbols as in Fig. 4-7.

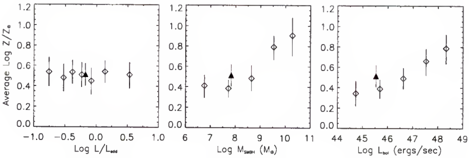

Figure 4–11 Symbols as in Fig. 4-7. Our best estimates of the overall metallicity of each spectrum are shown for the L/L_{edd}, SMBH mass, and luminosity composite spectra. The NLS1 composite, plotted in all three panels as a filled triangle, has a metallicity that is slightly high for its SMBH mass and luminosity, but still well below the metallicities of most luminous quasars.

All of the line ratios involving N III] and N V show N/O and N/C ratios that are solar or greater. This implies a metallicity of $\gtrsim 1$ $Z_\odot$ if N is mostly secondary. One implication of the unusual emission-line behavior with L/L_{edd} (discussed in §4.4.3) is that the derived metallicities on average show no trend with L/L_{edd}. The only line ratio to exhibit a strong trend with L/L_{edd} is N V/O VI.

Figure 4-11 shows our best estimates of the overall metallicities (derived from several line ratios, as described above for the "Average" in Figure 4-10) from the composite spectra sorted by L/L_{edd}, SMBH mass, and luminosity. The NLS1 composite spectrum is plotted in all three panels for comparison. The NLS1s exhibit a metallicity that is slightly high (a 30%–40% enhancement) for their SMBH masses and luminosities (see also Shemmer & Netzer 2002; Shemmer et al. 2003), but still well below the metallicities derived for most luminous quasars.

It is difficult to compare our results directly to Shemmer & Netzer (2002) because they measure only N V/C IV and N V/He II ratios for a sample of individual objects. However, it does appear that the metallicity enhancement we derive as an average from several line ratios is smaller than the Shemmer & Netzer result based only on N V/C IV and N V/He II.

4.5 Discussion

There is evidence supporting super-Eddington accretion rates for ~27% of the objects shown in Figures 4-1 and 4-4. Previous studies have also found quasars that appear to be accreting at super-Eddington rates (e.g., Collin et al. 2002, Vestergaard 2004). It is also worth noting that changing the index on the $R_{BLR} - L$ relationship (see §4.1) from 0.7 to 0.5 (e.g., Netzer & Laor 1993; Shields et al. 2003) would actually increase our estimates of L/L_{edd}, by as much as a factor of $\sim$ 4 in the brightest quasars (see also Netzer 2003). Super-Eddington accretion can be explained simply by non-spherically symmetric accretion (Osterbrock 1989). It has been suggested that accretion disks with radiation-driven inhomogeneities could produce luminosities up to 100 times Eddington (Begelman 2002; Wang 2003).

Woo & Urry (2002) find that only 9% of their objects (21 out of 234, see their Fig. 4-7) have $L/L_{edd} > 1$. However, this may be due to the selection effect that their sample contains only 9 objects with $L > 10^{47}$ ergs s^{-1}. In our sample, only 13% of the objects with $L \leq 10^{47}$ ergs s^{-1} have $L/L_{edd} > 1$ (compared to 8%, 18 out of 225, in Woo & Urry 2002), but 41% of the objects in our sample with $L > 10^{47}$ ergs s^{-1} have super-Eddington ratios.

The NLS1 composite spectrum exhibits many properties unlike the L/L_{edd} composite spectra. The NLS1 composite has a much steeper ("softer") UV continuum than the L/L_{edd} composites, consistent with studies finding that NLS1s generally have redder UV continua than typical AGNs (e.g., Crenshaw et al. 2002; Constantin & Shields 2003). There is no apparent trend between continuum shape and L/L_{edd} (Table 4-1), but there are trends between continuum shape and both SMBH mass (see Table 4-1; Warner et al. 2003) and luminosity (Table 4-1; M. Dietrich, private comm.), such that objects with lower SMBH masses and lower luminosities have steeper ("softer") UV continua. Therefore, the steeper UV continuum in the NLS1 composite may be due to the NLS1 composite having a much lower average $M_{\rm SMBH}$ and L than the L/L_{edd} composites.

Interestingly, Figure 4-2 shows that the NLS1 composite spectrum most strongly resembles the composite spectrum created from objects with $L/L_{edd} > 2$. It seems to fit at the top of Figure 4-2 and not where it would be placed based on its average L/L_{edd} of 0.67. Based on this similarity between NLS1s and quasars with high L/L_{edd}, it has been suggested that high-redshift ($z \gtrsim 4$), high-luminosity, narrow-lined quasars are analogs of NLS1s (Mathur 2000). However, despite the similarity in Figure 4-2 between the NLS1 composite and the $L/L_{edd} > 2$ composite, the REWs of some emission lines in the two spectra can be quite different (see Figure 4-7, Constantin & Shields 2002). Moreover, the NLS1s do not fit the general trends in Figure 4-7 between emission line REW and L/L_{edd}.

If host galaxy mass, which correlates strongly with SMBH mass (see §4.1), is the fundamental parameter affecting BLR metallicity, it is reasonable to expect no trend between metallicity and L/L_{edd} because there is no trend between L/L_{edd} and SMBH mass in the L/L_{edd} composites. The results in Figures 4-10 and 4-11 confirm this expectation. The different L/L_{edd} composites have similar average SMBH masses (Table 4-1) and similar metallicities. However, the NLS1 behavior is surprising. They have roughly the same metallicity as the L/L_{edd} composites even though their average SMBH mass and luminosity are almost two orders of magnitude lower. Figure 4-11 shows more directly that the NLS1s have slightly high metallicities for their luminosities and SMBH masses (see also Shemmer & Netzer 2002; Shemmer et al. 2003). If host galaxy mass, correlated with $M_{\rm SMBH}$, is the main driver behind AGN metallicities (Figure 4-11 and Warner et al. 2003), then clearly some other factor is enhancing the metallicities in NLS1s. The magnitude of the NLS1 enhancement is modest, roughly 30%–40%. Note, in particular, that the NLS1 metallicities are still well below the values derived for most luminous (e.g., high-redshift) quasars.

Shemmer & Netzer (2002) suggest that high L/L_{edd} is driving the high metallicities in NLS1s. However, we have shown that there is no correlation between metallicity and L/L_{edd} (Figures 4-10 and 4-11). In addition, luminous narrow-lined quasars with the highest values of L/L_{edd} (such as BR2248-1242, Warner et al. 2002) do *not* have high metallicities for their SMBH masses. We conclude that the additional parameter affecting NLS1 metallicities is not related to L/L_{edd}.

Constantin & Shields (2003) suggest that the result for NLS1s having lower metallicities than high-redshift quasars runs counter to the hypothesis that these two groups of objects are in a similar early evolutionary phase. However, because the high-redshift quasars have higher SMBH masses and luminosities than NLS1s, they would naturally be expected to have higher metallicities. If both types of objects are in similar early evolutionary phases, and/or reside in young or rejuvenated host galaxies and the metallicities of both types of objects are thus enhanced by a similar amount, then the high-redshift quasars would still exhibit a higher metallicity than the NLS1s due to their higher SMBH masses. Thus, we conclude that more information is necessary to determine if either NLS1s or the high-redshift quasars (or both) are preferentially young objects.

4.6 Summary and Conclusions

We have examined a large sample of 578 AGNs that spans five orders of magnitude in SMBH mass, seven orders of magnitude in luminosity, and a redshift range from $0 \leq z \leq 5$. We estimate SMBH masses using the virial theorem and formulae given in Kaspi et al. (2000), and then derive Eddington ratios. To improve the signal-to-noise ratio and average over object-to-object variations, we calculate composite spectra for different ranges in L/L_{edd}. We include a composite spectrum of a sample of 26 NLS1s for comparative analysis. Our main results are as follows.

1) We find that a large fraction (27%) of the objects in our sample have $L/L_{edd} > 1$. These super-Eddington ratios may be explained by non-spherically symmetric accretion. While NLS1s generally show high Eddington ratios for their luminosities, the objects with the highest L/L_{edd} are high-luminosity, narrow-lined quasars.

2) There is no trend between L/L_{edd} and either redshift or SMBH mass. L/L_{edd} does correlate positively with luminosity and negatively with FWHM(C IV), but these trends may be attributed largely to our derivation of L/L_{edd} from these quantities (see Equation 4.4).

3) There is no trend between the shape of the UV continuum and L/L_{edd}. The NLS1 composite has a much steeper (softer) continuum than the L/L_{edd} composites. This is consistent with a trend between continuum shape and SMBH mass.

4) The composite spectra sorted by L/L_{edd} exhibit an unusual emission-line behavior: nearly constant peak heights and decreasing FWHMs with increasing L/L_{edd} (Figure 4-2). The origins of this behavior are not understood, but it is in marked contrast to the emission-line behaviors in composite spectra sorted by luminosity, SMBH mass, and FWHM(C IV) (Figure 4-8), all of which clearly show trends in the line REWs analagous to the Baldwin Effect.

5) The composite spectra show no trend between L/L_{edd} and metallicity (Figure 4-10). This is consistent with SMBH mass being related to the fundamental parameter affecting BLR metallicity (Warner et al. 2003).

6) The NLS1 composite exhibits several unusual behaviors. It generally does not fit the trends between emission line REWs and L/L_{edd} as defined by the L/L_{edd} composites. It also has a metallicity that is slightly high for its average SMBH

mass and luminosity, although still well below the high metallicities exhibited by the most luminous quasars with the most massive central SMBHs. The quasars with the highest L/L_{edd}, high-luminosity quasars with narrow C IV emission, do not have high metallicities for their SMBH masses and luminosities. Our earlier work (Warner et al. 2003) is consistent with the theory that host galaxy mass, correlated with SMBH mass (and AGN luminosity), is the fundamental parameter affecting BLR metallicity. We conclude that i) there must be some secondary effect enhancing the metallicity in NLS1s, and ii) this secondary effect is not related to L/L_{edd}.

CHAPTER 5
BLACK HOLE MASSES, METALLICITIES, AND THE BALDWIN EFFECT

5.1 Introduction

Supermassive black holes (SMBHs) are believed to power the central engines of Active Galactic Nuclei (AGNs). Recent studies have shown that the mass of the SMBH scales directly with the mass of the host galaxy's bulge or spheroidal component (Magorrian et al. 1998; Laor et al. 1998; Wandel 1999; Ferrarese & Merritt 2000, 2002; Gebhardt et al. 2000a; Tremaine et al. 2002). The SMBH masses have been estimated by several indirect methods. One set of these methods assumes that the broad emission-line region (BLR) is in gravitational equilibrium with the central SMBH, and thus the black hole's mass can be estimated by applying the virial theorem, $M_{\rm SMBH} = rv^2/G$, to the line-emitting gas (Peterson 1993; Peterson 1997; Wandel et al. 1999; Kaspi et al. 2000; McLure & Dunlop 2001; Vestergaard 2002). Reverberation mapping studies have used the lag time between continuum variations and the emission-line response to estimate $R_{\rm BLR}$, the radial distance between the central SMBH and the BLR (Peterson 1993; Peterson 1997; Wandel et al. 1999; Kaspi et al. 2000). These studies have also demonstrated an observed relation of approximately $R_{\rm BLR} \propto \lambda L_\lambda(5100\text{Å})^{0.7}$ that can be used to estimate $R_{\rm BLR}$, and thus $M_{\rm SMBH}$, across a wide range of redshifts (Kaspi et al. 2000; McLure & Dunlop 2001; Vestergaard 2002; Corbett et al. 2003; Warner et al. 2003). Netzer (2003) has argued that the powerlaw index in this relation is not known to an accuracy of better than about 0.15. However, a precise knowledge of this powerlaw slope is not needed for our analysis based on global trends in a large dataset.

The overall mass of a galaxy's bulge or spheroidal component is also known to correlate with its metallicity (Faber 1973; Zaritsky et al. 1994; Jablonka et al. 1996; Trager et al. 2000). This relationship is attributed to more massive galaxies having deeper potential wells, making it harder for supernovae and stellar winds to expel matter from the region. Thus, the gas remains in the galaxy longer and is further reprocessed by stars, resulting in higher metallicities.

Broad emission line flux ratios involving nitrogen lines can be valuable in estimating the metallicity, Z, in AGNs. This is due to the expected "secondary" N production via the CNO cycle of nucleosynthesis in stars, in which N is produced from existing carbon and oxygen (Shields 1976; Hamann & Ferland 1992, 1993, 1999; Ferland et al. 1996; Hamann et al. 2002). Therefore, the nitrogen abundance scales as $\mathrm{N/H} \propto Z^2$ and $\mathrm{N/O} \propto \mathrm{O/H} = Z$ (Tinsley 1980), providing a metallicity diagnostic (for $Z \gtrsim 0.2\ \mathrm{Z}_\odot$) when direct measurements of $Z = \mathrm{O/H}$ are not available (see also Wheeler et al. 1989; Hamann & Ferland 1999; Henry et al. 2000; Hamann et al. 2003; Pilyugin 2003; Pilyugin et al. 2003).

Warner et al. (2003) found a relationship between SMBH mass and BLR metallicity that can be understood by combining the galaxy mass-metallicity relationship with the relationship between SMBH mass and galaxy mass. Furthermore, we found that the slope of the M_{SMBH}-BLR metallicity relationship is consistent with the slope of the observed galactic mass-metallicity relation. However, we could not rule out AGN luminosity as the fundamental parameter driving BLR metallicity because of the tight correlation between SMBH mass and luminosity in our sample (see Figure 7 in Warner et al. 2003). In this paper, we revisit the M_{SMBH}-BLR metallicity relationship and isolate SMBH mass and AGN luminosity by creating composite spectra that i) span a range in SMBH mass at nearly constant luminosity and ii) span a range in luminosity at nearly constant SMBH mass.

We also discuss the Baldwin Effect, an observed inverse correlation between AGN luminosity and the equivalent widths of strong emission lines such as Lyα, C IV λ1549, and O VI λ1034 (Baldwin 1977; Espey et al. 1993; Wills et al. 1993; Zheng & Malkan 1993; Osmer et al. 1994; Osmer & Shields 1999; Croom et al. 2002; Dietrich et al. 2002). We examine the relationships between SMBH mass, luminosity, and general emission line properties.

5.2 Data and Analysis

Our sample consists of over 800 Type 1 (broad-line) AGNs, 578 of which have rest-frame UV spectra covering the range $950 \leq \lambda \leq 2050$ Å. The spectra were obtained by several groups using various ground-based instruments as well as the *Hubble Space Telescope (HST)* and the *International Ultraviolet Explorer (IUE)* (see Dietrich et al. 2002, 2004 in prep; Warner et al. 2004 for more details). The sample spans seven orders of magnitude in luminosity, five orders of magnitude in SMBH mass, and a redshift range of $0 \lesssim z \lesssim 5$. One unique property of this sample is that it contains new observations of faint quasars at redshift $z > 2.5$ (e.g., Steidel et al. 2002, Dietrich et al. 2002). At all redshifts, the sample spans at least three orders of magnitude in luminosity (see Fig. 1 in Dietrich et al. 2002). Therefore, we can avoid to some degree the bias toward higher luminosities at higher redshifts inherent in magnitude-limited samples.

We estimate SMBH masses by application of the virial theorem (see Warner et al. 2003):

$$M_{SMBH} = 1.5 \times 10^5 \mathrm{M}_\odot \left(\frac{R_{\mathrm{BLR}}}{\mathrm{lt-days}}\right) \left(\frac{\mathrm{FWHM}}{10^3\ \mathrm{km\ s^{-1}}}\right)^2 \tag{5.1}$$

where FWHM applies to the broad emission line profile. We estimate R_{BLR} based on the observed relation between R_{BLR} for a particular line and the continuum luminosity (Wandel et al. 1999; Kaspi et al. 2000; Vestergaard et al. 2002; Corbett et al. 2003). We select the C IV λ1549 emission line instead of Hβ to estimate SMBH masses because it is more readily observable across the entire redshift range from $z \sim 0$ to $z \sim 5$. Warner et al. (2003) showed there is approximately a 1:1 correlation between the SMBH mass obtained from C IV and that obtained from Hβ, after adjusting for a factor of ~ 2 smaller value of $R_{\rm BLR}$ for C IV. Individual objects can show significant deviations from this correlation, but it holds well for averages of many objects and composite spectra (see also Vestergaard 2002). We derive

$$M_{SMBH} = 1.4 \times 10^{6} {\rm M}_{\odot} \left(\frac{\rm FWHM(CIV)}{10^{3}\ {\rm km\ s^{-1}}}\right)^{2} \left(\frac{\lambda L_{\lambda}(1450{\rm \AA})}{10^{44}\ {\rm ergs\ s^{-1}}}\right)^{0.7} \tag{5.2}$$

SMBH masses estimated by applying this equation to single-epoch spectra of individual objects have a 1σ uncertainty of a factor of three when compared to studies that use Hβ and a direct reverberation measurement of $R_{\rm BLR}$ (Vestergaard 2002). Composite spectra and averages over large samples should have significantly lower uncertainties because they average over variabilities and object-to-object scatter. See Krolik (2001), Vestergaard (2002, 2004), Netzer (2003), and Corbett et al. (2003) for further discussion of the uncertainties.

We measure the FWHM of C IV in each spectrum using an automated program (see Warner et al. 2003 for details). Comparisons between the FWHMs derived by this program and those measured manually indicate an error of $\leq 10\%$ in the automated results. Lines containing significant absorption are flagged by the program and their FWHMs are estimated by manually interpolating across the absorption feature. We use the FWHM(C IV) and the continuum luminosity, $\lambda L_{\lambda}(1450{\rm \AA})$, to estimate SMBH masses for all objects in our sample based on Equation (5.2).

We then estimate bolometric luminosities, L, based on an integration over a typical quasar continuum shape (see Warner et al. 2004 for details). We derive bolometric corrections of 4.36 and 9.27 for $\lambda L_{\lambda}(1450{\rm \AA})$ and $\lambda L_{\lambda}(5100{\rm \AA})$, respectively. These corrections are in good agreement with other recent derivations (Kaspi et al. 2000; Vestergaard 2004). We use the cosmological parameters $\rm H_0 = 65$

km s^{-1} Mpc^{-1}, $\Omega_M = 0.3$, and $\Omega_\Lambda = 0$ (Carroll, Press, & Turner 1992) throughout this paper[1] .

5.3 Composite Spectra

In order to isolate SMBH mass and luminosity, we first select narrow ranges of $8.9 < \log M_{\rm SMBH} < 9.3$ $M_\odot$, $46.5 < \log L < 47.5$ ergs s^{-1}, and $47.0 < \log L < 47.5$ ergs s^{-1}. These ranges were selected to obtain a large number of objects in small ranges of $M_{\rm SMBH}$ and L. We then sort the quasars in these ranges by $M_{\rm SMBH}$ or L into several bins and compute composite (average) spectra for each bin. Therefore, we obtain composite spectra that i) span a range in luminosity at nearly constant SMBH mass and ii) span a range in SMBH mass at nearly constant luminosity. For comparison, we also create composite spectra that span a range in SMBH mass from a narrow range of $3000 <$ FWHM(C IV) < 4000 km s^{-1} (see §5.4). Table 5-1 lists various parameters for the composite spectra, including the mean values of $M_{\rm SMBH}$, L, FWHM(C IV), Eddington ratio, L/L_{edd}, and the redshift, z, as determined from the individual objects contributing to each composite. Also listed are the number of objects contributing to each composite at the wavelength of the C IV emission line. The spectral slopes, α, are defined below. Notice that the average SMBH mass in the $8.9 < \log M_{\rm SMBH} < 9.3$ $M_\odot$ composites is the same to within 25%, while the average L varies by a factor of 8. In the composites with $47.0 < \log L < 47.5$ ergs s^{-1} and $46.5 < \log L < 47.5$ ergs s^{-1}, the average luminosities are the same to within 32% and a factor of 2.7, respectively, while the SMBH masses span a factor of 8 and 18, respectively.

---

[1] The use of this cosmology was motivated for comparison with earlier studies in the pre-WMAP era. The difference between this set of cosmological parameters and those suggested by WMAP results in a difference of less than 20% in luminosity for a wide redshift range of $0 < z < 4$ (Dietrich et al. 2004, in prep).

Table 5–1 Composite Parameters

# Objects at C IV	α	z	Log L [ergs s^{-1}]	FWHM(C IV) [km s^{-1}]	Log M_{SMBH} [M$_\odot$]	L/L_{edd}
$8.9 \leq \log M_{\mathrm{SMBH}} < 9.3$ M$_\odot$						
30	-0.09	1.44	46.65	5800	9.07	0.32
49	-0.39	2.17	47.10	4400	9.15	0.75
40	-0.40	2.81	47.56	3200	9.17	2.07
$46.5 \leq \log L < 47.5$ ergs s^{-1}						
25	-0.46	2.03	46.86	2600	8.47	2.11
90	-0.60	2.06	47.03	3600	8.89	1.14
108	-0.55	2.18	47.20	5300	9.35	0.61
29	-0.58	2.26	47.29	7400	9.72	0.30
$47.0 \leq \log L < 47.5$ ergs s^{-1}						
33	-0.62	2.46	47.19	2700	8.80	2.25
84	-0.61	2.37	47.26	4500	9.29	0.82
43	-0.55	2.34	47.31	6900	9.69	0.35
$3000 \leq$ FWHM(C IV) < 4000 km s^{-1}						
22	-0.70	0.25	45.51	3400	7.80	0.38
74	-0.64	1.23	46.69	3500	8.61	0.79
51	-0.37	2.86	47.61	3500	9.31	1.50

One advantage of composite spectra is that they improve the signal-to-noise ratio, making it easier to measure weaker emission lines that may be lost in the noise in individual spectra. Since narrow absorption features may affect the emission line profiles in composite spectra, we developed a routine to detect strong narrow absorption features. The contaminated spectral region of the individual spectrum is then excluded from the calculation of the composite spectrum. For more details about creating composite spectra, see Brotherton et al. (2001), Vanden Berk et al. (2001), Dietrich et al. (2002), and Warner et al. (2003).

We correct each composite spectrum for strong iron emission lines using the empirical Fe emission template that was extracted from I Zw 1 by Vestergaard & Wilkes (2001), which they very kindly provided for this study (see Dietrich et al. 2002 and Warner et al. 2003 for more details). This correction, while generally small at wavelengths $\lesssim$ 2000 Å, significantly improves the measurements of weak lines such as O III] λ1665 and N III] λ1750. We then fit the continuum of each spectrum with a powerlaw of the form $F_\nu \propto \nu^\alpha$. The fit is constrained by the flux in 20 Å wide intervals centered at 1450 Å and 1990 Å. Figure 5-1 shows the final Fe-subtracted composite spectra normalized by the continuum fits.

We use a spectral fitting routine developed in the IDL language, that employs χ^2 minimization, to measure the composite broad emission lines. We fit each line with one or more Gaussian profiles with the goal of simply measuring the total line strengths free of blends. We use the profile of C IV to constrain the fits to weaker or more blended lines such as N III] λ1750 and N V λ1240. See Warner et al. (2003) for more details of our fitting procedure. The continuum location is the primary uncertainty in our flux measurements. We estimate the 1σ standard deviation of our measurements of the fluxes of Lyα and C IV to be $\lesssim$10% based on repeated estimates with the continuum drawn at different levels. We estimate the uncertainty in the fluxes of weaker lines to be ~10–20% by the same method.

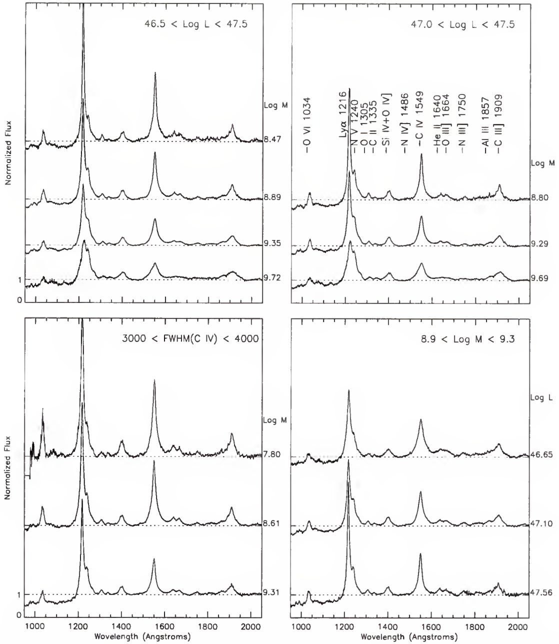

Figure 5–1 Normalized composite spectra sorted by SMBH mass in narrow ranges of luminosity (top left and right) and FWHM(C IV) (bottom left) are compared to normalized composite spectra sorted by luminosity in a narrow range of SMBH mass (bottom right). The mean values of SMBH mass ($M_\odot$) and luminosity (ergs s^{-1}) are indicated to the right. The horizontal dashed lines and tick marks indicate the normalized continuum levels for each composite spectrum. The scaled height of the normalized continua above zero flux, as indicated for the bottom spectrum in each panel, is the same for all spectra plotted. The composite spectra sorted by SMBH mass all show a trend for decreasing line equivalent widths and peak heights as SMBH mass increases. However, the composites sorted by luminosity at nearly constant SMBH mass show nearly constant C IV peak heights and increasing Lyα peak heights with increasing luminosity.

This does not include additional uncertainties due to line blending, which can be important for some of the weaker lines and for N V in the wing of Lyα.

5.4 Results and Comparisons

5.4.1 Metallicities

We estimate metallicities by comparing the measured line ratios to plots of metallicity vs. line ratio based on theoretical models (see Figure 5 in Hamann et al. 2002 and Figure 3 in Warner et al. 2002). All of the line ratios involving N III] or N V indicate N/O and N/C ratios that are solar or higher. This implies solar or higher metallicities if N is mostly secondary (§5.1).

Figure 5-2 shows trends in some of the line flux ratios measured from the composites. These particular ratios were favored by Hamann et al. (2002) for metallicity estimates because they are most accurately measured and most reliable from a theoretical viewpoint. All of the ratios exhibit a strong trend with SMBH mass in the composite spectra created from narrow ranges in both luminosity and FWHM(C IV). However, the composite spectra created from nearly constant SMBH mass show no trend between the line ratios and luminosity. It therefore appears that SMBH mass is the fundamental driver behind AGN metallicities.

To test this idea further, we also examine the line ratio behaviors with changing FWHM(C IV) and accretion efficiency, $L/L_{edd} \propto \dot{M}_{acc}/M_{\rm SMBH}$, where $\dot{M}_{acc}$ is the mass accretion rate. Notice that the composites created at fixed L (top two panels in Fig. 5-1) have FWHM(C IV) increasing with SMBH mass because of the method used to derive the masses (Eqn. 5.2). Could it be that the line ratios (i.e., metallicity) depend more on FWHM(C IV) than SMBH mass? The lower left panel of Figure 5-1 shows composites spanning a range in SMBH mass at roughly constant FWHM(C IV). Specifically, the average FWHMs(C IV) in these composites are the same to within 3%, while the SMBH masses span a factor of 32. Inspection of this plot shows that the line ratios diagnostic of metallicity (e.g., N V/C IV,

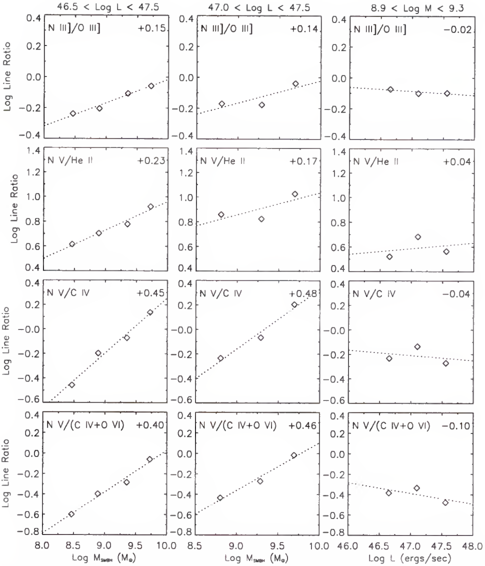

Figure 5–2 Emission line ratios diagnostic of metallicity are plotted versus SMBH mass and luminosity for three of the composite spectra shown in Fig. 5-1. The dotted lines are linear fits to the data, with slopes given in the upper right. All of the ratios indicate a strong trend between metallicity and SMBH mass, but no trend between metallicity and luminosity.

N V/He II, and N III]/O III]) increase dramatically with SMBH mass even at a fixed FWHM(C IV). However, the converse does not occur; composite spectra that span a range in FWHM(C IV) at constant SMBH mass[2] show no dependence of the line ratios on FWHM(C IV).

Similar experiments comparing L/L_{edd} to SMBH mass lead to the same result. In particular, if we fix SMBH mass and consider a range in L/L_{edd}, we find no change in the line ratios with changing L/L_{edd} (see Fig. 9 in Warner et al. 2004). But if we fix L/L_{edd} and allow SMBH mass to vary, we again see a strong trend for increasing nitrogen line ratios with increasing mass (data not shown). Our analysis in Warner et al. (2004) showed that overall the line flux ratios have virtually no dependence on L/L_{edd} (if SMBH mass is fixed). SMBH mass is clearly the main driver behind these line ratios.

However, Warner et al. (2004) also noted a surprising exception in the Narrow Line Seyfert 1s (NLS1s, as defined by Hβ FWHM and other criteria). These objects tend to have larger nitrogen ratios, and thus higher metallicities, for a given SMBH mass, compared to the rest of our Type 1 AGN sample (see also Shemmer & Netzer 2002). NLS1s also have larger L/L_{edd} ratios for a given SMBH mass, and so it has been suggested that enhanced accretion efficiency correlates with enhanced metallicities (Shemmer & Netzer 2002; Shemmer et al. 2004). However, Warner et al. (2004) showed that there is no relationship between metallicity (i.e., the nitrogen line ratios) and L/L_{edd} if SMBH mass is held fixed. Some unknown parameter, which is not L, L/L_{edd}, FWHM(C IV), nor SMBH mass, conspires to make the nitrogen line ratios larger in NLS1s (see Warner et al. 2004 and §5.5.1 below for more discussion).

---

[2] The composite spectra that span a range in luminosity at nearly constant SMBH mass also span a wide range in FWHM(C IV) (see Figure 5-1 and Table 5-1). These spectra, therefore, illustrate the effects of changing FWHM(C IV) at constant SMBH mass.

5.4.2 Line Peak Heights and the Baldwin Effect

Warner et al. (2004) found another interesting emission line behavior: composite spectra that have nearly the same average SMBH mass will also have nearly the same line peak heights (relative to the continuum) for any value of L/L_{edd}. However, composites that span a factor of 100 in average SMBH mass at constant L/L_{edd} (within 3%) show a dramatic trend for decreasing line peak heights with increasing SMBH mass.

Our composite spectra that isolate $M_{\rm SMBH}$ and L exhibit this same behavior (see Figure 5-1). The composite spectra sorted by SMBH mass in narrow ranges of both luminosity and FWHM(C IV) show decreasing line peak heights and equivalent widths with increasing SMBH mass. However, the composite spectra sorted by luminosity or FWHM(C IV) in a narrow range of SMBH mass have nearly constant C IV peak heights (and actually *increasing* Lyα peaks) with increasing luminosity.

This behavior of the peak heights is analogous to the Baldwin Effect, except we have shown that it is tied to SMBH mass and not the AGN luminosity. To examine the Baldwin Effect directly, we now explore the dependence of the line rest equivalent widths (REWs) on L and $M_{\rm SMBH}$. Typically, a strong Baldwin Effect is exhibited by the emission lines O VI λ1034, Lyα, and C IV (Baldwin 1977; Croom et al. 2002; Dietrich et al. 2002; Espey et al. 1993; Osmer et al. 1994; Osmer & Shields 1999; Zheng & Malkan 1993). Figure 5-3 shows that in the composite spectra sorted by SMBH mass in a narrow luminosity range these three emission lines do show a strong inverse correlation between REW and SMBH mass. In the composite spectra sorted by luminosity at nearly constant SMBH mass, the REW of C IV does inversely correlate with luminosity (although with a slope that is less steep than in the SMBH mass composites), but the REWs of O VI and Lyα actually increase with increasing luminosity.

The Baldwin Effect is not usually present in N V λ1240 (Osmer et al. 1994; Laor et al. 1995; Turnshek 1997; Korista et al. 1998; Espey & Andreadis 1999; Dietrich et al. 2002; Warner et al. 2003), leading to a higher N V / C IV ratio in objects with higher luminosities, SMBH masses, and FWHMs(C IV). In our composite spectra sorted by SMBH mass, the REW of N V actually increases with SMBH mass, again leading to a higher N V / C IV ratio at higher SMBH masses. However, in the composite spectra sorted by luminosity at constant mass, N V shows a Baldwin Effect with approximately the same slope as C IV. This yields a nearly constant N V / C IV ratio across the full range of luminosities. We conclude that the Baldwin Effect is stronger with $M_{\rm SMBH}$ than with L and that the positive trend between N V REW and $M_{\rm SMBH}$ is due to increased nitrogen abundances (e.g., metallicities, see §5.4.1) offsetting the usual Baldwin Effect (see also Korista et al. 1998).

We also find a strong inverse correlation between SMBH mass and emission line peak heights. Figure 5-4 plots peak heights relative to the fitted continuum (I_p/I_c) versus SMBH mass and luminosity for several prominent emission lines. A comparison of Figures 5-3 and 5-4 show that the peak heights depend as strongly on SMBH mass as the REWs do. Also notice that, for a fixed SMBH mass, the REW of C IV still decreases with increasing luminosity, but the peak height of C IV remains fixed. There is also no trend between L and the peak height of C III] λ1909, while O VI and Lyα actually show trends for increasing peak heights with increasing luminosity.

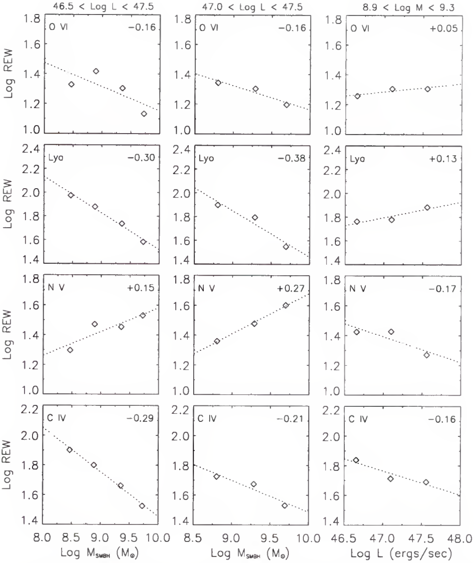

Figure 5–3 Emission line REWs (in angstroms) versus SMBH mass and luminosity for the same three composite spectra in Fig. 5-2. The dotted lines are linear fits to the data, with slopes given in the upper right. O VI, Lyα, and C IV all show much stronger anti-correlations between REW and SMBH mass than between REW and luminosity. N V shows a positive correlation between REW and SMBH mass but an anti-correlation between REW and luminosity.

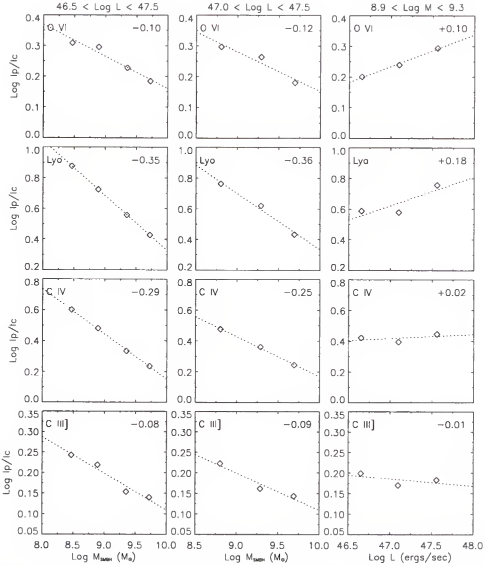

Figure 5–4 Emission line peak heights versus SMBH mass and luminosity for the same three composite spectra in Fig. 5-2. The peak heights decrease sharply with increasing SMBH mass, but remain constant or increase with increasing luminosity. The dotted lines are linear fits to the data with slopes given in the upper right.

5.5 Discussion

5.5.1 BLR Metallicities

The main result from §5.4 is that emission line flux ratios diagnostic of BLR metallicity show a strong positive correlation with SMBH mass but no trend with luminosity (Figures 5-1 & 5-2). This is consistent with the hypothesis in §5.1, that if the BLR gas was enriched by stars in the AGN's host galaxy, there might be a natural trend between BLR metallicity and SMBH mass. This trend should have roughly the same slope as the mass-metallicity relation in elliptical galaxies. For the composite spectra that span a range in SMBH mass at nearly constant luminosity, we estimate an overall metallicity by averaging the results of N III]/O III], N V/He II, and N V/(C IV+O VI). We employ a χ^2 minimization routine to obtain a linear fit to a plot of this average metallicity vs. SMBH mass (Figure 5-5). The fitted slope of $\Delta Z/\Delta M \sim 0.37$ is consistent with the slope of ~ 0.3 for the mass-metallicity relation in elliptical galaxies (see the derivation in Warner et al. 2003 based on data in Bender et al. 1993; Zaritsky et al. 1994; van Albada et al. 1995; Trager et al. 2000). This further supports the idea that host galaxy mass, which scales directly with SMBH mass (Kormandy & Gebhardt 2001, see §5.1), is the factor most responsible for determining BLR metallicities.

It is also noteworthy that SMBH mass is the only quantity that shows a correlation with the line ratios diagnostic of metallicity. It has been suggested that the high metallicities exhibited by some NLS1s are due to high L/L_{edd} (Shemmer & Netzer 2002; Shemmer et al. 2004). However, Warner et al. (2004) found no trend between L/L_{edd} and metallicity in composite spectra created from different ranges in L/L_{edd} (see their Figure 10). Also, the objects with the highest L/L_{edd} ratios (luminous quasars with narrow lines) do not show enhanced metallicities. We conclude that a secondary parameter not related to L/L_{edd} must be enhancing the metallicities in (some) NLS1s. Our results here, for no trend between metallicity

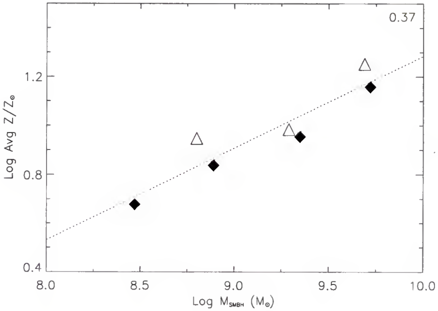

Figure 5–5 Average metallicity versus SMBH mass for the two sets of composite spectra that span a range in SMBH mass at nearly constant luminosity. The composites with $46.5 < \log L < 47.5$ ergs s^{-1} are represented by filled diamonds and the composites with $47.0 < \log L < 47.5$ ergs s^{-1} are represented by open triangles. The average metallicity is obtained by comparing individual line ratios to theoretical predictions in Hamann et al. (2002) and then averaging the results of N III]/O III], N V/He II, and N V/(C IV+O VI). The dotted line is a linear fit to all seven datapoints with the slope given in the upper right.

and L, FWHM, or L/L_{edd} at constant SMBH mass, support this conclusion (see Figure 5-2 and Table 5-1). The apparent discrepancy with Shemmer & Netzer (2002) and Shemmer et al. (2004) might be because their estimates of SMBH mass and L/L_{edd} are based on Hβ instead of C IV (§5.2). The 1:1 correlation between the SMBH masses determined from each of these emission lines holds well for composite spectra or averages of many objects, but there can be significant deviations for individual objects. In particular, there is a selection bias for NLS1s to have broader C IV compared to Hβ because NLS1s are classified based on extremely narrow (< 2000 km s^{-1}) Hβ lines. However, these objects compose a very small fraction of our sample as a whole.

5.5.2 The Baldwin Effect

Another key result of this study is that, in both the composite spectra and individual objects in our overall sample, the REWs of most prominent emission lines decrease more sharply with SMBH mass than with luminosity (Fig. 5-3). If L versus REW had been the more fundamental relationship, we should have found constant REWs at constant L instead of the strong trends in Figure 5-3 between REW and SMBH mass at constant L.

Figures 5-1 and 5-4 suggest that the line peak heights are even more closely coupled with SMBH mass than the REWs. In particular, the peak heights, unlike the REWs, remain nearly constant at constant SMBH mass. We can readily understand this result if the peak heights are more sensitive than the total REWs to the strength of the “narrow” core components of the broad emission lines (see Wills et al. 1993, Shang et al. 2003). Many studies have suggested that this narrow line core is the primary contributer to the Baldwin Effect (Francis et al. 1992; Osmer et al. 1994; Francis & Koratkar 1995; Shang et al. 2003). However, our results suggest that SMBH mass, and not luminosity, is the parameter that defines the strength of the narrow line cores. Note that this mass-driven behavior would naturally produce the observed Baldwin Effect because i) SMBH mass and luminosity are closely related, and ii) for any given SMBH mass, the peak heights are fixed but more luminous objects have narrower overall line profiles (based on the assumption of virialized motion) and thus lower overall REWs (see Fig. 5-1). We conclude that the Baldwin Effect is best understood as an inverse correlation between SMBH mass and the intensity of the narrow core of broad emission lines.

5.6 Summary and Conclusions

We have investigated a large sample of 578 AGNs for trends between the metallicity in the BLR and both SMBH mass and luminosity. The sample spans seven orders of magnitude in luminosity, five orders of magnitude in SMBH mass, and a redshift range from $0 \leq z \leq 5$ and contains new observations of faint quasars at redshift $z > 2.5$. We apply the virial theorem to the C IV $\lambda1549$ emission line to estimate SMBH masses and we estimate metallicities based on emission line flux ratios involving nitrogen. We isolate SMBH mass and luminosity by creating composite spectra that i) span a range in SMBH mass at nearly constant luminosity and ii) span a range in luminosity at nearly constant SMBH mass. We conclude that SMBH mass plays a critical role in defining AGN spectra. SMBH mass determines both emission line ratios (diagnostic of the metallicity) and the strengths of the narrow cores of the emission lines. Our main results are as follows.

1) Emission line flux ratios diagnostic of the metallicity in the BLR all show a strong trend with SMBH mass but no trend with luminosity or L/L_{edd} (Figure 5-2). This indicates that host galaxy mass, which correlates strongly with SMBH mass (see §5.1), is probably the fundamental parameter driving quasar metallicities.

2) Composite spectra sorted by SMBH mass in narrow ranges of both luminosity and FWHM(C IV) show an inverse correlation between SMBH mass and the REWs of emission lines such as Lyα, C IV, and O VI. This correlation is much stronger than the correlation between line REWs and L (the Baldwin Effect) in

composites that span a range in luminosity at nearly constant SMBH mass (Figures 5-1 & 5-3).

3) In the composites that span a range in L at nearly constant $M_{\rm SMBH}$, N V shows an inverse correlation between equivalent width and luminosity with approximately the same slope as C IV. The composites at nearly constant L and FWHM(C IV) show a positive correlation between N V REW and SMBH mass. This correlation may be understood as increased nitrogen abundances, due to "secondary" N production, offsetting the anti-correlation between SMBH mass and equivalent width.

4) We find a strong inverse correlation between SMBH mass and emission line peak heights (Figure 5-4). In addition, all of our composite spectra show constant peak heights at constant SMBH mass, but equivalent widths do not remain constant at either constant SMBH mass or constant luminosity. This suggests that the correlation driving the Baldwin Effect may be between SMBH mass and the strength of the "narrow cores" of emission lines.

CHAPTER 6

ON THE RELATIONSHIP BETWEEN METALLICITY AND EMISSION LINE VELOCITY WIDTHS IN AGNS

6.1 Introduction

The broad emission-line spectra of active galactic nuclei (AGNs) provide valuable information on the physical state and chemical composition of the gas in the broad emission-line region (BLR). If the gas in the BLR was processed and enriched by the surrounding stellar environment, then the element abundances we measure from the emission lines are a useful probe of the star formation history in these environments (see Hamann & Ferland 1999). Warner, Hamann & Dietrich (2003, 2004 in prep) found a direct correlation between the metallicity of the gas in the BLR and the mass of the central supermassive black hole (SMBH). This correlation can be understood in terms of more massive SMBHs residing in more massive host galaxies, combined with the well known mass-metallicity relationship among galaxies (see Warner et al. 2003, 2004 in prep for more details).

Warner, Hamann & Dietrich (2004, in prep) also found that SMBH mass is the only property that correlates with BLR metallicity. In particular, BLR metallicity does not depend on the FWHM of individual emission lines at constant SMBH mass. Composite spectra at nearly constant FWHM(C IV λ1549) exhibit the usual correlation between metallicity and SMBH mass, while composites at nearly constant SMBH mass show no trend between metallicity and FWHM(C IV).

Some recent studies have suggested that Narrow Line Seyfert 1s (NLS1s) depart from this relationship between metallicity and SMBH mass, with some NLS1s having metallicities as high as those measured in high-luminosity, high-redshift quasars (Mathur 2000; Shemmer & Netzer 2002; Shemmer et al. 2003; Shemmer et al. 2004). NLS1s are a subclass of Seyfert 1 galaxies that exhibit distinct and unusual properties: very narrow Hβ emission lines (<2000 km s^{-1}) with [O III] λ5007 / Hβ ratios of less than 3 (to exclude Seyfert 2s), strong Fe II emission, and unusually strong big blue bumps (Osterbrock & Pogge 1985; Kuraszkiewicz et al. 2000; Constantin & Shields 2003). NLS1s also land at one extreme end of the Boroson & Green (1992) Principal Component 1 (PC1). It has been suggested that PC1 is strongly correlated with the accretion efficiency parameter L/L_{edd} (Boroson & Green 1992; Boroson 2002; Shemmer & Netzer 2002; Constantin & Shields 2003) and that NLS1s have low SMBH masses for their luminosities and thus high L/L_{edd} (Mathur 2000; Kuraszkiewicz et al. 2000; Shemmer & Netzer 2002; Shemmer et al. 2003; Shemmer et al. 2004). Some studies have therefore hypothesized that the enhanced metallicities in NLS1s are caused by their high L/L_{edd} and that AGN metallicity is more strongly correlated with L/L_{edd} than SMBH mass or luminosity (Shemmer & Netzer 2002; Shemmer et al. 2004).

However, Warner et al. (2004) found no correlation between metallicity and L/L_{edd} in composite spectra spanning a wide range in L/L_{edd} at nearly constant SMBH mass. Furthermore, luminous, narrow-lined quasars with the highest L/L_{edd} values do *not* have enhanced metallicities for their SMBH masses. Therefore, we conclude that there must be some secondary effect, not related to L/L_{edd}, that is enhancing the metallicities in NLS1s. In this paper, we examine a large sample of AGNs and study the metallicities of NLS1s and the correlation between AGN metallicity and the ratio of full widths at half maximum, FWHM(C IV)/FWHM(Hβ).

We estimate metallicities based on emission line ratios involving nitorgen, specifically N III] λ1751/O III] λ1665, N III]/C III] λ1909, N V λ1240/He II λ1640, and N V/C IV. These line ratios are useful in estimating metallicity when secondary nitrogen production dominates (i.e., for $Z \gtrsim 0.2$ $Z_{\odot}$) because nitrogen abundances then scale as N/H $\propto Z^2$ and N/O scales as Z = O/H (Shields 1976; Tinsley 1980; Wheeler et al. 1989; Hamann & Ferland 1992, 1993, 1999; Ferland et al. 1996; Henry et al. 2000; Hamann et al. 2002; Pilyugin 2003; Pilyugin et al. 2003).

6.2 Data & Analysis

Our research group has compiled spectra of over 800 Type 1 (broad-line) AGNs, 578 of which have rest-frame UV wavelength coverage and 72 of these also have measurements of Hβ (see Dietrich et al. 2002, 2004 in prep; Warner et al. 2004 for details). The sample includes 25 objects that were classified by others as NLS1s, according to the criteria described in §6.1 (Kuraszkiewicz et al. 2000; Wang & Lu 2001; Constantin & Shields 2003). Eighteen of the NLS1s have measurements of C IV and twelve have measurements of Hβ.

We estimate the SMBH mass of each AGN by applying the virial theorem to the line-emitting gas (see Wandel et al. 1999; Kaspi et al. 2000; Vestergaard 2002; Corbett et al. 2003; Warner et al. 2003). We select the C IV λ1549 emission line instead of Hβ to estimate SMBH masses because it is more readily observable across our entire redshift range from $z \sim 0$ to $z \sim 5$. There is approximately a 1:1 correlation between the SMBH mass obtained from C IV and that obtained from Hβ. Individual objects can show significant deviations from this correlation, but it holds well for averages of many objects (Vestergaard 2002; Warner et al. 2003). For each individual object, we use the observed quantities FWHM(C IV) and λL_λ(1450Å) to estimate the SMBH mass, $M_{\rm SMBH}$, the bolometric luminosity, L, and the accretion efficiency parameter, L/L_{edd} (see Warner et al. 2003, 2004 for details). We use the cosmological paramaters $\rm H_0$ = 65 km s^{-1} Mpc^{-1}, $\Omega_M = 0.3$, and $\Omega_\Lambda = 0$ (Carroll, Press, & Turner 1992) throughout this paper[1] .

---

[1] The use of this cosmology was motivated for comparison with earlier studies in the pre-WMAP era. Furthermore, the difference between this set of cosmological

We create composite spectra defined by various criteria, based on procedures outlined in Warner et al. (2003, 2004). We remove the Fe II and Fe III emission from these composites, normalize the continua to unity, and measure the broad emission lines using a spectral fitting routine developed in the IDL language. The routine employs χ^2 minimization and fits each line with one or more Gaussian profiles. We estimate the 1σ standard deviations of our line flux measurements to be $\lesssim$10% for strong lines such as Lyα and C IV and ~10–20% for weaker or more blended lines.

6.3 Composite Spectra

Table 6-1 summarizes various parameters for the composite spectra created for this study, including the mean values of FWHM(C IV), FWHM(Hβ), FWHM(C IV)/FWHM(Hβ), the redshift z, and L, as determined from the individual objects contributing to each composite. Also listed are the number of objects contributing to each composite at the wavelengths of C IV and Hβ and the average metallicity of each composite as determined from the line flux ratios listed in §6.1.

Warner, Hamann & Dietrich (2004) found that a composite spectrum of the 25 NLS1s in our sample has a metallicity that is slightly high compared to composite spectra created from our entire sample with similar L and $M_{\rm SMBH}$, although still well below the high metallicities exhibited by luminous quasars with the most massive SMBHs. Furthermore, we find that the NLS1 composite has a significantly higher metallicity than a composite spectrum created from low-redshift AGNs with narrow (< 3000 km s^{-1}) C IV (including several NLS1s). Therefore, either the non-NLS1s in this composite spectrum are lowering its metallicity or the NLS1s with FWHM(C IV) > 3000 km s^{-1} are enhancing the metallicity in the

---

parameters and those suggested by WMAP results in a difference of less than 20% in luminosity for a wide redshift range of $0 < z < 4$ (Dietrich et al. 2004, in prep).

Table 6-1. Composite Parameters

# Objects at C IV	# Objects at Hβ	FWHM(C IV) [km s^{-1}]	FWHM(Hβ) [km s^{-1}]	FWHM(C IV)/ FWHM(Hβ)	z	Log L [ergs s^{-1}]	Log $< Z >$ [Z$_\odot$]
Overall NLS1s							
18	12	3000	1500	2.02	0.06	45.54	0.51
Narrow Versus Broad C IV NLS1s							
11	8	2200	1500	1.74	0.06	45.53	0.41
7	4	4100	1600	2.58	0.09	45.79	0.82
2000 km s^{-1} < FWHM(Hβ) < 4000 km s^{-1}							
24	24	3200	3000	1.10	0.33	46.69	0.28
12	12	4900	2800	1.76	0.48	47.21	0.56
FWHM(C IV)/FWHM(Hβ) Composites							
29	29	3200	3800	0.88	0.40	46.77	0.35
22	22	3700	2800	1.33	0.18	46.15	0.37
21	21	4600	2100	2.35	0.33	46.97	0.57
9	9	4000	1300	2.96	0.14	45.70	0.60

NLS1 composite. In order to more thoroughly examine this phenomenon, we create separate composite spectra of NLS1s with narrow (< 3000 km s^{-1}) and broad ($>$ 3000 km s^{-1}) C IV (see Figure 6-1) and measure the emission line ratios diagnostic of metallicity (§6.1). All four of the ratios indicate that the NLS1 composite with broad C IV has a much higher metallicity than the NLS1 composite with narrow C IV, with some line ratios indicating a difference in metallicity of greater than a factor of two (Figures 6-1 & 6-2). N V $\lambda1240$ and N III] $\lambda1751$ are roughly the same strength in both composites. However, C IV, He II $\lambda1640$, O III] $\lambda1665$, and C III] $\lambda1909$ are all much weaker in the NLS1s with broad C IV.

In order to test whether this behavior is unique to NLS1s, we create composite spectra sorted by FWHM(C IV)/FWHM(Hβ) for objects with intermediate-width Hβ (2000 km s^{-1} $<$ FWHM(Hβ) $<$ 4000 km s^{-1}) (spectra not shown). Again, the objects with broader C IV *compared to Hβ* show higher metallicities (Figure 6-2). Finally, we create composite spectra from our entire sample for different ranges in FWHM(C IV)/FWHM(Hβ) (see Figure 6-1). These composites are consistent with a trend between FWHM(C IV)/FWHM(Hβ) and the line ratios diagnostic of metallicity (Figure 6-2).

6.4 Results & Discussion

Warner, Hamann, & Dietrich (2004, in prep) found that BLR metallicity does not correlate with AGN luminosity, FWHM(C IV), or *L/L_{edd} at constant SMBH mass.* Therefore, the high metallicities (for their L and $M_{\rm SMBH}$) measured in some NLS1s (Mathur 2000; Shemmer & Nezter 2002; Shemmer et al. 2004) must be enhanced by some unknown secondary effect, not related to L, FWHM(C IV), or L/L_{edd}. We find that not all NLS1s exhibit these high metallicities: NLS1s with narrow (< 3000 km s^{-1}) C IV lines have metallicities consistent with other AGNs of similar $M_{\rm SMBH}$ and L and thus do not depart from the relationship between metallicity and SMBH mass. Only the NLS1s with broad C IV have enhanced

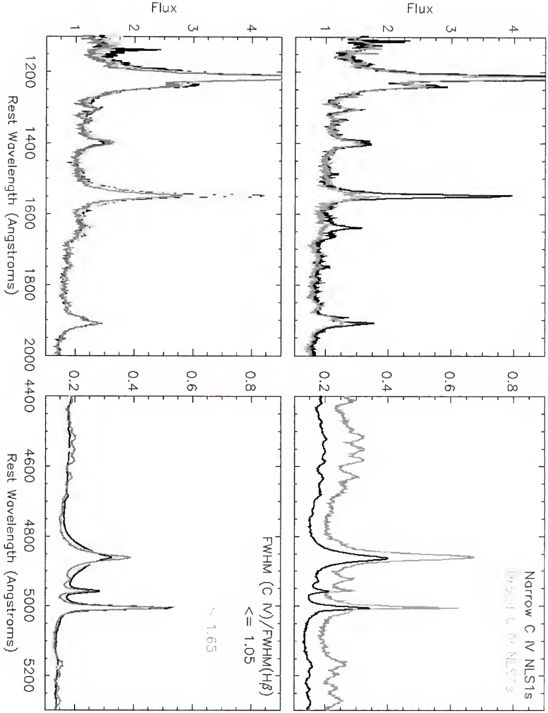

Figure 6–1 Composite spectra of NLS1s with narrow and broad C IV λ1549 lines (top) and composite spectra created from our entire sample for different ranges in FWHM(C IV)/FWHM(Hβ λ4861) (bottom). In both comparisons, the N V λ1240 and N III] λ1751 lines stay nearly constant, while the objects with broader C IV *compared to Hβ* have much weaker C IV, He II λ1640, O III] λ1665, and C III] λ1909 emission lines.

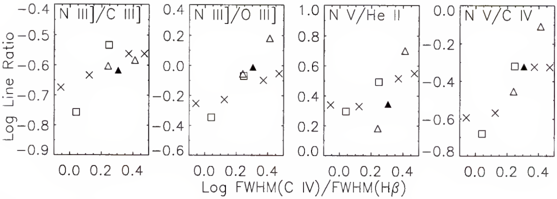

Figure 6–2 Emission line ratios diagnostic of metallicity are plotted (without error bars for clarity) versus FWHM(C IV)/FWHM(Hβ) for various composite spectra (see §6.3 and Table 6-1). The filled triangle represents our overall NLS1 composite while the open triangles represent the separate NLS1 composites created from objects with narrow and broad C IV lines. The squares represent the composites created from objects with 2000 km s^{-1} < FWHM(Hβ) < 4000 km s^{-1} and sorted by FWHM(C IV)/FWHM(Hβ). The ×'s represent the composites created from our entire sample for different ranges in FWHM(C IV)/FWHM(Hβ). All sets of composite spectra show a trend for higher metallicities when C IV is broader compared to Hβ.

metallicities. Furthermore, this behavior is not unique to NLS1s. We find that composite spectra created from our entire sample show the same behavior for higher metallicities, based on line ratios involving both N V and N III], at higher FWHM(C IV)/FWHM(Hβ) ratios, independent of SMBH mass, L, individual line FWHMs, or L/L_{edd}. The physical reason for this behavior is unknown.

It should be noted that because NLS1s are classified based on extremely narrow Hβ lines (see §6.1), selecting a sample of NLS1s preferentially selects objects with broader C IV compared to Hβ. Therefore, a larger fraction of NLS1s than AGNs in general exhibit enhanced metallicities due to high FWHM(C IV)/FWHM(Hβ) ratios.

6.5 Summary & Conclusions

We have investigated the enhanced metallicities measured in NLS1s by studying various composite spectra created from subsamples of a large sample of 578 AGNs. Our main results are as follows.

1) While the N v and N iii] lines are roughly the same strength in composite spectra of NLS1s with broad (> 3000 km s^{-1}) and narrow C iv, the composite created from NLS1s with broad C iv has much weaker C iv, He ii, O iii], and C iii] emisssion lines and thus a much higher metallicity (based on the line flux ratios listed in §6.1) than the composite spectrum created from NLS1s with narrow C iv (see Figures 6-1 & 6-2).

2) An examination of our entire AGN sample shows that this result for the NLS1s is part of a general trend. In particular, rare objects with broad C iv compared to Hβ have higher metallicities, based on emission line ratios involving *both N*v *and N*iii*]*, than objects with small or intermediate FWHM(C iv)/FWHM(Hβ) ratios (Figures 6-1 & 6-2). The physical reason for this behavior is unknown.

3) While objects with broad C iv compared to Hβ (and thus enhanced metallicities) compose only a small fraction of our sample as a whole, they represent a significant fraction of NLS1s. This is due to a selection bias for NLS1s to have broad C iv compared to Hβ because NLS1s are classified based on having extremely narrow (< 2000 km s^{-1}) Hβ lines.

CHAPTER 7
SUMMARY AND CONCLUSIONS

Studying quasars allows us to probe the early universe. In particular, if the gas near quasars was processed by the surrounding host galaxy then the element abundances we measure from the emission lines provide valuable information about star formation and galaxy evolution. I obtained the spectrum of a redshift 4.16 quasar, BR2248-1242, and performed the most comprehensive emission-line abundance analysis to date for a $z > 4$ quasar. I find that even at redshifts of $z > 4$, the gas close to quasars has a metallicity of solar or greater. This implies that an episode of rapid and extensive star formation occured before the observed epoch of ~ 1.5 Gyr after the Big Bang. This evidence for high metallicities and rapid star formation is consistent with both previous emission line results (Ferland et al. 1996; Korista et al. 1998; Hamann & Ferland 1999; Dietrich & Wilhelm-Erkens 2000; Hamann et al. 2001) and recent simulations, which show that the densest proto-galactic condensations can form stars and reach solar or higher metallicities at $z \gtrsim 6$ (Ostriker & Gnedin 1997; Haiman & Loeb 2001).

This is among the first studies to use C IV λ1549 to extend SMBH mass estimates out to the highest redshifts. I compare the SMBH mass estimated from C IV to that estimated from Hβ for all 74 objects in our sample with observations of both lines and find approximately a 1:1 correlation. Individual objects can deviate significantly from this trend, but the relation holds well for averages of many objects and measurements based on composite spectra.

Previous studies have shown that BLR metallicity correlates with AGN luminosity, with the tentative hypothesis that the metallicities are driven by host galaxy mass (Hamann & Ferland 1992, 1993, 1999). I examine a large sample of

578 AGNs and make the first comparisons between metallicity and SMBH mass, which correlates directly with host galaxy mass. I also study the dependence of metallicity and other emission line properties on SMBH mass, luminosity, and accretion efficiency by creating composite spectra that isolate these three parameters from each other for the first time. I find that BLR metallicity shows a strong correlation with SMBH mass, but no correlation (at constant SMBH mass) with luminosity, accrection efficiency, emission line FWHM, or redshift. Moreover, the slope of the trend between SMBH mass and metallicity is consistent with the slope of the mass-metallicity relationship among galaxies. Thus, the direct correlation between SMBH mass and quasar metallicity can be understood in terms of more massive SMBHs residing in more massive host galaxies, combined with the well-known galactic mass-metallicity relationship. This correlation also contributes to the growing evidence for a close relationship between quasars and their host galaxies (e.g., Shields et al. 2002).

In agreement with previous studies, I find that NLS1s generally have high Eddington ratios for their luminosities and also exhibit slightly enhanced metallicities for their SMBH masses. However, there is no trend between L/L_{edd} and metallicity in our sample as a whole. Futhermore, the objects with the highest L/L_{edd} (luminous, narrow-lined quasars) do not have high metallicities for their SMBH masses. Upon further examination, I find that only NLS1s with broad (> 3000 km s^{-1}) C IV have enhanced metallicities and that NLS1s with narrow C IV have metallicities that are consistent with other AGNs of similar $M_{\rm SMBH}$. I find that this behavior is part of a general trend in our overall sample for enhanced metallicities in rare objects with broad C IV *compared to Hβ*. The physical reason for this behavior is unknown. Because NLS1s are classified based on extremely narrow (< 2000 km s^{-1}) Hβ lines, there is a selection bias for NLS1s to have broad C IV compared to

Hβ. Therefore, a larger fraction of NLS1s than AGNs in general exhibit enhanced metallicities due to high FWHM(C IV)/FWHM(Hβ) ratios.

I also find an unusual and interesting emission-line behavior: composite spectra that have nearly the same average SMBH mass will also have nearly constant line peak heights (relative to the continuum), regardless of average luminosity, emission line FWHM, or L/L_{edd}. This behavior is in marked contrast to the usual Baldwin Effect: decreasing line peak heights and equivalent widths with increasing luminosity. I find that the REWs of strong emission lines such as Lyα, C IV, and O VI show a stronger inverse correlation with SMBH mass than with luminosity. If luminosity versus REW had been the fundamental driver behind the Baldwin Effect, we should have found nearly constant REWs at constant L instead of a strong inverse correlation between REW and $M_{\rm SMBH}$. Furthermore, the line peak heights, unlike the REWs, remain nearly constant at constant SMBH mass. This result can be understood if the peak heights are more sensitive than the total REWs to the strength of the "narrow core" components of the broad emission lines (see Wills et al. 1993; Shang et al. 2003). Therefore, I conclude that the fundamental driver behind the Baldwin Effect is an inverse correlation between SMBH mass and the equivalent widths of the narrow emission line cores.

Finally, I conclude that SMBH mass plays a critical role in defining the spectra of quasars and AGNs in general. SMBH mass determines both emission line ratios (diagnostic of metallicity) and the strengths of the narrow cores of the emission lines.

APPENDIX A
DETAILS OF LINE FITTING PROCEDURE

We fit C IV λ1549 with three Gaussian profiles. Three Gaussians are necessary to obtain a good fit because the emission lines are not Gaussian by nature and contain broad wings. We ignore the doublet splitting in C IV because it is small compared to the observed line widths. N IV] λ1486, where it is measureable, is fit with a C IV profile. That is, we fit it with three Gaussian profiles that have their FWHMs tied to the values fit to C IV and their relative fluxes and relative wavelength shifts are tied to the same ratios as in the fit to C IV. For the two highest mass composite spectra, we fit only an upper-bound to N IV] because it is too blended with the wing of C IV to measure. He II λ1640 is fit with two Gaussian profiles, one broad and one narrow and O III] λ1665 is fit with a C IV profile. The weak and badly blended doublet Si II $\lambda\lambda$1527, 1533 is fit with one Gaussian profile for each component.

Lyα λ1216, like C IV, is fit with three Gaussian profiles, but only the red side of the line is used for χ^2 minimization because of contamination by the Lyα forest on the blue side. Each component of the N V λ1240 doublet is fit with a C IV profile because N V is strongly blended with the wing of Lyα. This connection between C IV and N V can be justified because they are both high ionization lines with similar excitation properties (Ferland et al. 1998). The relative fluxes of the two components of the N V doublet are set to the ratio of the statistical weight, g, times the A value for each transition (approximately 2:1 in this case), because this yields a better fit than using a 1:1 ratio. We use atomic data obtained from the National Institute of Standards and Technology (http://aeldata.phy.nist.gov/PhysRefData/contents-atomic.html) to calculate

g times the A value for each transition. The weak and blended multiplet Si II $\lambda\lambda1260, 1264, 1265$ is fit with one Gaussian profile for each component.

We fit O I $\lambda1303$ with a single Gaussian profile and C II $\lambda1335$ with two Gaussians, one for each component of the doublet. The fluxes of the two C II components are tied to a 1:1 ratio because this yields a better fit than a 2:1 ratio. The FWHMs and relative wavelengths are also tied together.

We fit the doublet Si IV $\lambda\lambda1393, 1403$ with one Gaussian profile for each of the two components. The fluxes of these components are tied to a 1:1 ratio because this yields a better fit than a 2:1 ratio. O IV] $\lambda1403$, a blended multiplet of five lines, is fit with one Gaussian profile for each of its five components. The flux ratios of the components in this case are tied to the ratio of g times the A value for each transition using atomic data obtained from Nussbaumer & Storey (1982). Because Si IV and O IV] are badly blended, we tie the FWHMs and relative wavelengths together for all seven components of the Si IV - O IV] blend. We list the sum of the blend in Table 3-2.

We fit the N III] $\lambda1750$ multiplet with five C IV profiles, one for each component of the multiplet. We use C IV profiles to constrain the fit because N III] is a weak intercombination line. The relative fluxes of the five components are tied to the ratio of g times the A value for each transition because this yields the best fit. The FWHMs and relative wavelengths are all tied together.

We use two Gaussian profiles to fit C III] $\lambda1909$ because two Gaussians provide a fit that is just as good as the fit obtained by using three Gaussians. The Al III $\lambda\lambda1855, 1863$ doublet is fit with one Gaussian profile for each component. The flux ratio is tied to the ratio of g times the A value for each transition and the FWHMs and relative wavelengths of both components are tied together. Si III] $\lambda1892$ is fit with one Gaussian profile and has its FWHM and relative wavelength tied to Al III because it is badly blended with C III].

We fit a local continuum around O VI $\lambda1035$, which was constrained by the flux in wavelength intervals centered at 960 Å and 1100 Å. We then fit each component of the O VI $\lambda1035$ doublet with two Gaussian profiles. The fluxes are tied to a 3:2 ratio, compromising between 1:1 and 2:1, because this yields the best fit. Where they are measureable, C III $\lambda977$ and N III $\lambda990$ are fit with one Gaussian profile each, and their FWHMs and relative wavelengths are tied together. When calculating fluxes from measured REWs, we scale O VI as if it were sitting on top of a segmented powerlaw continuum, defined by our previous continuum fit redward of 1250 Å and by a powerlaw with index $\alpha = -1.76$ (Telfer et al. 2002) blueward of 1250 Å.

Each of the five spectra is fit in this fashion, with the following exceptions for the broadest ($M \sim 10^{10}$ M$_\odot$) spectrum, which has many extremely blended lines. In this spectrum, we tie the relative wavelengths of the three Gaussian profiles used to fit C IV and Lyα and the two Gaussian profiles used to fit C III] to the corresponding ratios from our fit to the $M \sim 10^9$ M$_\odot$ sample. We do not attempt to fit N IV] or Si II $\lambda\lambda1527, 1533$, as they are undetectable due to the broad wing of C IV. It should also be noted that in our fit to this spectrum, the broader Gaussian profile of our fit to He II is blueshifted by 15 Å.

APPENDIX B
LINE FITTING WITH GATORPLOT

Beginning with chapter 4, all of my line fitting was done with GatorPlot (see Appendix C), a software package I developed in the IDL programming language. GatorPlot provides more reliable fits and more versatile fitting options than IRAF and also performs the fits hundreds of times faster. In particular, the gpfitmg procedure allows one to better constrain the fits to weak or blended lines by fitting multiple Gaussian profiles to a particular emission line and simultaneously fitting scaled versions of that line's overall profile to other emission lines.

We first fit the continuum with a powerlaw of the form $F_\nu \propto \nu^\alpha$ using the gpfitplw procedure. The fit was constrained by the flux in wavelength intervals centered at 1450 Å, 1990 Å, and when possible 1720 Å.

After normalizing the continuum to unity, we again fit C IV λ1549 with the three Gaussian profiles necessary to obtain a good fit. We simultaneously fit N IV] λ1486, He II λ1640, and O III] λ1665 each with a C IV profile. We ignore the very weak and badly blended doublet Si II $\lambda\lambda$1527, 1533.

Lyα λ1216, like C IV, is fit with three Gaussian profiles, but only as little as possible of the blue side of the line is used for χ^2 minimization because of contamination by the Lyα forest. Generally, 1210-1285 Å is the wavelength range used for χ^2 minimization because this excludes the contaminated blue wing of Lyα, while still fitting the line peak well. Each component of the N V λ1240 doublet is fit with a C IV profile because N V is strongly blended with the wing of Lyα. The relative fluxes of the two components of the N V double are set to the ratio of the statistical weight, g, times the A value for each transistion (approximately 2:1 in this case) because this yields a better fit than using a 1:1 ratio. The weak and blended multiplet Si II $\lambda\lambda$1260, 1264, 1265 is fit with one Gaussian profile for each component. The fluxes and FWHMs of each Gaussian are tied to a 1:1 ratio and the relative wavelengths are tied to a fixed ratio.

We fit O I λ1303 with a single Gaussian profile and C II λ1335 with one Gaussian for each component of the doublet. The fluxes and FWHMs of the two C II components are tied to a 1:1 ratio and the relative wavelengths are fixed.

Because the doublet Si IV $\lambda\lambda$1393, 1403 is so badly blended with the multiplet O IV] λ1403, we simply fit two Gaussian profiles to the entire blend. Our goal is simply to measure the total strength of the blend and each individual Gaussian has no physical meaning.

We fit N III] λ1750 with five C IV profiles, one for each component of the multiplet, because it is a weak line. The relative fluxes of the five components are tied to the ratio of g times the A value for each transition because this yields the best fit and the relative wavelengths are tied to fixed values so that only one flux value and one wavelength are allowed to float.

We fit C III] λ1909 with just two Gaussian profiles because this provides just as good a fit as that obtained with three Gaussians. Al III λ1855, 1863 is fit with one Gaussian profile for each component of the doublet. The relative fluxes are tied to the ratio of g times the A value for each transition and the FWHMs and relative wavelengths of both components are tied together. Si III] λ1892 is fit with one Gaussian profile. When it is badly blended, its FWHM is tied to the FWHM of Al III and its relative wavelength is tied to the narrower of the two Gaussians fit to C III].

We fit a local continuum around O VI λ1035, which was constrained by the flux in wavelength intervals centered at 950 Å and 1100 Å. We then fit each component of the O VI doublet with two Gaussian profiles. The fluxes of the two components are tied to a 3:2 ratio, compromising between 1:1 and 2:1, because this yields the best fit. When they are measureable, C III $\lambda 977$ and N III $\lambda 990$ are fit with one Gaussian profile each, and their FWHMs and relative wavelengths are tied together. When calculating fluxes from measured REWs, we scale O VI, C III, and N III as if they were sitting on top of a segmented powerlaw continuum, defined by our previous continuum fit redward of 1250 Å and by a powerlaw with index $\alpha = -1.76$ (Telfer et al. 2002) blueward of 1250 Å.

APPENDIX C
GATORPLOT DOCUMENTATION

C.1 Overview

GatorPlot is a software package designed in the IDL programming language to interactively plot, fit, and manipulate data from one or more FITS or ASCII files or functions. I developed GatorPlot while working on my dissertation, adding features as I needed them, because the current available software was very inadequate. Beginning with chapter 4, everything for my dissertation was done using GatorPlot. Documentation and downloads for GatorPlot are available on the web at http://www.astro.ufl.edu/~warner/GatorPlot/. To install GatorPlot, simply download the files gatorplot.pro and gatorplot_config.pro and place them anywhere in your IDL_PATH. The files are then executed by simply typing "gatorplot" or "gatorplot_config" at any IDL command prompt. GatorPlot can be used via an interactive graphical user interface (GUI) or a scripting language, GPScript. A large portion of the GUI is the graphing window and to the left of that window and below it are buttons and text areas that control all of the plot options (see Figure C-1). GPScript allows scripts to be written to do anything automatically instead of interactively.

The program gatorplot_config allows you to specify a default directory to select files from, the location to save the temporary file gatorplotvars.dat in, the location of the gatorplot.help file, and a command to start your web browser of choice. The default values are your current directory, $HOME, $IDL_DIR/contrib/astroLib/text/gatorplot.help, and none, respectively.

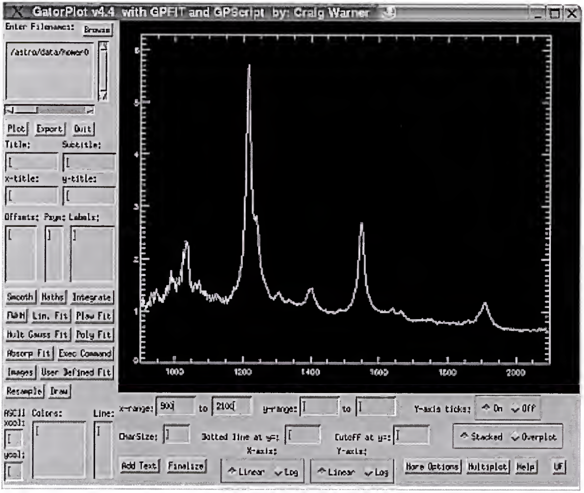

Enter Filenames: /astro/data/power0

Title:
Subtitle:
x-title:
y-title:
Offsets:
Psym:
Labels:
ASCII xcol:
ycol:
Colors:
Line:

x-range: 900 to 2100
y-range: to
Y-axis ticks: ● On ○ Off
CharSize:
Dotted line at y=:
Cutoff at y=:
● Stacked ○ Overplot
X-axis: ● Linear ○ Log
Y-axis: ● Linear ○ Log

Figure C–1 GatorPlot v4.4 plotting the rest-frame UV region of a composite spectrum.

This appendix includes documentation of every major feature of GatorPlot. When a version identifier appears next to a feature (i.e., v2.0+), it marks the first version of GatorPlot in which the feature was implemented.

C.2 Plotting Files

At the top left corner of the GUI are the "Enter Filenames" text area and the "Browse" button. Enter as many filenames as desired by either typing them directly into the text area or by clicking the "Browse" button to bring up a file selector that allows multiple selections. These selections are appended to anything already in the text area, allowing files from multiple directories to be chosen by clicking browse multiple times.

The types of files accepted by GatorPlot are .fits, ASCII files, and .list files. If a filename ends in .fits, it is assumed to be a FITS file. Note that the read_fits, write_fits, and sxpar procedures need to be in your current directory or IDL_PATH. If a filename ends in .list, it is assumed to be an ASCII file containing a list of FITS and/or ASCII filenames, one per line. If neither .fits or .list, the file is assumed to be an ASCII file. When plotting an ASCII file, a window will pop up asking for the X-axis and Y-axis columns in the file. Multiple columns can be added or subtracted, e.g., column 1 is your x-axis scale, and you want to plot column 2 + column 3 as the y-axis. Enter 1 for x-axis column and 2+3 for y-axis column. Similarly you could enter 4-2 or 3+5-4+7. If no value is entered for the X-axis column, element # in the y-axis array is used as the x-axis. You can also optionally enter a number of lines to skip at the start of a file. Click "OK" to proceed or "OK for all" if you want the same columns plotted for every ASCII file entered so you don't have to re-enter the column values.

Beginning with version 2.0, functions can be entered into gatorplot in the form f(x)=sin(x) or f(x)=x^ 2+3*x-7 in the file list text area. When you enter a function, you will be prompted for Xmin, Xmax, and the # of points you wish to use in calculating the function. All of these values are optional and if left blank will default to the min, max, and # of points of the first file in the list if there is another file.

The “Plot”, “Export”, and “Quit” buttons are located below the “Enter Filenames” box. Click the “Plot” button to generate the plot on the screen. Every time you click “Plot”, it will redraw the plot, and lose all text added after plotting. Clicking anywhere in the plotting window returns the X and Y coordinates of the mouse pointer to your terminal window.

Click the “Export” button to export the plot. You will be prompted for a filename and given a choice of format (Figure C-2). You can also (in v3.0 and above) choose to export as greyscale or color. Note that IDL does not support true color plots in the postscript device so if your display is set to true color, you must use Screenshot .PS to get a color .PS file (the same goes for printing and .PDF files). The format choices are as follows.

- Postscript: After selecting Postscript, you are given the option of specifying its Xsize and Ysize in inches and whether you want .ps, or .eps (Encapsulated Postscript). Then you can click Finalize or Don’t Finalize. If you click Finalize, the plot is sent to the specified file and is ready to be printed or opened in a PS viewer. If you click Don’t Finalize, the plot is sent, but the file remains open so that you can add text to it using the “Add Text” button at the bottom. You must then click the “Finalize” button, also at the bottom, to close the file
- JPEG: Everything currently on the screen (including text added to the plot) is sent to a JPEG file when you click Export.
- FITS: The data currently being viewed is exported to a .FITS file. Note that only the data from the first file in the file list is exported to the .FITS file,

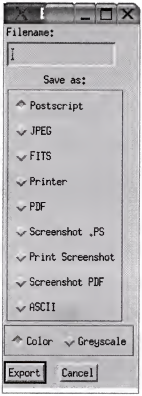

Figure C–2 GatorPlot's export window listing your choices of file formats.

and that only the portion of the data currently being viewed is sent to the .FITS file. So you can zoom in on a certain X-range and save only that part.

- Printer (works in Unix/Linux only): Sends the plot to your default printer. As with Postscript, you can specify the dimensions and click Finalize to print the plot, or click Don't Finalize and add text. Then when you click Finalize at the bottom, the plot with the text will be sent to the printer.
- PDF (works in Unix/Linux only): Same as Postscript except its sent to a .pdf file, viewable in Adobe Acrobat and Netscape.
- Screenshot .PS (v3.0): Screenshot .PS generates a Postscript file from the data currently in the plot window. Everything in the plot, including text that has been added is sent to the .PS file. To make it encapsulated, simply enter a .eps instead of .ps filename. The .PS file is automatically finalized so you can't add anything after exporting it.

- Print Screenshot (v3.0, Unix/Linux only): Same as Screenshot .PS except it sends the plot to your default printer.
- Screenshot PDF (v3.0, Unix/Linux only): Same as Screenshot .PS except its sent to a .pdf file.
- ASCII (v4.0): The x-axis and y-axis data are exported to a two-column ASCII file.

Clicking the "Quit" button quits GatorPlot.

C.3 Titles, Labels, Symbols, and Offsets

Under the "Plot", "Export", and "Quit" buttons are text fields labeled Title, Subtitle, x-title, y-title. Text entered in these fields will be displayed as the main title, subtitle, and corresponding axes titles on the plot.

If you are creating a stacked plot, use the Offsets text area to override the default offsets between the different plots. For n files, enter up to n-1 offsets. The first offset sets the y-value to be used as the "zero" value for the second file (overriding the default). The second line in offsets sets the y-value to be used for the third file, and so on.

In the Psym text area, you can enter a plotting symbol for each file. Leave blank or enter 0 for a line connecting the points. Enter 1-7 for different symbols (plus sign, asterisk, dot, diamond, triangle, square, and ×, respectively) or -1 to -7 for those symbols to be used and connected by a line. Enter 10 for histograms.

In the Labels text area, you can enter a short label for each file that will appear on the right side of the plot beyond the right y-axis. If creating a stacked plot, each label will appear next to the corresponding "zero" level. If overplotting data, the labels will appear from top (first file) to bottom (last file) of the right side.

C.4 Buttons

Click the "Smooth" button (v2.0+) to perform a smoothing function to your data. In the window that pops up, select Boxcar or Binomial smoothing, the number of points to bin by, and the number of iterations. For example, binning 3 points with boxcar smoothing would mean $x_2 = x_1/3 + x_2/3 + x_3/3$ while binning 3 points with binomial smoothing would result in $x_2 = 0.25x_1 + 0.5x_2 + 0.25x_3$.

The "Maths" button (v2.0+) can be used to perform arithmatic operations. A new window opens that has two text areas listing all the files, and next to each, text fields for scaling and x-offsets. You can select multiple files (or functions) in each text field and enter a scaling factor and an x-offset for each one. A constant can also be added. Then select the operation to perform between the two lists and click either plot or save (the result can be saved to a .fits or ASCII file). For example, if you wanted to plot File1 minus the constant 2, you could select File1 from the top text area and enter -2 in the +Constant box. If you wanted to plot (File1 - Function1) / (0.5 * File2), you would first select File1 and Function1 in the top text area and enter 1 and -1 in the first two rows of the Scale By box. Select "/" as your operation, select File2 in the lower text area, and enter 0.5 in the lower Scale By text field (Figure C-3). Finally, click either Plot or Save. X-offset is used if two files have different starting values so you can shift one relative to the other. Any arithmatic operation, from trivial to very complicated ones, can be performed on any set of files and functions with just a few clicks.

The "Integrate" button (v2.0+) performs an integration over a user-defined baseline. It can be used to integrate the flux of emission or absorption lines, to integrate functions numerically, or anything else. Clicking Integrate opens a new window that allows you to draw a baseline to integrate over. You can either enter a pair of (X,Y) coordinates for the start and finish of the line or left click on the graph window to obtain (X1,Y1) and right click to obtain (X2,Y2) coordinates by

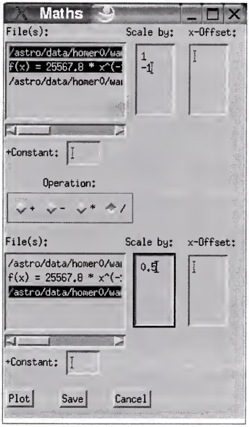

File(s):
/astro/data/homer0/wa
f(x) = 25567.8 * x^(-
/astro/data/homer0/wa

Scale by:
1
-1

File(s):
/astro/data/homer0/wa
f(x) = 25567.8 * x^(-
/astro/data/homer0/wa

Scale by:
0.5

Figure C–3 GatorPlot's maths window demonstrating one of the above examples.

mouse. Leaving the Y values blank results in them defaulting to 0. If you have more than one file listed in gatorplot, in either stacked or overplot mode, the integration will automatically be done for all files listed. Since there are a finite number of points in these functions and files, the integration is simply a sum that approximates the integral. This can be very useful in estimating fluxes of emission lines. Clicking Integrate returns 5 lines of information to your terminal window: filename (or function), Integration (flux), center x-axis value, Average f (continuum or baseline), and Equivalent Width. The baseline is overplotted as a dotted line.

The "FWHM" button (v2.0+) estimates the Full Width at Half Maximum of an emission or absorption line. Clicking FWHM opens a window that asks for the X and Y coordinates of two continuum points, one on either side of the line to be measured. It also asks for the X and Y coordinates of the peak of the line. This is optional and will be computed automatically if you leave these blank. The continuum points can be set by left clicking in the plot window at point1 and holding the mouse button down while you drag the pointer to point2. Then release the mouse. They can also be entered manually into the text fields. Right clicking enters the coordinates into X and Y peak. When you click FWHM, notice that a smoothed spectrum appears. The spectra are automatically smoothed by 5-point boxcar smoothing. This reduces the effect of noise on the measurement. The continuum is obtained by averaging 5 (already smoothed) points at each of the specified locations. If you do not specify the peak location, that is determined to be the maximum (smoothed) value in between the two continuum points. The program then determines the width of the line at half maximum and returns 4 lines to your terminal window: filename (or function), FWHM (in x-axis units), FWHM in km/s, and the center in x-axis units. This is very useful in measuring the FWHMs of strong lines, but may fail if lines become very blended. In that case, users must either guess at a local continuum or just click on either side of the line to obtain the X and Y coordinates and estimate the FWHM manually.

C.5 GPFIT

GPFIT was included with GatorPlot beginning with version 3.0. GPFIT refers collectively to all of GatorPlot's fitting routines. The "Lin. Fit" button (v3.0+) applies a linear fit of the form $Y = a + bX$ to your data using a chi-square minimization routine. You can select the ranges of data to be used in the fit by either entering them manually in the range box in the format low_x_value high_x_value. For instance, the example shown in Figure C-4 would use only data with x-axis values between 500 and 650 and between 712.5 and 842. Alternatively, you can just click on the screen to set the range. Click the left mouse button on the low x value, drag the mouse pointer to the high x value, and release the button. The range you selected will be appended to the range box. If the range box is left blank, it will use all the data for the fit. You can select no errors, poisson errors, or specify errors for each point from an input file. Note that the column of errors in the file must correspond point for point with Y_i, the individual y-axis values. Click Fit to do the fit. The results will be output to the screen and appended to a file linfit.gp in your current directory. A dotted line showing the fit will also be plotted on top of your data. A fit will be done for each file you have in the "Enter Filenames" box. Thus, you can automatically fit multiple files at once as long as you want to use the same range to fit each file.

The "Plaw Fit" button (v3.0+) fits a powerlaw of the form $Y = bX^a$ to your data using a chi-square minimization routine. You can select the ranges of data to be used in the fit as with the Linear Fit (see above). Choose no weighting (uniform) or Poisson weighting ($1.0/Y_i$). You may optionally enter your initial guesses for b and a. If either one or both are left blank, GatorPlot will generate initial guesses for you. Click Fit to perform the fit. The results will be output to

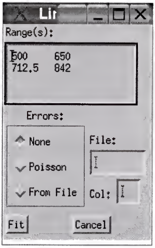

Range(s):

```
500     650
712.5   842
```

Errors: ● None ○ Poisson ○ From File

Figure C–4 An example of a linear fit to the range 500–650 and 712.5–842 Å.

the screen and appended to a file plawfit.gp in your current directory. A dotted line showing the fit will also be plotted on top of your data. Note that you can just copy the equation that is output to the screen right back into the "Enter Filenames box", substituting f(x) for Y and making sure to put parenthesis around a negative exponent, and plot the function yourself or enter Maths and divide the spectrum by the fit. The fit will be done for each file you have in the "Enter Filenames" box, so you can automatically fit multiple files at once as long as you want to use the same range to fit each file.

The "Mult Gauss Fit" button enables you to fit your data with one or more Gaussian profiles using a chi-square minimization routine. You can select the ranges of data to be used in the fit as with the Linear Fit (see above). Choose no weighting (uniform) or Poisson weighting ($1.0/Y_i$). If there is a constant offset from 0, you can enter that constant in the Constant box. For instance if you are fitting data that has been normalized to a continuum of 1, you would enter 1 in the Constant box. Initial guesses are mandatory, and there are two methods of inputting them. You can either give it a .gp filename that contains your initial guesses or enter the number of Gaussians you wish to fit in the #Gaussians box and enter the initial guesses of the parameters of each Gaussian in the Enter Fit Parameters box. The .gp file should have the following format.

```
number_of_Gaussians
flux1           factor tie_to   optional comments
wavelength1     factor tie_to   you can write anything
FWHM1           factor tie_to   you want to out here
flux2           factor tie_to
wavelength2     factor tie_to
FWHM2           factor tie_to
...
```

The wavelength is in whatever scale the x-axis is in, and the FWHMs are in km/s. For free parameters, just enter 0 for both factor and tie_to. To fix a parameter at a particular value (i.e., wavelength has to be 1549.0 and cannot float), enter -1 for factor and 0 for tie_to. To tie a parameter to a constant times the value of another parameter (i.e., FWHM3 = FWHM1 or flux2 = 2*flux1), enter the constant for factor (i.e., 1 or 2 in the examples), and enter the parameter to tie it to for tie_to. This is **not** the Gaussian number, but the parameter number, which starts at 0 for flux1, 1 for wavelength1, 2 for FWHM1, 3 for flux2, 4 for wavelength2, and so on. You may find it helpful to keep track of the parameter numbers in your optional comments space in the file. So for the example of flux2 = 2*flux1, I would enter 2 for factor and 0 for tie_to. Below is an example file.

```
2
15.0          0      0      param0
1549.0       -1      0      param1 fixed at 1549
3000          0      0      param2
30.0          2.0    0      param3 tied to 2*flux1
1549.0        0      0      param4
```

```
3000             1        2         param5 tied to 1*FWHM1
```

Finally, you can tie a parameter to a variable ratio. This is useful if you want to use the profile of one emission line to constrain the fit to another emission line. For example, you want to use the profile of C IV to fit O III], and use 2 Gaussians to fit each line: 1 and 2 to fit C IV and 3 and 4 to fit O III]. In this case, you would want flux4/flux3 = flux2/flux1 in order to maintain the C IV profile in the fit to O III]. You would then let flux1, flux2, and flux3 float and tie flux4 to (flux2/flux1)*flux3. This is done by entering -3.00 for factor and 6 for tie_to. The wavelength4 could similar be tied to (wavelength2/wavelength1)*wavelength 3 by entering -4.01 for factor and 7 for tie_to. If factor is negative and not an integer, GPFIT takes the integer part (of the absolute value) as the parameter number for the numerator and 100 times the fractional part (of the absolute value) as the parameter number for the denominator. It then multiplies this ratio by the value in the parameter given in tie_to just as it would do with a constant factor. If you want to enter the parameters into the Enter Fit Parameters box instead of providing an input file, they are entered in the exact same way except that number of Gaussians is left off since it has its own box. So the first line in the Enter Fit Parameters box would be the second line of the input file (i.e., parameter number 0, which is the flux for the first Gaussian. Figure C-5 shows an example in which an input file is used to fit multiple Gaussians to the flux in the wavelength interval 1450–1720 Å of a spectrum with the continuum normalized to unity.

Click Fit to perform the fit and the final fit parameters will be output to the screen. They will also be appended to a .gpfit file. You can optionally specify this filename by entering it in the Output (.gpfit) File text field. If no filename is entered, it defaults to multgaussfit.gpfit in your current directory. A .dat file is also created with the plot data. It is an ASCII file with the format

```
Xi  Total_Fit  Const  Gauss1  Gauss2  ...  GaussN
```

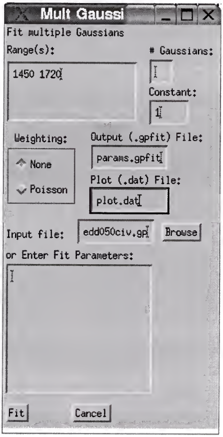

Range(s): 1450 1720

Gaussians:

Constant: 1

Weighting: ● None ○ Poisson

Output (.gpfit) File: params.gpfit

Plot (.dat) File: plot.dat

Input file: edd050civ.gp

or Enter Fit Parameters:

Figure C–5 An example of a multiple Gaussian fit to the wavelength range 1450–1720 Å. The continuum in the spectrum being fit has been normalized to unity, so 1 is entered as the constant. An input file contains the initial parameters.

and thus contains N+3 columns for a fit of N Gaussians. This filename can be specified in the Plot (.dat) File text field. If no filename is entered, it defaults to gpmultgaussfit.dat in your current directory. Your fit is then plotted over your data. Each individual Gaussian is plotted in one of five colors, with a dahsed line. The overall fit is then plotted in a solid blue-green line over top of your data. The fit will be done for each file you have in the Enter Filenames window, so you can automatically fit multiple files at once as long as you want to use the same range to fit each file and as long as the initial guesses are valid for each file. If the fit is unsatisfactory or the chi-square fails to converge, you should modify your initial guesses and try again. Once you have a satisfactory fit, you can export it to a postscript file using the Screenshot .PS option in the Export menu. Figure C-6 shows the result of a fit to the data shown in Figure C-5.

Click the "Poly Fit" button (v3.0+) to fit a polynomial of the form $Y = a_0 + a_1X + a_2X^2 + ... + a_nX^n$ to your data using a chi-square minimization routine. You can select the ranges of data to be used in the fit as with the Linear Fit (see above). Choose no weighting (uniform) or Poisson weighting ($1.0/Y_i$). Note that Poisson weighting can not be used if one of your data values is 0 since 1.0/0 is infinite. Enter the order of the polynomial you want to fit: 0 is a constant, 1 a linear fit, 2 quadratic, 3 cubic, and so on. Then you can optionally enter your initial guesses to the polynomial coefficients. Enter them one per line in the Init Coeff box, in the order a_0 (constant term), a_1 (linear term), a_2, and so on. Then click Fit to perform the fit. The results will be output to the screen and appended to a file polyfit.gp in your current directory. A green dashed line showing the fit will also be plotted on top of your data. The fit will be done for each file you have in the Enter Filenames window, so you can automatically fit multiple files at once as long as you want to use the same range to fit each file.

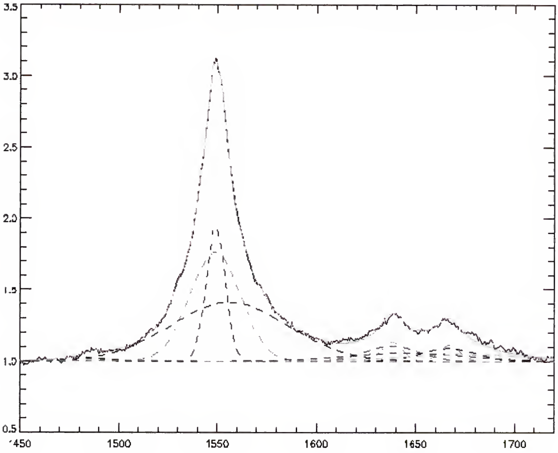

Figure C–6 An example of a multiple Gaussian fit to the wavelength range 1450–1720 Å of a normalized composite spectrum. C IV is fit with three Gaussian profiles, and N IV], He II, and O III] are all fit with C IV profiles. The plot has been exported using the Screenshot .PS option in the Export menu.

You can fit absorption lines using the “Absorp Fit” button (v4.0+). This is similar to the multiple Gaussian fit discussed above. You can fit your data with zero or more Gaussian profiles plus zero or more absorption line profiles of the form $I_\lambda = C_f I_0 e^{-\tau_\lambda} + I_0(1 - C_f)$, where $\tau_\lambda = \tau_0 e^{(-\Delta\lambda^2/\Delta\lambda_D^2)}$. Once again, a chi-square minimization routine is used to perform the fit. You can select the ranges of data to be used in the fit as with the Linear Fit (see above). Choose no weighting (uniform) or Poisson weighting ($1.0/Y_i$). If there is a constant offset from 0, you can enter that constant in the Constant box. For instance if you are fitting data that has been normalized to a continuum of 1, you would enter 1 in the Constant box. Initial guesses are mandatory, and there are two methods of inputting them. You can either give it a .gp filename that contains your initial guesses or enter the number of Gaussians and number of absorption lines you wish to fit in the #Gauss box and the #lines box, respectively, and enter the initial guesses of the parameters of each Gaussian and absorption line in the Enter Fit Parameters box. The .gp file should have the following format:

```
number_of_Gaussians
number_of_absorption_lines
flux1           factor tie_to   optional comments
wavelength1     factor tie_to   you can write anything
FWHM1           factor tie_to   you want to out here
flux2           factor tie_to   Note that there are 3 lines per
wavelength2     factor tie_to   Gaussian following the
FWHM2           factor tie_to   number_of_absorption_lines,
...
Tau_0 1         factor tie_to   then there are 5 lines
wavelength1     factor tie_to   per absorption line.
lambda_D 1      factor tie_to
```

```
I_0 1          factor tie_to

C_f 1          factor tie_to

Tau_0 2        factor tie_to

wavelength2    factor tie_to

lambda_D 2     factor tie_to

I_0 2          factor tie_to

C_f 2          factor tie_to

...
```

The wavelength is in whatever scale the x-axis is in, and the FWHMs are in km/s. τ_0 is an optical depth, λ_D is the Doppler broadening, I_0 is the continuum intensity, and C_f is the coverage factor (which ranges from 0 to 1). **It is very important that you have reasonable initial guesses for the fitting routine to properly work.** For free parameters, just enter 0 for both factor and tie_to. To fix a parameter at a particular value (i.e., wavelength has to be 1549.0 and cannot float), enter -1 for factor and 0 for tie_to. To tie a parameter to a constant times the value of another parameter (i.e., FWHM3 = FWHM1 or flux2 = 2*flux1), enter the constant for factor (i.e., 1 or 2 in the examples), and enter the parameter to tie it to for tie_to. This is **not** the Gaussian number, but the parameter number, which starts at 0 for flux1, 1 for wavelength1, 2 for FWHM1, 3 for flux2, 4 for wavelength2, and so on. Remember that the parameter number for τ_0 for the first absorption line will be 3 times the number of Gaussians. τ_0 for each subsequent absorption line will be $n_{Gauss} * 3 + n_{lines} * 5$, where n_{Gauss} is the number of Gaussians and n_{lines} is the number of previous absorption lines. You may find it helpful to keep track of the parameter number in your optional comments space in the file. Below is a sample input file.

```
2

1
```

```
15.0          0      0      param0
1549.0        -1     0      param1 fixed at 1549
3000          0      0      param2
30.0          2.0    0      param3 tied to 2*flux1
1549.0        0      0      param4
3000          1      2      param5 tied to 1*FWHM1
2             0      0      param6 - Absorption line Tau_0
1528          -1     0      param7 - fixed at 1528
5             0      0      param8
19            0      0      param9
0.5           0      0      param10 - C_f
```

Finally, you can tie a parameter to a variable ratio (see multiple Gaussian fit, above). If you want to enter the parameters into the Enter Fit Parameters box, they are entered in the exact same way except that the number of Gaussians and number of absorption lines are left off since they have their own boxes. So the first line in the Enter Fit Parameters box would be the third line of the input file (i.e., parameter number 0, which could be the flux of the first Gaussian or τ_0 for the first absoprtion line, depending on if you are fitting Gaussians in addition to absorption lines or not).

Click Fit to perform the fit and the final fit parameters will be output to the screen. They will also be appended to a .gpfit file. You can optionally specify this filename by entering it in the Output (.gpfit) File text field. If no filename is entered, it defaults to multgaussfit.gpfit in your current directory. A .dat file is also created with the plot data. It is an ASCII file with the format

```
Xi  Total_Fit  Const  Gauss1  ...  GaussN  Line1 ... LineN
```

and thus contains N+M+3 columns for a fit of N Gaussians and M absorption lines. This filename can be specified in the Plot (.dat) File text field. If no filename is entered, it defaults to gpmultgaussfit.dat in your current directory. Your fit is then plotted over your data. Each individual Gaussian and absorption line is plotted in one of five colors, with a dahsed line. The overall fit is then plotted in a solid blue-green line over top of your data. The fit will be done for each file you have in the "Enter Filenames" box, so you can automatically fit multiple files at once as long as you want to use the same range to fit each file and as long as the initial guesses are valid for each file.

The "User Defined Fit" button (v4.0+) allows you to fit any user-defined function to your data using a chi-square minimization routine. You can select the ranges of data to be used in the fit as with the Linear Fit (see above). Choose no weighting (uniform) or Poisson weighting ($1.0/Y_i$). You must give the function a one-word name in the Function name box (GPFIT will automatically generate an IDL procedure based on the function you enter and save it in your current directory). Next, enter the function in terms of X and your parameters. Your parameters must be represented by A[0], A[1], A[2], and so on. For example, to fit the function $a\ sin(bX) + c$ to your data (finding values for a, b, and c), you would type: A[0]*sin(A[1]*X)+A[2] where A[0]=a, A[1]=b, and A[2]=c. Next, you must give partial derivatives with respect to each parameter as functions of X so that IDL can use its chi-square minimization routine. For the above example, you would enter sin(A[1]*X), A[0]*X*sin(A[1]*X), and (X>1)/(X>1), respectively. Note that the derivative with respect to A[2] is 1, but IDL needs numeric partial derivatives for the entire array, so the derivative needs an array of the same length as X with each value set to 1. An easy way to do this is of course to set it to X/X which is by definition 1, but you might run into a division by zero error. Thus, (X>1)/(X>1) is a simple way to represent an array of the proper length in which every element is 1 without creating any errors. It is mandatory to enter initial guesses for your parameters, one per line. See Figure C-7 shows the above example.

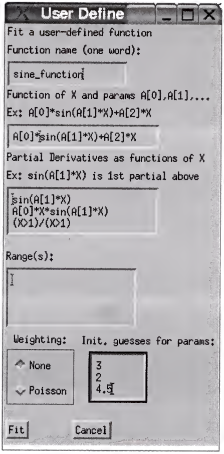

Fit a user-defined function

Function name (one word):

sine_function

Function of X and params A[0],A[1],...

Ex: A[0]*sin(A[1]*X)+A[2]*X

A[0]*sin(A[1]*X)+A[2]*X

Partial Derivatives as functions of X

Ex: sin(A[1]*X) is 1st partial above

```
sin(A[1]*X)
A[0]*X*sin(A[1]*X)
(X>1)/(X>1)
```

Range(s):

Weighting: ● None ○ Poisson

Init. guesses for params:

```
3
2
4.5
```

Figure C–7 An example of a user-defined fit of the function $Y = a\ sin(bX) + c$.

Click Fit to perform the fit. The results will be output to the screen and appended to a file udfit.gp in your current directory. A dotted line showing the fit will also be plotted on top of your data. The fit will be done for each file you have in the "Enter Filenames" box, so you can automatically fit multiple files at once as long as you want to use the same function and range to fit each file.

C.6 Commands, Images, and More

The "Exec Command" button (v4.0+) brings up a box that allows you to enter IDL and/or GPScript code to be executed immediately. Click Execute to execute the code or Exit to close the window without executing any code. The code can be as simple as the statement print,"Hello." or as complicated or moreso than the following program.

```
openr,5,'files.txt'
f=''
for j=0,4 do begin
   readf,5,f
   gpsload,f
   a=gpsDataAt(1442) AND gpsDataAt(1712) AND gpsDataAt(1549)
   if a then gpsfwhm,1442,1712,xpeak=1549,out='FWHM.dat'
endfor
close,5
```

Almost anything you can write in a program can be written here (although its doubtful you'll want to use this to write anything much longer than the above example, as it would be better to put anything long in its own file and execute it normally as either an IDL program or with GPScript).

GatorPlot also suports JPEG and FITS images. Click the "Images" button (v4.0+) to bring up the Image Menu which contains seven buttons: Load Image, New Window, Intensity, Export, Erase, Negative, and Cancel. The Image Menu will stay open until you click Cancel, which closes the menu and sends you back to the main GatorPlot. Load Image predictably loads an image. You can choose to load the image into either a new window that IDL will automatically size to fit the entire image, or into an existing window (created by either loading a previous image or with New Window). You can specify an X and Y position in pixels from the lower left hand corner of the window for the lower left hand corner of the image. By using this in an existing window, smaller images can be combined into larger images. In addition to Load and Cancel, there is a Get Info button, which, when clicked, will display on your screen the X and Y dimensions of the image and whether it is greyscale or true color. This can be useful when combining images of unknown sizes into a larger image because it allows you to determine the image size before entering the position to display the image at in the window. New Window allows you to open a window of a custom X and Y size. For instance, if you wanted to combine four 80x80 images into one 4-panel 160x160 image, you would use New Window to open a 160x160 image, then Load all 4 images into the existing window with the proper X and Y position for each image. Intensity can only be used after an Image has been loaded. Clicking it brings up a window that has boxes labeled X, Y, R/gs, G, and B as well as a Cancel button that will close the window. Mouse over the image and X and Y will display the (X,Y) coordinate the mouse is over. If it is a greyscale image, the intensity (0-255) will be displayed in the R/gs box. If it is a true color image, then the R, G, and B intensities will all be displayed in the corresponding boxes. Erase erases the current open window. Negative takes a negative of the current image. Export allows you to export the image as a JPEG, FITS, Postscript, to the printer, or as a PDF in either greyscale or color. Enter a filename and select the file type, and color or greyscale. If you want to export as an encapsulated postscript, simply select postscript, but make sure your filename ends in .eps. Note that the Printer and PDF options only work on Unix and Linux systems.

The “Resample” button (v4.4) allows you to resample your data in various ways. You can enter a redshift to convert an observed spectrum to its rest-frame wavelengths. For instance, entering a redshift of 2 would cause the x-axis of the spectrum to be divided by 3. You can change the step size between pixels and the start and end wavelengths as well. The modified data can be plotted or saved as an ASCII or FITS file.

You can draw a line anywhere in the plot window using the “Draw” button (v4.4). Enter the X and Y coordinates of the two endpoints of the line either manually or by left-clicking on one point and right-clicking on the other. A color can optionally be specified as an RGB triple separated by spaces. A linestyle can also be specified (see below).

C.7 Default Columns, Colors, and Linestyles

Beginning in v3.0, you can enter default column numbers for the x and y-axis data to be read from ASCII files. This is the same column you would normally enter in the popup dialogue box prompting you for X-axis column and Y-axis column when you plot an ASCII file. But if entered here, the popup box does not appear and gatorplot reads the column numbers from here instead. This saves time if you are plotting a file several times. GatorPlot will attempt to automatically detect any header the file may have and skip over it to get to the data.

In the Colors text area (v3.0+), you can optionally enter a color for each file to be plotted with. Colors can be entered in one of two ways. If your display is set to true color, you can enter the R, G, and B values (delimited by spaces) of the color you want to be plotted. For instance, 0 255 255 would produce a bright blue-green color or 255 160 0 would produce orange. R, G, and B values range from 0 to 255 each. If you would rather manually enter a color index yourself, you can do that instead. This can be used if you have 8-bit color or a color table already loaded (or if you have true color and are just adventerous). Enter for example 210 (or if you have true color try 3921453). If no color value is entered, it defaults to white on the screen and black in .PS files.

In the Line text area (v3.0+), you can optionally enter a linestyle for each file to be plotted with. Valid linestyles range from 0–5 and correspond to solid, dotted, dashed, dash dot, dash dot dot, and long dashes respectively. If left blank, it will default to solid lines if you are creating a stacked plot or the default linestyle corresponding to the file number for overplots.

C.8 More Options

Under the plot window are various other options that can be specified. Use the x-range and y-range text areas to specify the range you wish to view. Leave them blank for the default behavior of displaying the entire dataset. The Y-axis ticks button toggles between On and Off. Turn this off when creating a stacked plot if you don't want meaningless tick marks running all the way up the y-axis. Instead, there will only be tick marks at the "zero" level and, if specified, the level of each dotted line for the plot.

The CharSize text field allows you to set the character size. The default value is 1. Entering 2 would cause all characters to be twice as big and similarly entering 0.5 would cause all characters to be half the normal size. The "Dotted line at y=" text field allows you to overplot a dotted line at any specific y-value (for instance a continuum at y=1 if plotting a spectrum that has been normalized to a continuum level of 1). The "Cutoff at y=" text field allows you to cut off all data above this level for each plot. This can be useful when creating a stacked plot. For example, if you are plotting spectra that contain a strong emission line, use this to cut off the values above a certain level and zoom in on the details of weaker emission lines. This allows you to put a smaller offset between the plots and the smaller range shows more detail. The Stacked and Overplot buttons toggle the plotting behavior between stacking plots on top of each other and plotting multiple files directly over each other. The default behavior is Stacked and creates a plot where the files are stacked above each other with a y-axis offset for each. Click Overplot to plot the data directly on top of each other with the same "zero" level for all of the plots. If you choose Overplot, different linestyles will be used for the different files: solid for the first file, dotted for the second, dashed, dash dot, dash dot dot, and long dashes for the 6th file. If there are still more files, the pattern then repeats with the 7th being solid and so on.

Click the "Add Text" button to add text anywhere in the plot. It brings up a window prompting for X and Y coordinates, the text, character size, alignment, orientation, and color. If adding text to a plot on the screen, clicking on the screen will automatically fill in the X and Y coordinates for you. Alignment ranges from the default value of 0.0 (text begins at specified point) to 1.0 (text ends at specified point) and Orientation is from 0 to 360 degrees. Note that when adding text to a Postscript, or PDF file or a plot being sent to the printer, you are not able to click on the screen to obtain the X and Y coordinates because you are plotting to a different device. The easiest way to add text to these plots would be to first plot to the screen, then click everywhere you want to add text, and those coordinates will be printed out in the IDL window. Then export to the file, click "Don't Finalize", and add the text, typing in the coordinates that were printed out in the IDL window. Then click "Finalize" when you are done. Alternatively, beginning in v3.0, you can add text to the plot on the screen and then export the plot using Screenshot .PS, Print Screenshot, or Screenshot PDF.

If you are exporting a plot to a Postscript or PDF file or sending it to a printer and you clicked "Don't Finalize" from the export menu, click the "Finalize" button after you are done adding text to the plot to close the file or send it to the printer.

The X-axis and Y-axis buttons allow you to toggle each axis between linear and logarithmic. The "More Options" button (v2.0+) allows you to set more IDL plot options, including Position, XYMargin, XYMinor, XYtickinterval, XYticklayout, XYticks, XYtickname, and XYtickv. See the IDL documentation for an explaination of what each of these options does.

Click the "Multiplot" button (v2.0+) to create a plot with multiple panels in one window. Set the number of rows and columns and specify auto or manual. In auto mode, each file or function in your file list is automatically plotted in its own panel. For instance if you have 4 files entered and you want to create a 4-panel plot with 2 rows and 2 columns and have each file plotted, select 2 rows, 2 colums, and auto, click Apply, then click either Plot or Export. If you want to plot more than one file or function per panel, use manual mode. In manual mode, each time you click Plot, another panel is added with the files currently listed plotted just as they would normally be except within a panel. When exporting in manual mode to a Postscript or .PDF file or the printer, click Export after you set your Multiplot options, and enter the file info. But do not finalize if you have more panels to add. Add any text you want to this first window now, as this is your only chance (this applies to just plotting as well as exporting). Starting with the second plot, click Plot instead of export as you already entered a filename (or selected the printer). When finished, click Finalize at the bottom. To export to a JPEG, select Export–JPEG at any time and the current contents of the screen will be exported to a JPEG file. The same goes for the exporting options Screenshot .PS, Print Screenshot, and Screenshot PDF.

Clicking the "Help" button (v2.0+) enables the online help. A help file similar to this appendix is printed to your current terminal window, 23 lines at a time. Pressing the space bar goes to the next page, and pressing 'q' quits help. Beginning with v3.01, if you have correctly configured your web browser of choice using gatorplot_config, clicking help will open a browser window displaying the help file in HTML. Finally, the UF button is a little gadget added to make GatorPlot more Gator friendly.

C.9 GPScript

GPScript is a systemwide scripting language (implemented in v4.0) that can be used to automatically do almost anything that can be done interactively in GatorPlot. The procedures and functions of GPScript are an extension of IDL, so your scripts may contain any combination of IDL and GPScript functions/procedures. To run a script, at an IDL prompt, enter: gatorplot,script='scriptname', where scriptname is the name of the file that contains the script. The script should be set up as and IDL procedure. Note that the file must be in your IDL_PATH or your current directory so that IDL can see it since it will not be precompiled. Also, the filename must match the name of the procedure. For instance, you could have script called data in a file named data.pro:

```
pro data
gpsload,'file.fits'
print,gpsDataAt(1549)
end
```

This simple script could be run by entering: gatorplot,script='data' at an IDL prompt. Below is a list of all GPScript functions/procedures, their calling sequences, and some examples.

- gpsload: Loads a file or several files into memory.

  `gpsload, files[, xcol=, ycol=, funmin=, funmax=, funpts=]`

  files is a string or string array containing one or more filenames or functions. The files can be either FITS or ASCII or you can enter a function just as you would in the Enter Filenames box in GatorPlot. The optional xcol and ycol keywords specify the columns in the ASCII file to read X and Y data from. The optional funmin, funmax, and funpts keywords specify the minimum and maximum X-values to be used in generating the function and the number of points to be used for the function. xcol and ycol are mandatory if loading an ASCII file, as are funmin, funmax, and funpts if loading a function.

  Examples:

  ```
  gpsload,['file1.fits','file2.dat'],xcol=1,ycol=3
  gpsload,'f(x)=sin(x)',funmin=0,funmax=6.28,funpts=100
  ```

- gpsmultiplot: Use this to setup a multi-panel plot.

  `gpsmultiplot, rows, cols [, /auto]`

rows and cols are the number of rows and columns in the multipanel plot. If auto is not set, then all files currently loaded will be plotted (either stacked or overplotted) in one panel of the multi-panel plot each time gpsplot is called. If the optional keyword auto is set, then each file currently loaded will be plotted in its own separate panel. Examples:

```
gpsmultiplot,2,2
gpsmultiplot,3,2,/auto
```

- gpsplot: Plot currently loaded files to the screen. If a multi-panel plot is desired, gpsmultiplot should be called first. gpsplot must be called before exporting any plots.

  ```
  gpsplot, [xmin=, xmax=, ymin=, ymax=, xtitle=, ytitle=, title=,
  /xlog, /ylog, /overplot, charsize=, linestyle=, color=, psym=,
  offset=, label=, xmargin=, ymargin=]
  ```

  In its simplest form, you can just call gpsplot without any keywords. The optional keywords xmin, xmax, ymin, and ymax of course allow you to specify the X and Y ranges to be displayed. xtitle, ytitle, and title allow you to enter strings that will be used as axis or plot titles. Specifying /xlog or /ylog makes that axis logarithmic instead of linear. Specifying /overplot causes files to be plotted over one another in the case that more than one file is plotted in a panel (or window). By default, the files will be shown stacked on top of each other. charsize sets the character size (default = 1), linestyle the linestyle (0-5, see IDL help), and psym the plotting symbol (again, see IDL help). color can be specified by either a string containing a single number for color index (e.g., color='1019') or as an RGB triple as in the GatorPlot GUI (e.g., color = '0 255 255' for blue-green). offset takes an array argument of length up to files-1 and overrides the default offset when displaying a stacked plot (e.g., if you have three files loaded, to be displayed in a stacked plot, off=[2,5] would set the zero-level for file 2 at 2 and for file 3 at 5). label takes a string array as an argument and will label each data set on the right side of the display (e.g., label = ['File 1', 'File 2', 'File 3']). Finally, xmargin and ymargin each take vectors of length two and perform the same task as the xmargin and ymargin keywords in the IDL PLOT procedure. Examples:

```
gpsplot,xmin=1450,xmax=1720,ymax=5, xtitle='Wavelength',ytitle='Flux',
charsize=1.5, color='255 0 0'
gpsplot,title='Stacked Spectra',/xlog, linestyle=[0,1,2],
color=['255 0 0', '0 255 0', '0 0 255'], offset=[2,5], label=['File
1', 'File 2', 'File 3']
```

- gpsexport: Export plots that have been created with gpsplot. Plots can be exported to Postscript, JPEG, PDF files, the printer, or the data can be exported to a FITS or ASCII file.

  ```
  gpsexport, filename [, /printer, /color, /landscape, /multiplot,
  xsize=, ysize=]
  ```

  filename is the export file to contain the plot/data. The file type is automatically determined by the file extension (.jpg or .jpeg = JPEG file, .fit or .fits = FITS file, .ps or .eps = Postscript, .pdf = PDF, .dat or .txt = ASCII). Specify the /printer keyword to send the plot to the printer (UNIX/Linux only). Specify /color to export as true color instead of the default greyscale. Specify /landscape to export in landscape instead of portrait mode. Specifying /multiplot makes GPScript check if all panels have been created and only exports if they all have (e.g., if you're doing a 9-panel, 3x3 plot but you call gpsexport after only plotting 7 files and specify /multiplot, then nothing will happen. If you call it again after plotting all 9 files, again specifying /multiplot, then the plot will be exported. If you don't specify /multiplot then GPScript exports without checking.) xsize and ysize can be set to the X and Y size of the Postscript, PDF, or printer file in inches. Again, using a .eps extension causes the plot to be exported to an encapsulated postscript file. Examples:

```
gpsexport,'image.jpg',/color
gpsexport,'figure.eps',xsize=7,ysize=9
gpsexport,/printer
```

- gpssmooth: Apply smoothing to loaded data.

  ```
  gpssmooth [, /boxcar, /binomial, npts=# of points, iter=#
  iterations]
  ```

  See Smoothing (above) for more details. If not specified, npts defaults to 5 and iter to 1. Example:

  ```
  gpssmooth, /boxcar, npts=3
  ```

- gpsmath: Perform arithmatic operations on data.

  ```
  gpsmath, files1 [, factor1=,const1=,oper=,files2=,factor2=,const2=,out=]
  ```

  filelist1 is an intarr containing the index of each file (starting with 0) to include in the arithmatic operation. factor1 is an intarr containing the factor to scale each corresponding dataset by eg. a0*x0+a1*x1+... const1 is a constant number to be added to this. oper can be '+', '-', '*', or '/'. files2 is an intarr similar to files1, with factor2 and const2 corresponding to factor1 and const1. Finally, out is a string containing a filename for the data to be written to after the arithmatic is performed. If the filename ends in '.fits' or '.fit', the data will be written as a FITS file, otherwise it will be written as an ASCII file. So there are many possible combinations of operations that can be performed by gpsmath: (a0*x0+a1*x1+a2*x2+...+c1) +, -, * , or / (b0*x0+b1*x1+b2*x2+...+c2) Examples:

  ```
  gpsload,['a1.dat','a2.dat','a3.dat','a4.dat'] ;load 4 files
  ```

```
gpsmath, [0,1], factor1=[1,2], const1=2, out='test.fits'
```

writes a FITS file with the result of a1.dat + 2*a2.dat + 2.

```
gpsmath, [0,3], const1=1, oper='/', files2=[1], factor2=[2],
out='test.dat'
```

writes an ASCII file with (a1.dat + a3.dat + 1) / (2*a2.dat).

- gpsintegrate: Integrate over a user-defined baseline (see Integrate above).

  ```
  gpsintegrate, x1, x2 [,y1, y2 , out=]
  ```

  x1, x2, y1, and y2 are the X and Y coordinates of the start and end of the user-defined baseline Leaving off the y-values results in them being set to 0. out specifies a file to output the results to. If no file is specified, it defaults to gpsintegrate.dat. Examples:

  ```
  gpsintegrate, 1500, 1600, out='results.dat'
  ```

  integrates over a line drawn from (1500,0) to (1600,0) and outputs results to results.dat.

  ```
  gpsintegrate, 1500, 1600, 0.5, 1.5
  ```

  integrates over a line drawn from (1500,0.5) to (1600, 1.5) and outputs results to gpsintegrate.dat. gpsintegrate can also be used as a function:

  ```
  result = gpsintegrate(x1, x2 [,y1, y2, out=])
  ```

  When used as a function, the result returned is a string containing 4 space-delimited columns: the integration (flux), center, equivalent width, and filename. If more than one file is loaded when gpsintegrate is called, result returns as a string arrray with one element for each file. Example:

  ```
  flux=strparse(gpsintegrate(1500,1600,1,1),1)+0.
  ```

- gpsfwhm: Estimate the FWHM of an emission/absorption line without fitting (see FWHM above).

  ```
  gpsfwhm, contin_x1, contin_x2 [, xpeak=, ypeak=, out=]
  ```

contin_x1 and contin_x2 are the x-coordinates of two continuum points, one on each side of the line. xpeak and ypeak allow you to optionally specify the X and/or Y coordinates of the peak/trough of the line. If you do not specify these, they will be automatically calculated. out specifies an output file for the results (defaults to gpsfwhm.dat). Examples:

```
gpsfwhm, 1442, 1712
gpsfwhm, 1442, 1712, xpeak=1549, out=’civ_fwhm.dat’
```

Like gpsintegrate, gpsfwhm can also be used as a function:

```
result = gpsfwhm(contin_x1, contin_x2 [, xpeak=, ypeak=, out=])
```

When used as a function, the result returned is a string containing 4 space-delimited columns: the FWHM in x-axis units, FWHM in km/s, center, and filename. If more than one file is loaded when gpsfwhm is called, result returns as a string arrray with one element for each file. Example:

```
fwhm=strparse(gpsfwhm(1450,1720),2)+0.
```

- gpslinfit: Linear fit to data (see GPFIT: Linear Fit).

  ```
  gpslinfit [, range=, /poission, out=, plotps=, plotxrange=]
  ```

  range is a string array representing the ranges in the data to be included in the fit. It is entered just as you would enter in in the Range box in GPFIT (i.e. ['1825 1850’, ’2000 2025’] would mean fit using data from 1825–1850 and 2000–2025). Leaving off range makes the range all X's. The /poisson option sets poisson errors. out specifies the output file for the fit parameters (default linfit.gp). plotps specifies a filename to plot (in postscript) the data and the fit. If no filename is specified, the plot is not created. plotxrange allows you to specify the x-range for the postscript plot. Example:

  ```
  gpslinfit, range=[’1825 1850’, ’2000 2025’], /poisson, plotps=’fit.ps’
  ```

- gpsplawfit: Powerlaw fit to data (see GPFIT: Powerlaw Fit).

  ```
  gpsplawfit [, range=, /poisson, coeff=, out=, plotps=, plotxrange=]
  ```

range is a string array (see gpslinfit) and /poisson sets poisson weighting. gpfcoeff takes your initial guesses for the coefficients of aX^b in the order [a,b]. out, plotps, and plotxrange as described in gpslinfit. out defaults to plawfit.gp if not specified. Example:

```
gpsplawfit, range=['1440 1460', '2000 2025'], /poisson, coeff=[700,
-0.8]
```

gpsplawfit may be called as a function as well:

```
result = gpsplawfit([range=, /poisson, coeff=, out=, plotps=,
plotxrange=])
```

When used as a function, the result returned is a two-element array containing the coefficients in the order [a,b].

- gpsmgfit: Multiple Gaussians fit to data (see GPFIT: Multiple Gaussian Fit).

  ```
  gpsmgfit in= [,range=,/poisson,const=,out=,plotfile=,plotps=,plotxrange=
  ```

  in specifies the input file containing the fit parameters (as described in GPFIT: Multiple Gaussian Fit). range, poisson, out, plotps, and plotxrange as described above. out defaults to multgaussfit.gpfit. const is a constant offset from 0 (e.g., normalized continuum level). plotfile specifies a filename to receive the plotfile containing the data, overall fit, and value of each Gaussian at every X-value. It defaults to gpmultgaussfit.dat. Example:

  ```
  gpsmgfit, range=['1510 1680'], in='civ.gp', const=1, plotps='civfit.ps'
  ```

- gpspolyfit: Polynomial fit to data (see GPFIT: Polynomial Fit).

  ```
  gpspolyfit order= [, range, /poission, coeff=, out=, plotps=,
  plotxrange=]
  ```

  order specifies the order of the Polynomial to be fit (e.g., 2 = quadratic, 3 = cubic). range, poisson, out, plotps, and plotxrange as described above. out defaults to polyfit.gp. coeff is an array containing optional initial guesses at the polynomial coefficients of $a_0 + a_1X + ... + a_nX^n$ in the order [a_0, a_1, ..., a_n]. Example:

```
gpspolyfit, order=3, coeff=[3, 0, -2, 1], out='poly.dat'
```

- gpsabsfit: Fit Absorption Lines (see GPFIT: Absorption Line Fit).

  ```
  gpsabsfit, in= [,range=,/poisson,const=,out=,plotfile=,plotps=,
  plotxrange=]
  ```

  in specifies the input file containing the fit parameters (as described in GPFIT: Absorption Line Fit). Everything else as described in gpsmgfit. out defaults to multabsfit.gpfit and plotfile defaults to gpmultabsfit.dat. Example:

  ```
  gpsabsfit, range=['1470 1600'], in='absparams.dat', const=19,
  plotps='abs.ps'
  ```

- gpsudfit: Fit User-Defined Function (see GPFIT: User-Defined Fit).

  ```
  gpsudfit, name, f=, pders=, coeff= [,range=,/poisson,out=,plotps=,
  plotxrange=]
  ```

  name specifies the name of the user-defined function for purposes of generating it (one word). f gives the function as a String in terms of X and parameters A[0], A[1], ... (e.g. A[0]*sin(A[1]*X)+A[2]). pders is a String array containing the partial derivatives with respect to each parameter (e.g. df/dA[0], df/dA[1], ...). coeff gives the initial guesses for each parameter. range, poisson, out, plotps, and plotxrange as described above. out defaults to udfit.gp. Example:

  ```
  gpsudfit, 'sinefit', f='A[0]*sin(A[1]*X)', pders=['sin(A[1]*X)',
  'A[0]*X*sin(A[1]*X)'], coeff=[4, 2], plotps='sine.ps'
  ```

- gpsDataAt: Checks if there is non-zero data at a specified X-value and returns 1 (true) or 0 (false).

  ```
  result = gpsDataAt(x)
  ```

  Examples:

```
print, gpsDataAt(1549)
```

```
if gpsDataAt(1549) then print,'There is data at 1549.'
```

```
a = gpsDataAt(1549)
```

- gpsMean: Returns the mean value of all data in a specified range.

  ```
  result = gpsMean(w1, w2)
  ```

  w1 and w2 are the X-values used to determine the range. Examples:

  ```
  print, gpsMean(1440, 1460)
  ```

  returns the mean value of the data in the 1440–1460 interval.

  ```
  if gpsDataAt(1450) then a=gpsMean(1440, 1460)
  ```

- gpsMedian: Returns the median value of all data in a specified range.

  ```
  result = gpsMedian(w1, w2)
  ```

  Example:

  ```
  print, gpsMedian(1440, 1460)
  ```

- gpsStdDev: Returns the standard deviation of all data in a specified range.

  ```
  result = gpsStdDev(w1, w2)
  ```

  Example:

  ```
  s = gpsStdDev(1440, 1460)
  ```

- gpsMax: Returns the maximum value in a specified range.

  ```
  result = gpsMax(w1, w2)
  ```

  Example:

  ```
  m = gpsMax(1500, 1600)
  ```

- gpsWhereMax: Returns the corresponding X-value to the maximum value in a specified range.

  ```
  result = gpsWhereMax(w1, w2)
  ```

  Example:

  ```
  x = gpsWhereMax(1500, 1600)
  ```

- gpsMin: Returns the minimum value in a specified range.

```
result = gpsMin(w1, w2)
```

Example:

```
m = gpsMin(1500, 1600)
```

- gpsWhereMin: Returns the corresponding X-value to the minimum value in a specified range.

  ```
  result = gpsWhereMin(w1, w2)
  ```

  Example:

  ```
  x = gpsWhereMin(1500, 1600)
  ```

- gpsloadimg: Loads an image into memory.

  ```
  gpsloadimg, filename
  ```

  filename is either a JPEG or FITS image. Example:

  ```
  gpsloadimg, 'picture.jpg'
  ```

- gpsexportimg: Exports a previously loaded image to JPEG, FITS, Postscript/.eps, PDF, or the printer.

  ```
  gpsexportimg, filename [, /printer]
  ```

  The file-type is automatically determined by the ending (.jpg/.jpeg, .fit/.fits, .ps/.eps, or .pdf). Specifying the printer keyword sends the image to the printer (UNIX/Linux only). Examples:

  ```
  gpsexportimg, 'picture.ps'
  gpsexportimg, /printer
  ```

- gpsnegative: Takes the negative of a previously loaded image.

  ```
  gpsnegative
  ```

- gpsIntensityAt: returns the intensity of a given pixel in an image.

  ```
  result = gpsIntensityAt(x, y)
  ```

  x and y are the x and y coordinates of the desired pixel. result returns as a number between 0 and 255 for greyscale images or a 3-element array representing the R, G, and B intensities as 3 numbers between 0 and 255 for a true color image. Example:

```
a = gpsIntensityAt(50, 100)
```

- gpsexecom: Brings up a window that allows you to enter IDL and/or GPScript code to be executed immediately. See “Exec Command” button above.

  ```
  gpsexecom
  ```

- gpsresample: allows you to resample your data in various ways (see the “Resample” button above).

  `gpsresample [, z=, step=, xmin=, xmax=, outf=]` z is the redshift, step is the stepsize between pixels, and xmin and xmax are the start and end x-axis values. outf is an output file that can be either FITS or ASCII. If the filename entered ends in ’.fit’ or ’.fits’, then it will be a FITS file. Otherwise, it will be an ASCII file. Example:

  ```
  gpsresample, z=1.5, step=0.5, outf='resampled.dat'
  ```

- gpsdrawline: draws a line anywhere in the current plot (see the “Draw” button above).

  ```
  gpsdrawline, X1, X2, Y1, Y2 [,color=, linestyle=]
  ```

  X1, X2, Y1, and Y2 are the X and Y coordinates of the two endpoints of the line. color can be a number or a string with space-delimited RGB values of a color. linestyle can be from 0 to 5. Example:

  ```
  gpsdrawline, 1549, 1549, 3, 5, color='255 0 0', linestyle=1
  ```

- strparse: While technically not a part of GPScript, the strparse function is used by several procedures in GatorPlot and GPScript and is thus included with GatorPlot. strparse allows you to parse a string delimited by whitespace (tabs or spaces).

  ```
  result = strparse(string, column)
  ```

string is any string and column is the column number you want to extract.

Examples:

```
s = 'column1 5 3 6 column5'
```

```
print,strparse(s,1)
```

prints 'column1' to the screen.

```
b = strparse(s,2)+0.*strparse(s,4)+0.
```

stores 30 (5*6) in the variable b.

- get_color: Also not technically a part of GPScript, but included with GatorPlot, get_color converts an RGB triple into a number between 0 and 2^{24} that IDL uses to represent that color.

  ```
  result = get_color(r, g, b)
  ```

  r, g, and b are all integers between 0 and 255. Examples:

  ```
  a = get_color(255, 112, 0)
  ```

  ```
  plot, x, y, color=get_color(0, 255, 255)
  ```

APPENDIX D
DETAILS OF CREATING COMPOSITE SPECTRA

The following is a step-by-step guide to creating, manipulating, and fitting composite spectra.

1) Our sample contains AGN spectra in both FITS format and gzipped ASCII files. The spectra have already been transformed to rest-frame wavelengths and conform to a uniform flux scale and wavelength range. Flux and wavelength calibrations have been applied, as well as an interstellar extinction correction and a K-correction.

2) We have several plain text data files containing various information about each AGN, including its filename, redshift, luminosity, FWHM(C IV), SMBH mass, and L/L_{edd}. These files can be used to sort the AGNs by various criteria and select objects for a composite spectrum.

3) I begin by creating a new directory for each composite or group of composites. Among the items that should be included in this directory are the data files mentioned above, programs to sort the AGNs, the calctemplate program (see below), and several subdirectories. I generally create subdirectories named input, test, output, and GatorPlot.

4) I create a list of all spectra to be included in each composite. I use a program to sort the AGNs by my chosen criteria and create two output files: input/file and input/file.list. The first file should be an executable that copies the gzipped ASCII versions of the spectra into the subdirectory test. The second file (input/file.list) should contain the filename of each spectrum to be included in the composite (i.e., test/file.dat).

5) I change directories into test and gunzip all the files. All of the spectra to be included in the composite are now in ASCII format in the subdirectory test, and are listed in the file input/file.list.

6) I change back up a directory (from test) and run the calctemplate program written by Matthias Dietrich. When prompted, I enter 1 for interactive mode and 3 for absorption-line filter. I next enter the file containing the input filenames (input/file.list) and an output filename (i.e., output/file.dat). I enter 1 for the number of iterations and 3 for x-times rms as the threshold for the absorption-line filter. After calctemplate finishes running, the file output/file.dat is a 14,000 line, 5-column ASCII file. The first three columns contain the number of objects contributing at each wavelength, the wavelength, and the mean flux.

7) I convert the ASCII file to a FITS file. This can be done in several ways. First, GatorPlot can be used simply by selecting the ASCII file and choosing to export as a FITS file. Secondly, it can be done using GPScript, GatorPlot's scripting language. A script can be written that uses the procedures gpsload and gpsexport to automatically convert several files in batch mode. Finally, one can write a custom program to convert the files.

8) I copy the new FITS files into the GatorPlot subdirectory.

9) Before performing the iron subtraction, I must determine which iron emission template to use. There are iron templates for every 500 km s^{-1} in emission line FWHM. I use GatorPlot's FWHM button to estimate the FWHM of C IV in the composite spectrum. I left-click the mouse at the left continuum point, drag the mouse to the right continuum point, release the mouse button, then click the Compute button. I round the FWHM to the nearest 500 km s^{-1}, choose which iron emission template to use, and copy it over to the GatorPlot subdirectory.

10) I use GatorPlot to perform the iron subtraction. Using the Browse button, I select both the composite and the Fe II template and plot them both. I use the

Integrate button to determine the total flux between 1440 Å and 1460 Å in both spectra: I click the Integrate button and enter 1440, 1460, 0, and 0 as X1, X2, Y1, and Y2, respectively. Integrate sums the total flux above a user-defined baseline (in this case zero). Since the strength of the iron emission lines should be equal to ~ 2–3% of the total flux in this wavelength range, I scale the template so that its flux equals 2% of the flux of the composite spectrum between 1440 Å and 1460 Å. With both the composite and the template still listed in the filenames box in GatorPlot, I click the Maths button. In the top file box, I then select the composite spectrum and select "-" as the operation. I select the template in the bottom file box and enter a factor to scale it by in the "Scale By" box. I next click the Save button, select FITS as the file type, and enter a filename.

11) I next fit the continuum with a powerlaw. I erase everything from the filenames box in GatorPlot and use the Browse button to select the iron-subtracted composite spectrum I just created. I plot this spectrum and select the wavelength ranges to be used to anchor the continuum fit. Generally I use wavelength intervals centered at 1450 Å, 1990 Å, and when possible 1720 Å or 1780 Å. I always zoom in on these regions of the spectrum and look at them carefully before deciding exactly which wavelength ranges to use. Once I have decided on the wavelength ranges to anchor the fit, I set my x-axis range to 900–2100 Å and my y-axis range to 0–2 in order to get a close look at how good the continuum fit is. I then click the Plaw Fit button. I enter the wavelength ranges in the Range(s) box in a two-column format, select either no weighting or Poisson weighting, and optionally enter an initial guess for the exponent of the powerlaw. The powerlaw is of the form $Y = bX^a$. An initial guess can be given for a without a guess for b (or vice-versa). The fit will be plotted as a dashed line on the screen and the function will be printed out in the terminal window. If the fit does not look good enough, I will vary the initial guesses, weighting options, and wavelength ranges and try again.

12) Once I have a good fit to the continuum, I will divide my spectrum by that fit, normalizing the continuum to unity. I reset the x-axis and y-axis ranges and underneath the composite's filename in the filenames box, I enter the continuum fit as a function of x (i.e., "f(x)=9883.13 * xˆ (-1.26655)"). I select the Overplot button in the bottom right corner of the GUI and click the Plot button. When prompted for Xmin, Xmax, and number of points, I just click OK and it uses the values from the composite spectrum. The composite spectrum will be plotted as a solid line with the continuum fit overplotted as a dotted line. If the fit still looks good, I next click the Maths button. I select the composite in the top file box, "/" as the operation, and the continuum function in the bottom file box. I click the Save button, select FITS as the file type, and enter a filename.

13) I make a subdirectory in GatorPlot called gpfit to contain all initial guess files, output files, plot files and postscript images of my emission line fits. I create an initial guess file for each region of the spectrum as described in the GatorPlot documentation (see Appendix C).

14) I open the normalized composite spectrum in GatorPlot, select an x-axis and y-axis range, and click the Mult Gauss Fit button. I enter the range or ranges to be used in fitting and enter 1 as the constant (since the continuum is normalized to unity). I select the .gp input file that contains my initial guesses, optionally enter filenames for the output and plot files, and click the Fit button. If the fit looks good, I export the fit as a screenshot .ps file. Otherwise, I go back and vary the initial guesses, fitting range, and weighting options until I obtain a satisfactory fit. This can take a while when dealing with complex blends such as Lyα-N V. I have written routines that use the results of my fit to C IV to generate initial guess files for the Lyα-N V and N III] regions.

15) Once I have satisfactory fits to all of the lines in the spectrum, I total the rest-frame equivalent widths and fluxes from the output .gpfit files. I wrote

programs that read these .gpfit files and automatically calculate the total REW and flux for each emission line.

APPENDIX E
POSTERS

This appendix contains the posters that I have presented at the following conferences: the 201st meeting of the American Astronomical Society (AAS) in Seattle (Figure E-1), the "AGN Physics With the Sloan Digital Sky Survey (SDSS)" conference at Princeton University (Figure E-2), the 203rd meeting of the AAS in Atlanta (Figure E-3), and the 204th meeting of the AAS in Denver (Figure E-4).

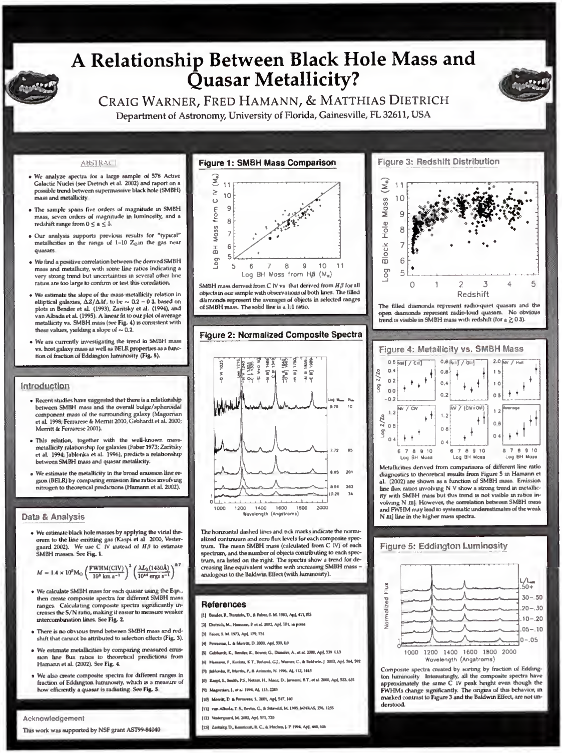

A Relationship Between Black Hole Mass and Quasar Metallicity?

CRAIG WARNER, FRED HAMANN, & MATTHIAS DIETRICH
Department of Astronomy, University of Florida, Gainesville, FL 32611, USA

ABSTRACT

- We analyze spectra for a large sample of 578 Active Galactic Nuclei (see Dietrich et al. 2002) and raport on a possible trend between supermassive black hole (SMBH) mass and metallicity.
- The sample spans five orders of magnitude in SMBH mass, seven orders of magnitude in luminosity, and a redshift range from $0 \leq z \leq 5$.
- Our analysis supports previous results for "typical" metallicities in the ranga of 1–10 $Z_\odot$ in the gas near quasars.
- We find a positive correlation between the derived SMBH mass and metallicity, with some line ratios indicating a very strong trend but uncertainties in several other line ratios are too large to confirm or test this correlation.
- We estimate the slope of the mass-metallicity relation in elliptical galaxies, $\Delta Z/\Delta M$, to be ~ 0.2 – 0.3, based on plots in Bender et al. (1993), Zaritsky et al. (1994), and van Albada et al. (1995). A linear fit to our plot of average metallicity vs. SMBH mass (see **Fig. 4**) is consistent with these values, yielding a slope of ~ 0.2.
- We ara currently investigating the trend in SMBH mass vs. host galaxy mass as well as BELR properties as a function of fraction of Eddington luminosity (**Fig. 5**).

Introduction

- Recent studies have suggested thet there is a relationship between SMBH mass and the overall bulge/spheroidal component mass of the surrounding galaxy (Magorrian et al. 1998, Ferrarese & Merritt 2000, Gebhardt et al. 2000; Merritt & Ferrarese 2001).
- This relation, together with the well-known mass-metallicity ralationship for galaxies (Faber 1973; Zaritsky et al. 1994, Jablonka et al. 1996), predicts a relationship between SMBH mass and quasar metallicity.
- We estimate the metallicity in the broad emission line region (BELR) by comparing emission line ratios involving nitrogen to theoretical predictions (Hamann et al. 2002).

Data & Analysis

- We estimate black hole masses by applying the virial theorem to the line emitting gas (Kaspi et al 2000, Vestergaard 2002). We use C IV instead of $H\beta$ to estimate SMBH masses. See **Fig. 1**.

$$M = 1.4 \times 10^6 M_\odot \left(\frac{\mathrm{FWHM(CIV)}}{10^3\ \mathrm{km\ s^{-1}}}\right)^2 \left(\frac{\lambda L_\lambda(1450\mathrm{\AA})}{10^{44}\ \mathrm{ergs\ s^{-1}}}\right)^{0.7}$$

- We calculate SMBH mass for each quasar using the Eqn., then create composite spectra for different SMBH mass ranges. Calculating composite spectra significantly increases the S/N ratio, making it easier to measure weaker intercombination lines. See **Fig. 2**.
- There is no obvious trend between SMBH mass and redshift that cannot ba attributed to selection effects (**Fig. 3**).
- We estimate metallicities by comparing measured emission line flux ratios to theoretical predictions from Hamann et al. (2002). See **Fig. 4**.
- We also create composite spectra for different ranges in fraction of Eddington luminosity, which is a measure of how efficiently a quasar is radiating. See **Fig. 5**.

Acknowledgement

This work was supported by NSF grant AST99-84040

Figure 1: SMBH Mass Comparison

SMBH mass derived from C IV vs that derived from $H\beta$ for all objects in our sample with observations of both lines. The filled diamonds represent the averages of objects in selected ranges of SMBH mass. The solid line is a 1:1 ratio.

Figure 2: Normalized Composite Spectra

The horizontal dashed lines and tick marks indicate the normalized continuum and zero flux levels for each composite spectrum. The mean SMBH mass (calculated from C IV) of each spectrum, and the number of objects contributing to each spectrum, ara listed on the right. The spectra show a trend for decreasing line equivalent widthe with increasing SMBH mass – analogous to the Baldwin Effect (with luminosity).

References

[1] Bender, R., Burstein, D., & Faber, S. M. 1993, ApJ, 411, 153
[2] Dietrich, M., Hamann, F. et al. 2002, ApJ, 581, in press
[3] Faber, S. M. 1973, ApJ, 179, 731
[4] Ferrarese, L. & Merritt, D. 2000, ApJ, 539, L9
[5] Gebhardt, K., Bender, R., Bower, G., Dressler, A., et al. 2000, ApJ, 539 L13
[6] Hamann, F., Korista, K T., Ferland, G.J., Warner, C., & Baldwin, J 2002, ApJ, 564, 592
[7] Jablonka, P., Martin, P., & Arimoto, N. 1996, AJ, 112, 1415
[8] Kaspi, S., Smith, P.S., Netzer, H., Maoz, D., Jannuzi, B.T., et al. 2000, ApJ, 533, 631
[9] Magorrian, J., et al. 1998, AJ, 115, 2285
[10] Merritt, D & Ferrarese, L. 2001, ApJ, 547, 140
[11] van Albada, T. S., Bertin, G., & Stiavelli, M. 1995 MNRAS, 276, 1255
[12] Vestergaard, M. 2002, ApJ, 571, 733
[13] Zaritsky, D., Kennicutt, R. C., & Huchra, J. P 1994, ApJ, 420, 87

Figure 3: Redshift Distribution

The filled diamonds represent radio-quiet quasars and the open diamonds represent radio-loud quasars. No obvious trend is visible in SMBH mass with redshift (for $z \gtrsim 0.3$).

Figure 4: Metallicity vs. SMBH Mass

Metallicities derived from comparisons of different line ratio diagnostics to theoretical results from Figure 5 in Hamann et al. (2002) are shown as a function of SMBH mass. Emission line flux ratios involving N V show a strong trend in metallicity with SMBH mass but this trend is not visible in ratios involving N III]. However, the correlation between SMBH mass and FWHM may lead to systematic underestimates of the weak N III] line in the higher mass spectra.

Figure 5: Eddington Luminosity

Composite spectra created by sorting by fraction of Eddington luminosity. Interestingly, all the composite spectra have approximately the same C IV peak height even though the FWHMs change significantly. The origins of this behavior, in marked contrast to Figure 3 and the Baldwin Effect, are not understood.

Figure E–1 Poster from the January 2003 AAS meeting in Seattle.

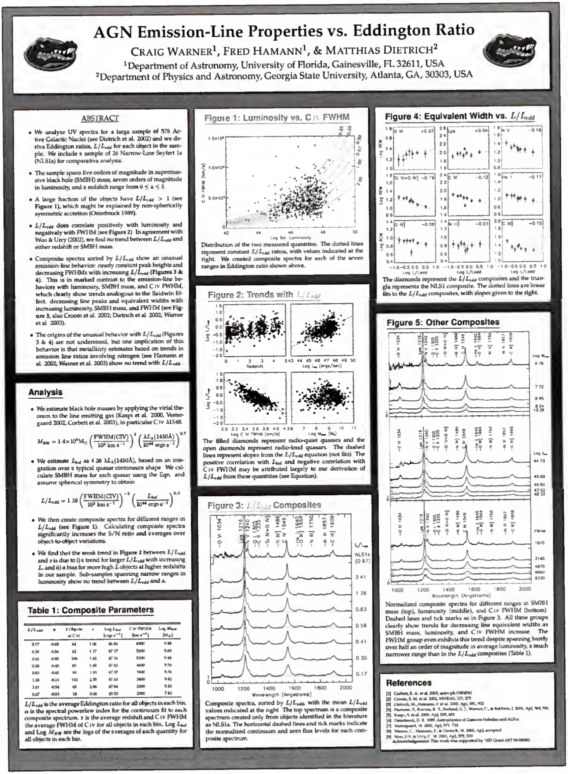
Figure 1: Luminosity vs. C IV FWHM
1.5×10⁴
1.0×10⁴
5.0×10³
0
C IV FWHM (km/s)
42
44
46
48
50
Log Bol Luminosity
0.25
0.33
0.50
0.67
1.00
2.00
Figure 2: Trends with L/L_edd
Log L/L_edd
Redshift
Log L_bol (ergs/sec)
Log C IV FWHM (km/s)
Log M_BH (M_⊙)
Figure 3: L/L_edd Composites
O VI 1034
Lyα 1216
N V 1240
O I 1305
C II 1335
Si IV+O IV]
N IV] 1486
C IV 1549
He II 1640
O III] 1664
N III] 1750
Al III 1857
C III] 1909
L/L_edd
NLS1s (0.67)
3.41
1.38
0.83
0.58
0.41
0.30
0.17
1000
1200
1400
1600
1800
2000
Wavelength (Angstroms)
Figure 4: Equivalent Width vs. L/L_edd
O VI +0.07
Lyα +0.04
N V −0.15
Si IV+O IV] −0.19
C IV −0.12
He II −0.11
O III] −0.08
N III] −0.01
C III] −0.15
Log REW
Log L/Ledd
Figure 5: Other Composites
Log M_BH
8.78
7.72
8.95
8.54
10.28
Log L_bol
44.73
45.69
46.62
47.52
48.32
FWHM
1870
3140
4870
6680
8330
Wavelength (Angstroms)

AGN Emission-Line Properties vs. Eddington Ratio

CRAIG WARNER[1], FRED HAMANN[1], & MATTHIAS DIETRICH[2]
[1]Department of Astronomy, University of Florida, Gainesville, FL 32611, USA
[2]Department of Physics and Astronomy, Georgia State University, Atlanta, GA, 30303, USA

ABSTRACT

- We analyze UV spectra for a large sample of 578 Active Galactic Nuclei (see Dietrich et al. 2002) and we derive Eddington ratios, L/L_{edd} for each object in the sample. We include a sample of 26 Narrow-Line Seyfert 1s (NLS1s) for comparative analysis.
- The sample spans five orders of magnitude in supermassive black hole (SMBH) mass, seven orders of magnitude in luminosity, and a redshift range from $0 \leq z \leq 5$
- A large fraction of the objects have $L/L_{edd} > 1$ (see Figure 1), which might be explained by non-spherically symmetric accretion (Osterbrock 1989).
- L/L_{edd} does correlate positively with luminosity and negatively with FWHM (see Figure 2). In agreement with Woo & Urry (2002), we find no trend between L/L_{edd} and either redshift or SMBH mass.
- Composite spectra sorted by L/L_{edd} show an unusual emission-line behavior: nearly constant peak heights and decreasing FWHMs with increasing L/L_{edd} (Figures 3 & 4). This is in marked contrast to the emission-line behaviors with luminosity, SMBH mass, and C IV FWHM, which clearly show trends analogous to the Baldwin Effect: decreasing line peaks and equivalent widths with increasing luminosity, SMBH mass, and FWHM (see Figure 5, also Croom et al. 2002; Dietrich et al. 2002, Warner et al. 2003).
- The origins of the unusual behavior with L/L_{edd} (Figures 3 & 4) are not understood, but one implication of this behavior is that metallicity estimates based on trends in emission line ratios involving nitrogen (see Hamann et al. 2002, Warner et al. 2003) show no trend with L/L_{edd}.

Analysis

- We estimate black hole masses by applying the virial theorem to the line emitting gas (Kaspi et al. 2000, Vestergaard 2002, Corbett et al. 2003), in particular C IV λ1549.

$$M_{BH} = 1.4\times10^{6} M_{\odot} \left(\frac{\mathrm{FWHM(CIV)}}{10^{3}\ \mathrm{km\ s^{-1}}}\right)^{2} \left(\frac{\lambda L_{\lambda}(1450\text{Å})}{10^{44}\ \mathrm{ergs\ s^{-1}}}\right)^{0.7}$$

- We estimate L_{bol} as 4.36 $\lambda L_{\lambda}(1450\text{Å})$, based on an integration over a typical quasar continuum shape. We calculate SMBH mass for each quasar using the Eqn. and assume spherical symmetry to obtain

$$L/L_{edd} = 1.59 \left(\frac{\mathrm{FWHM(CIV)}}{10^{3}\ \mathrm{km\ s^{-1}}}\right)^{-2} \left(\frac{L_{bol}}{10^{44}\ \mathrm{ergs\ s^{-1}}}\right)^{0.3}$$

- We then create composite spectra for different ranges in L/L_{edd} (see Figure 1). Calculating composite spectra significantly increases the S/N ratio and averages over object-to-object variations.
- We find that the weak trend in **Figure 2** between L/L_{edd} and z is due to i) a trend for larger L/L_{edd} with increasing L, and ii) a bias for more high L objects at higher redshifts in our sample. Sub-samples spanning narrow ranges in luminosity show no trend between L/L_{edd} and z.

Table 1: Composite Parameters

L/L_{edd}	α	# Objects at C IV	z	Log L_{bol} [ergs s^{-1}]	C IV FWHM [km s^{-1}]	Log M_{BH} [$M_{\odot}$]
0.17	-0.65	64	1.06	46.84	6900	9.48
0.30	-0.56	62	1.17	47.17	5600	9.60
0.41	-0.40	106	1.63	47.16	5300	9.44
0.58	-0.40	85	1.68	47.43	4600	9.56
0.83	-0.60	90	1.93	47.37	3900	9.36
1.38	-0.33	118	2.58	47.63	3400	9.42
3.41	-0.54	45	2.86	47.84	2400	9.26
0.67	-0.93	18	0.06	45.53	2900	7.83

L/L_{edd} is the average Eddington ratio for all objects in each bin. α is the spectral powerlaw index for the continuum fit to each composite spectrum. z is the average redshift and C IV FWHM the average FWHM of C IV for all objects in each bin. Log L_{bol} and Log M_{BH} are the logs of the averages of each quantity for all objects in each bin.

Figure 1: Luminosity vs. C IV FWHM

Distribution of the two measured quantities. The dotted lines represent constant L/L_{edd} ratios, with values indicated at the right. We created composite spectra for each of the seven ranges in Eddington ratio shown above.

Figure 2: Trends with L/L_{edd}

The filled diamonds represent radio-quiet quasars and the open diamonds represent radio-loud quasars. The dashed lines represent slopes from the L/L_{edd} equation (not fits). The positive correlation with L_{bol} and negative correlation with C IV FWHM may be attributed largely to our derivation of L/L_{edd} from these quantities (see Equation).

Figure 3: L/L_{edd} Composites

Composite spectra, sorted by L/L_{edd}, with the mean L/L_{edd} values indicated at the right. The top spectrum is a composite spectrum created only from objects identified in the literature as NLS1s. The horizontal dashed lines and tick marks indicate the normalized continuum and zero flux levels for each composite spectrum.

Figure 4: Equivalent Width vs. L/L_{edd}

The diamonds represent the L/L_{edd} composites and the triangle represents the NLS1 composite. The dotted lines are linear fits to the L/L_{edd} composites, with slopes given to the right.

Figure 5: Other Composites

Normalized composite spectra for different ranges in SMBH mass (top), luminosity (middle), and C IV FWHM (bottom). Dashed lines and tick marks as in Figure 3. All three groups clearly show trends for decreasing line equivalent widths as SMBH mass, luminosity, and C IV FWHM increase. The FWHM group even exhibits this trend despite spanning barely over half an order of magnitude in average luminosity, a much narrower range than in the L/L_{edd} composites (Table 1).

References

[1] Corbett, E. A. et al. 2003, astro-ph/0304541
[2] Croom, S. M. et al. 2002, MNRAS, 337, 275
[3] Dietrich, M., Hamann, F. et al. 2002, ApJ, 581, 912
[4] Hamann, F., Korista, K. T., Ferland, G. J., Warner, C., & Baldwin, J. 2002, ApJ, 564, 592
[5] Kaspi, S. et al. 2000, ApJ, 533, 631
[6] Osterbrock, D. E. 1989, Astrophysics of Gaseous Nebulae and AGNs
[7] Vestergaard, M. 2002, ApJ, 571, 733
[8] Warner, C., Hamann, F., & Dietrich, M. 2003, ApJ, accepted
[9] Woo, J.-H. & Urry, C. M. 2002, ApJ, 579, 530

Acknowledgement: This work was supported by NSF Grant AST 99-84040.

Figure E–2 Poster from the July 2003 “AGN Physics With the SDSS” meeting.

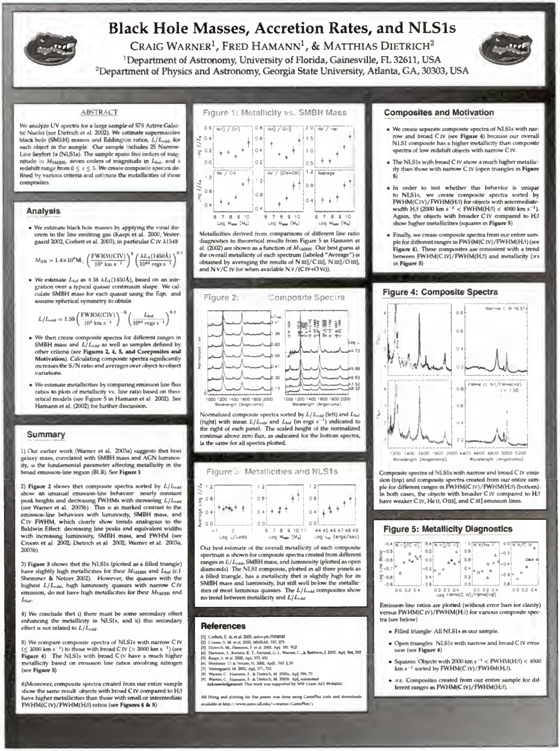

Black Hole Masses, Accretion Rates, and NLS1s

CRAIG WARNER[1], FRED HAMANN[1], & MATTHIAS DIETRICH[2]
[1]Department of Astronomy, University of Florida, Gainesville, FL 32611, USA
[2]Department of Physics and Astronomy, Georgia State University, Atlanta, GA, 30303, USA

ABSTRACT

We analyze UV spectra for a large sample of 578 Active Galactic Nuclei (see Dietrich et al. 2002). We estimate supermassive black hole (SMBH) masses and Eddington ratios, L/L_{edd}, for each object in the sample. Our sample includes 25 Narrow-Line Seyfert 1s (NLS1s). The sample spans five orders of magnitude in M_{SMBH}, seven orders of magnitude in L_{bol}, and a redshift range from $0 \leq z \leq 5$. We create composite spectra defined by various criteria and estimate the metallicities of these composites.

Analysis

- We estimate black hole masses by applying the virial theorem to the line emitting gas (Kaspi et al. 2000, Vestergaard 2002, Corbett et al. 2003), in particular C IV λ1549

$$M_{BH} = 1.4\times10^{6} M_{\odot} \left(\frac{FWHM(CIV)}{10^{3}\ km\ s^{-1}}\right)^{2} \left(\frac{\lambda L_{\lambda}(1450Å)}{10^{44}\ ergs\ s^{-1}}\right)^{0.7}$$

- We estimate L_{bol} as 4.36 $\lambda L_{\lambda}(1450Å)$, based on an integration over a typical quasar continuum shape. We calculate SMBH mass for each quasar using the Eqn. and assume spherical symmetry to obtain

$$L/L_{edd} = 1.59 \left(\frac{FWHM(CIV)}{10^{3}\ km\ s^{-1}}\right)^{-2} \left(\frac{L_{bol}}{10^{44}\ ergs\ s^{-1}}\right)^{0.3}$$

- We then create composite spectra for different ranges in SMBH mass and L/L_{edd} as well as samples defined by other criteria (see **Figures 2, 4, 5, and Composites and Motivation**). Calculating composite spectra significantly increases the S/N ratio and averages over object-to-object variations.
- We estimate metallicities by comparing emission line flux ratios to plots of metallicity vs. line ratio based on theoretical models (see Figure 5 in Hamann et al. 2002). See Hamann et al. (2002) for further discussion.

Summary

1) Our earlier work (Warner et al. 2003a) suggests thet host galaxy mass, correlated with SMBH mass and AGN luminosity, is the fundamental parameter affecting metallicity in the broad emission-line region (BLR). See **Figure 1**

2) **Figure 2** shows thet composite spectra sorted by L/L_{edd} show an unusual emission-line behavior: nearly constant peak heights and decreasing FWHMs with increasing L/L_{edd} (see Warner et al. 2003b). This is in marked contrast to the emission-line behaviors with luminosity, SMBH mass, and C IV FWHM, which clearly show trends analogous to the Baldwin Effect: decreasing line peaks and equivalent widths with increasing luminosity, SMBH mass, and FWHM (see Croom et al. 2002, Dietrich et al. 2002, Warner et al. 2003a, 2003b)

3) **Figure 3** shows thet the NLS1s (plotted as a filled triangle) have slightly high metallicities for their M_{SMBH} and L_{bol} (c.f. Shemmer & Netzer 2002). However, the quasars with the highest L/L_{edd}, high luminosity quasars with narrow C IV emission, do not have high metallicities for their M_{SMBH} and L_{bol}.

4) We conclude thet i) there must be some secondary effect enhancing the metallicity in NLS1s, and ii) this secondary effect is not related to L/L_{edd}.

5) We compare composite spectra of NLS1s with narrow C IV ($\leq$ 3000 km s^{-1}) to those with broad C IV (> 3000 km s^{-1}) (see **Figure 4**). The NLS1s with broad C IV have a much higher metallicity based on emission line ratios involving nitrogen (see **Figure 5**)

6)Moreover, composite spectra created from our entire sample show the same result: objects with broad C IV compared to Hβ have higher metallicities than those with small or intermediate FWHM(C IV)/FWHM(Hβ) ratios (see **Figures 4 & 5**)

Figure 1: Metallicity vs. SMBH Mass

Metallicities derived from comparisons of different line ratio diagnostics to theoretical results from Figure 5 in Hamann et al. (2002) are shown as a function of M_{SMBH}. Our best guess at the overall metallicity of each spectrum (labeled "Average") is obtained by averaging the results of N III]/C III], N III]/O III], and N V/C IV (or when available N V/(C IV+O VI)).

Figure 2: Composite Spectra

Normalized composite spectra sorted by L/L_{edd} (left) and L_{bol} (right) with mean L/L_{edd} and L_{bol} (in ergs s^{-1}) indicated to the right of each panel. The scaled height of the normalized continua above zero flux, as indicated for the bottom spectra, is the same for all spectra plotted.

Figure 3: Metallicities and NLS1s

Our best estimate of the overall metallicity of each composite spectrum is shown for composite spectra created from different ranges in L/L_{edd}, SMBH mass, and luminosity (plotted as open diamonds). The NLS1 composite, plotted in all three panels as a filled triangle, has a metallicity thet is slightly high for its SMBH mass and luminosity, but still well below the metallicities of most luminous quasars. The L/L_{edd} composites show no trend between metallicity and L/L_{edd}

References

[1] Corbett, E. A. et al. 2003, astro-ph/0304541
[2] Croom, S. M. et al. 2002, MNRAS, 337, 275
[3] Dietrich, M., Hamann, F. et al. 2002, ApJ, 581, 912
[4] Hamann, F., Korista, K. T., Ferland, G. J., Warner, C., & Baldwin, J. 2002, ApJ, 564, 592
[5] Kaspi, S. et al. 2000, ApJ, 533, 631
[6] Shemmer O. & Netzer, H. 2002, ApJL, 567, L19
[7] Vestergaard, M. 2002, ApJ, 571, 733
[8] Warner, C., Hamann, F., & Dietrich, M. 2003a, ApJ, 596, 72
[9] Warner, C., Hamann, F., & Dietrich, M. 2003b, ApJ, submitted

Acknowledgement: This work was supported by NSF Grant AST 99-84040.

All fitting and plotting for this poster was done using GatorPlot (info and downloads available at http://www.astro.ufl.edu/~warner/GatorPlot/).

Composites and Motivation

- We create separate composite spectra of NLS1s with narrow and broad C IV (see **Figure 4**) because our overall NLS1 composite has a higher metallicity than composite spectra of low redshift objects with narrow C IV.
- The NLS1s with broad C IV show a much higher metallicity than those with narrow C IV (open triangles in **Figure 5**)
- In order to test whether this behavior is unique to NLS1s, we create composite spectra sorted by FWHM(C IV)/FWHM(Hβ) for objects with intermediate-width Hβ (2000 km s^{-1} < FWHM(Hβ) < 4000 km s^{-1}). Again, the objects with broader C IV compared to Hβ show higher metallicities (squares in **Figure 5**)
- Finally, we create composite spectra from our entire sample for different ranges in FWHM(C IV)/FWHM(Hβ) (see **Figure 4**). These composites are consistent with a trend between FWHM(C IV)/FWHM(Hβ) and metallicity (×s in **Figure 5**)

Figure 4: Composite Spectra

Composite spectra of NLS1s with narrow and broad C IV emission (top) and composite spectra created from our entire sample for different ranges in FWHM(C IV)/FWHM(Hβ) (bottom). In both cases, the objects with broader C IV compared to Hβ have weaker C IV, He II, O III], and C III] emission lines.

Figure 5: Metallicity Diagnostics

Emission-line ratios are plotted (without error bars for clarity) versus FWHM(C IV)/FWHM(Hβ) for various composite spectra (see below)

- Filled triangle: All NLS1s in our sample.
- Open triangles: NLS1s with narrow and broad C IV emission (see **Figure 4**)
- Squares: Objects with 2000 km s^{-1} < FWHM(Hβ) < 4000 km s^{-1} sorted by FWHM(C IV)/FWHM(Hβ).
- ×s: Composites created from our entire sample for different ranges in FWHM(C IV)/FWHM(Hβ).

Figure E–3 Poster from the January 2004 AAS meeting in Atlanta.

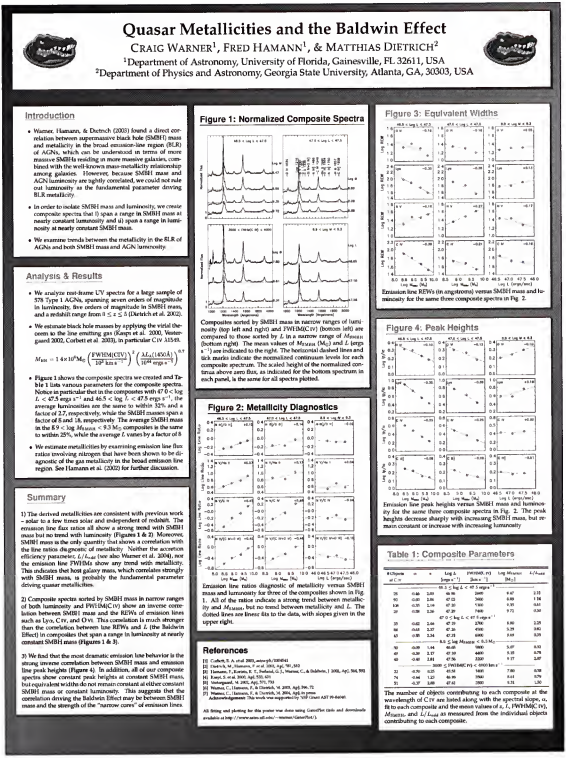

Quasar Metallicities and the Baldwin Effect

CRAIG WARNER[1], FRED HAMANN[1], & MATTHIAS DIETRICH[2]

[1]Department of Astronomy, University of Florida, Gainesville, FL 32611, USA
[2]Department of Physics and Astronomy, Georgia State University, Atlanta, GA, 30303, USA

Introduction

- Warner, Hamann, & Dietrich (2003) found a direct correlation between supermassive black hole (SMBH) mass and metallicity in the broad emission-line region (BLR) of AGNs, which can be understood in terms of more massive SMBHs residing in more massive galaxies, combined with the well-known mass-metallicity relationship among galaxies. However, because SMBH mass and AGN luminosity are tightly correlated, we could not rule out luminosity as the fundamental parameter driving BLR metallicity.
- In order to isolate SMBH mass and luminosity, we create composite spectra that i) span a range in SMBH mass at nearly constant luminosity and ii) span a range in luminosity at nearly constant SMBH mass.
- We examine trends between the metallicity in the BLR of AGNs and both SMBH mass and AGN luminosity.

Analysis & Results

- We analyze rest-frame UV spectra for a large sample of 578 Type 1 AGNs, spanning seven orders of magnitude in luminosity, five orders of magnitude in SMBH mass, and a redshift range from $0 \leq z \leq 5$ (Dietrich et al. 2002).
- We estimate black hole masses by applying the virial theorem to the line emitting gas (Kaspi et al. 2000, Vestergaard 2002, Corbett et al 2003), in particular C IV λ1549.

$$M_{\rm BH} = 1.4\times10^{6}{\rm M}_{\odot}\left(\frac{\rm FWHM(CIV)}{10^{3}\ {\rm km\ s^{-1}}}\right)^{2}\left(\frac{\lambda L_{\lambda}(1450{\rm \AA})}{10^{44}\ {\rm ergs\ s^{-1}}}\right)^{0.7}$$

- Figure 1 shows the composite spectra we created and Table 1 lists various parameters for the composite spectra. Notice in particular that in the composites with $47.0 < \log L < 47.5$ ergs s^{-1} and $46.5 < \log L < 47.5$ ergs s^{-1}, the average luminosities are the same to within 32% and a factor of 2.7, respectively, while the SMBH masses span a factor of 8 and 18, respectively. The average SMBH mass in the $8.9 < \log M_{\rm SMBH} < 9.3$ M$_{\odot}$ composites is the same to within 25%, while the average L varies by a factor of 8.
- We estimate metallicities by examining emission line flux ratios involving nitrogen that have been shown to be diagnostic of the gas metallicity in the broad emission line region. See Hamann et al. (2002) for further discussion.

Summary

1) The derived metallicities are consistent with previous work - solar to a few times solar and independent of redshift. The emission line flux ratios all show a strong trend with SMBH mass but no trend with luminosity (**Figures 1 & 2**). Moreover, SMBH mass is the only quantity that shows a correlation with the line ratios diagnostic of metallicity. Neither the accretion efficiency parameter, $L/L_{\rm edd}$ (see also Warner et al. 2004), nor the emission line FWHMs show any trend with metallicity. This indicates that host galaxy mass, which correlates strongly with SMBH mass, is probably the fundamental parameter driving quasar metallicities.

2) Composite spectra sorted by SMBH mass in narrow ranges of both luminosity and FWHM(C IV) show an inverse correlation between SMBH mass and the REWs of emission lines such as Lyα, C IV, and O VI. This correlation is much stronger than the correlation between line REWs and L (the Baldwin Effect) in composites that span a range in luminosity at nearly constant SMBH mass (**Figures 1 & 3**).

3) We find that the most dramatic emission line behavior is the strong inverse correlation between SMBH mass and emission line peak heights (**Figure 4**). In addition, all of our composite spectra show constant peak heights at constant SMBH mass, but equivalent widths do not remain constant at either constant SMBH mass or constant luminosity. This suggests that the correlation driving the Baldwin Effect may be between SMBH mass and the strength of the "narrow cores" of emission lines.

Figure 1: Normalized Composite Spectra

Composites sorted by SMBH mass in narrow ranges of luminosity (top left and right) and FWHM(C IV) (bottom left) are compared to those sorted by L in a narrow range of $M_{\rm SMBH}$ (bottom right). The mean values of $M_{\rm SMBH}$ (M$_{\odot}$) and L (ergs s^{-1}) are indicated to the right. The horizontal dashed lines and tick marks indicate the normalized continuum levels for each composite spectrum. The scaled height of the normalized continua above zero flux, as indicated for the bottom spectrum in each panel, is the same for all spectra plotted.

Figure 2: Metallicity Diagnostics

Emission line ratios diagnostic of metallicity versus SMBH mass and luminosity for three of the composites shown in Fig 1. All of the ratios indicate a strong trend between metallicity and $M_{\rm SMBH}$, but no trend between metallicity and L. The dotted lines are linear fits to the data, with slopes given in the upper right.

References

[1] Corbett, E. A. et al. 2003, astro-ph/0304541
[2] Dietrich, M., Hamann, F. et al. 2002, ApJ, 581, 512
[3] Hamann, F., Korista, K. T., Ferland, G. J., Warner, C., & Baldwin, J. 2002, ApJ, 564, 592
[4] Kaspi, S. et al. 2000, ApJ, 533, 631
[5] Vestergaard, M. 2002, ApJ, 571, 733
[6] Warner, C., Hamann, F., & Dietrich, M. 2003, ApJ, 596, 72
[7] Warner, C., Hamann, F., & Dietrich, M. 2004, ApJ, in press

Acknowledgement: This work was supported by NSF Grant AST 99-84040.

All fitting and plotting for this poster was done using GatorPlot (info and downloads available at http://www.astro.ufl.edu/~warner/GatorPlot/).

Figure 3: Equivalent Widths

Emission line REWs (in angstroms) versus SMBH mass and luminosity for the same three composite spectra in Fig 2.

Figure 4: Peak Heights

Emission line peak heights versus SMBH mass and luminosity for the same three composite spectra in Fig. 2. The peak heights decrease sharply with increasing SMBH mass, but remain constant or increase with increasing luminosity.

Table 1: Composite Parameters

# Objects at C IV	α	z	Log L [ergs s^{-1}]	FWHM(C IV) [km s^{-1}]	Log $M_{\rm SMBH}$ [M$_{\odot}$]	$L/L_{\rm edd}$
$46.5 \leq \log L < 47.5$ ergs s^{-1}						
25	-0.46	2.03	46.86	2600	8.47	2.11
90	-0.60	2.06	47.03	3600	8.89	1.14
108	-0.35	2.19	47.20	5300	9.35	0.61
29	-0.58	2.26	47.29	7400	9.72	0.30
$47.0 \leq \log L < 47.5$ ergs s^{-1}						
33	-0.62	2.46	47.19	2700	8.80	2.25
84	-0.61	2.37	47.26	4500	9.29	0.82
43	-0.55	2.34	47.31	6900	9.69	0.35
$8.9 \leq \log M_{\rm SMBH} < 9.3$ M$_{\odot}$						
30	-0.09	1.44	46.65	5800	9.07	0.32
49	-0.39	2.17	47.10	4400	9.18	0.75
40	-0.40	2.81	47.56	3200	9.17	2.07
$3000 \leq$ FWHM(C IV) < 4000 km s^{-1}						
22	-0.70	0.25	45.51	3400	7.80	0.38
74	-0.66	1.23	46.99	3500	8.61	0.79
51	-0.37	2.88	47.61	3500	9.31	1.50

The number of objects contributing to each composite at the wavelength of C IV are listed along with the spectral slope, α, fit to each composite and the mean values of z, L, FWHM(C IV), $M_{\rm SMBH}$, and $L/L_{\rm edd}$ as measured from the individual objects contributing to each composite.

Figure E–4 Poster from the June 2004 AAS meeting in Denver.

REFERENCES

Baldwin, J. A. 1977, ApJ, 214, 679

Baldwin, J. A., Hamann, F., Korista, K. T., Ferland, G. J., Dietrich, M., & Warner, C. 2003, ApJ, 583, 649

Becker, R. H., Fan, X., White, R. L., Strauss, M. A., Narayanan, V. K., Lupton, R. H., Gunn, J. E., Annis, J., Bahcall, N. A., Brinkman, J. et al. 2001, AJ, 122, 2850

Begelman, M. C. 2002, ApJ, 568, L97

Bender, R., Burnstein, D., & Faber, S. M. 1993, ApJ, 411, 153

Bettoni, D., Falomo, R., Fasano, G., & Govoni, F. 2003, A&A, 399, 869

Bischof, O. B. & Becker, R. H. 1997, AJ, 113, 2000

Boroson, T. A. 2002, ApJ, 565, 78

Boroson, T. A. 2003, ApJ, 585, 647

Boroson, T. A. & Green, R. F. 1992, ApJS, 80, 109

Boyle, B. J. 1990, MNRAS, 243, 231

Brotherton, M. S., Tran, H. D., Becker, R. H., Gregg, M. D., Laurent-Muehleisen, S. A., & White, R. L. 2001, ApJ, 546, 775

Bruzual, G., Barbury, B., Ortolani, S., Bica, E. & Cuisinier, F. 1997, AJ, 114, 1531

Carroll, S. M., Press, W. H., & Turner, E. L. 1992, ARA&A, 30, 499

Cen, R. & Ostriker, J. P. 1999, ApJ, 519, L109

Collin, S., Boisson, C., Mouchet, M., Dumont, A.-M., Coupé, S., Porquet, D., & Rokaki, E. 2002, A&A, 388, 771

Constantin, A., Shields, J. C., Hamann, F., Foltz, C., & Chaffee, F. 2001, ApJ, 565, 50

Constantin, A. & Shields, J. C. 2003, PASP, 115, 592

Corbett, E. A., Croom, S. M., Boyle, B. J., Netzer, H., Miller, L., Outram, P. J., Shanks, T., Smith, R. J., & Rhook, K. 2003, MNRAS, 343, 705

Crenshaw, D. M., Kraemer, S. B., Turner, T. J., Collier, S., Peterson, B. M., Brandt, W. N., Clavel, J., George, I. M., Horne, K., Kriss, G. A. et al. 2002, ApJ, 566, 187

Croom, S. M., Rhook, K., Corbett, E. A., Boyle, B. J., Netzer, H., Loaring, N. S., Miller, L., Outram, P. J., Shanks, T., & Smith, R. J. 2002, MNRAS, 337, 275

Dickey, J. & Lockman, F. 1990, ARA&A, 28, 215

Dietrich, M., Appenzeller, I., Wagner, S. J., Gässler, W., Häfner, R., Hess, H.-J., Hummel, W., Muschielok, B., Nicklas, H., Rupprecht, G. et al. 1999, A&A, 352, L1

Dietrich, M. & Wilhelm-Erkens, U. 2000, A&A, 354, 17

Dietrich, M., Hamann, F., Shields, J. C., Constantin, A., Vestergaard, M., Chaffee, F., Foltz, C. B., & Junkkarinen, V. T. 2002, ApJ, 581, 912

Dietrich, M., Appenzeller, I., Hamann, F., Heidt, J., Jäger, K., Vestergaard, M., & Wagner, S. J. 2003a, A&A, 398, 891

Dietrich, M., Hamann, F., Shields, J. C., Constantin, A., Heidt, J., Jäger, K., Vestergaard, M., & Wagner, S. J. 2003b, ApJ, 589, 722

Djorgovski, S. G., Castro, S., Stern, D., Mahabal, A. A. 2001, ApJ, 560, L5

Elvis, M., Wilkes, B. J., McDowell, J. C., Green, R. F., Bechtold, J., Willner, S. P., Oey, M. S., Polomski, E., & Cutri, R. 1994, ApJS, 95, 1

Erwin, P., Graham, A. W., & Caon, N. 2002, astro-ph/0212335

Espey, B. R., Lanzetta, K. M., & Turnshek, D. A. 1993, BAAS, 25, 1448

Faber, S. M. 1973, ApJ, 179, 731

Ferland, G. J., Baldwin, J. A., Korista, K. T., Hamann, F., Carswell, R. F., Phillips, M., Wilkes, B., & Williams, R. E. 1996, ApJ, 461, 683

Ferland, G. J., Korista, K. T., Verner, D. A., Ferguson, J. W., Kingdon, J. B., & Verner, E. M. 1998, PASP, 110, 761

Ferrarese, L. & Merritt, D. 2000, ApJ, 539, L9

Ferrarese, L., Pogge, R. W., Peterson, B. M., Merritt, D., Wandel, A., & Joseph, C. L. 2001, ApJ, 555, L79

Ferrarese, L. & Merritt, D. 2002, astro-ph/0206222

Francis, P. J., Hewett, P. C., Foltz, C. B., & Chaffee, F. H. 1992, ApJ, 398, 476

Francis, P. J. & Koratkar, A. 1995, MNRAS, 275, 504

Friaca, A. C. S. & Terlevich, R. J. 1998, MNRAS, 289, 399

Gebhardt, K., Bender, R., Bower, G., Dressler, A., Faber, S. M., Filippenko, A. V., Green, R., Grillmair, C., Ho, L. C., Kormendy, J. et al. 2000a, ApJ, 539, L13

Gebhardt, K., Kormendy, J., Ho, L. C., Bender, R., Bower, G., Dressler, A., Faber, S. M., Filippenko, A. V., Green, R., Grillmair, C. et al. 2000b, ApJ, 543, L5

Gnedin, N. Y. & Ostriker, J. P. 1997, ApJ, 486, 581

Graham, A. W., Erwin, P., Caon, N., & Trujillo, I. 2001, ApJ, 563, L11

Haiman, Z. & Loeb, A. 2001, ApJ, 552, 449

Hamann, F. 1997, ApJS, 109, 279

Hamann, F. & Ferland, G. 1992, ApJ, 391, L53

Hamann, F. & Ferland, G. 1993, ApJ, 418, 11

Hamann, F., Beaver, E. A., Cohen, R. D., Junkkarinen, V., Lyons, R. W., & Burbidge, E. M. 1997, ApJ, 488, 155

Hamann, F., Shields, J. C., Burbridge, E. M., Junkkarinen, V., & Crenshaw, D. M. 1998, ApJ, 496, 761

Hamann, F. & Ferland, G. 1999, ARA&A, 37, 487

Hamann, F., Korista, K. T., Ferland, G. J., Warner, C., & Baldwin, J. 2002, ApJ, 564, 592

Hamann, F., Dietrich, M., Sabra, B., & Warner, C. 2003, astro-ph/0306068

Henry, R. B. C., Edmunds, M. G., & Köppen, J. 2000, ApJ, 541, 660

Idiart, T. P., de Freitas Pacheco, J. A. & Costa, R.D.D. 1996, AJ, 112, 2541

Jablonka, P., Martin, P., & Arimoto, N. 1996, AJ, 112, 1415

Kaspi, S., Smith, P. S., Netzer, H., Maoz, D., Jannuzi, B. T., & Giveon, U. 2000, ApJ, 533, 631

Kellermann, K. I., Sramek, R., Schmidt, M., Shaffer, D. B., & Green, R. 1989, AJ, 98, 1195

Korista, K.T., Alloin, D., Barr, P., Clavel, J., Cohen, R. D., Crenshaw, D. M., Evans, I. N., Horne, K., Koratkar, A. P., Kriss, G. A. et al. 1995, ApJS, 97, 285

Korista, K., Baldwin, J., & Ferland, G. 1998, ApJ, 507, 24

Kormendy, J. & Gebhardt, K. 2001, in The 20th Texas Symposium on Relativistic Astrophysics, eds. H. Martel & J. C. Wheeler (Melville, NY: AIP), 363

Kriss, G. 1994, in ASP Conf. Ser. 61, Astronomical Data Analysis Software and Systems III, eds. D. R. Crabtree, R. J. Hanisch, & J. Barnes (San Francisco: ASP), 437

Krolik, J. 2001, ApJ, 551, 72

Kuraszkiewicz, J., Wilkes, B., Czerny, B., & Mathur, S. 2000, ApJ, 542, 692

Laor, A. 1998, ApJ, 505, L83

Laor, A. 2001, ApJ, 553, 677

Laor, A., Bahcall, J. N., Jannuzi, B. T., Schneider, D. P., Green, R. F., & Hartig, G. F. 1994, ApJ, 420, 110

Laor, A., Jannuzi, B. T., Green, R. F., & Boroson, T. A. 1997, ApJ, 489, 656

Magorrian, J., Tremaine, S., Richstone, D., Bender, R., Bower, G., Dressler, A., Faber, S. M., Gebhardt, K., Green, R., Grillmair, C. et al. 1998, AJ, 115, 2285

Mathur, S. 2000, MNRAS, 314, 17

Marziani, P., Sulentic, J. W., Dultzin-Hacyan, D., Calvani, M., & Moles, M. 1996, ApJS, 104, 37

McLure, R. J. & Dunlop, J. S. 2001, MNRAS, 327, 199

McLure, R. J. & Dunlop, J. S. 2002, MNRAS, 331, 795

McLure, R. J. & Jarvis, M. J. 2002, MNRAS, 337, 109

McWilliam, A. & Rich, R. M. 1994, ApJS, 91, 749

Merritt, D. & Ferrarese, L. 2001, ApJ, 547, 140

National Institute of Standards and Technology Atomic Spectra Database, http://aeldata.phy.nist.gov/PhysRefData/contents-atomic.html

Nelson, C. H. 2000, ApJ, 544, L91

Netzer, H. 2003, ApJ, 583, L5

Netzer, H. & Laor, A. 1993, ApJ, 404, L51

Nussbaumer, H. & Storey, P. J. 1982, A&A, 115, 205

Osmer, P., Porter, A. C., & Green, R. F. 1994, ApJ, 436, 678

Osmer, P. & Shields, J. C. 1999, La Serena Conference on "Quasars and Cosmology", eds. G. Ferland & J. Baldwin (San Francisco: ASP), 235

Osterbrock, D. E. & Pogge, R. W. 1985, ApJ, 297, 166

Osterbrock, D. E. 1989, Astrophysics of Gaseous Nebulae and Active Galactic Nuclei (Sausalito, California: University Science Books)

Ostriker, J. & Gnedin, O. 1997, ApJ, 487, 667

Peterson, B. M. 1993, PASP, 105, 247

Peterson, B. M. 1997, An Introduction to Active Galactic Nuclei (Cambridge: Cambridge University Press)

Peterson, B. M. 2001 in Advanced Lectures on the Starburst-AGN Connection, eds. I.Aretxaga, D. Kunth, R. Mújica (Singapore: World Scientific), 3

Peterson, B. M. & Wandel, A. 1999, ApJ, 521, L95

Peterson, B. M. & Wandel, A. 2000, ApJ, 540, L13

Petitjean, P., Rauch, M., & Carswell, R. F. 1994, A&A, 291, 29

Pettini, M. 2001 in The Promise of FIRST, eds. G.L. Pillbratt, J. Cernicharo, A.M. Heras, T.Prusti, & R. Harris (ESA SP-460; Noordwjik: ESA), 113

Pettini, M., Ellison, S. L., Bergeron, J., & Petitjean, P. 2002, A&A, 391, 21

Pilyugin, L. S. 2003, A&A, 399, 1003

Pilyugin, L. S., Mollá, M., Ferrini, F., & Vílchez, J. M. 2002, A&A, 383, 14

Pilyugin, L. S., Thuan, T. X., & Vilchez, J. M. 2003, A&A, 397, 487

Rees, M. J. 1984, ARA&A, 22, 471

Shang, Z., Wills, B. J., Robinson, E. L., Wills, D., Laor, A., Xie, B., & Yuan, J. 2003, ApJ, 586, 52

Shemmer, O. & Netzer, H. 2002, ApJ, 567, L19

Shemmer, O., Netzer, H., Maiolino, R., Oliva, E., Croom, S., & Corbett, E. 2003 in AGN Physics with the Sloan Digital Sky Survey, eds. G. T. Richards & P. B. Hall (San Francisco: ASP), 407

Shemmer, O., Netzer, H., Maiolino, R., Oliva, E., Croom, S., Corbett, E., & di Fabrizio, L. 2004, astro-ph/0406559

Shields, G. A. 1976, ApJ, 204, 330

Shields, G. A., Gebhardt, K., Salviander, S., Wills, B. J., Xie, B., Brotherton, M. S., Yuan, J., & Dietrich, M. 2003, ApJ, 583, 124

Steidel, C. C., Hunt, M. P., Shapley, A. E., Adelberger, K. L., Pettini, M., Dickinson, M., & Giavalisco, M. 2002, ApJ, 576, 653

Stern, D., Djorgovski, S. G., Perley, R. A., de Carvalho, R. R., & Wall, J. V. 2000, AJ, 119, 1526

Stirpe, G. M, Winge, C., Altieri, B., Alloin, D., Aguero, E. L., Anupama, G. C., Ashley, R., Bertram, R., Calderon, J. H., Catchpole, R. M. et al. 1994, ApJ, 425, 609

Storrie-Lombardi, L. J., McMahon, R. G., Irwin, M. J., & Hazard, C. 1996, ApJ, 468, 121

Telfer, R. C., Zheng, W., Kriss, G. A., & Davidsen, A. F. 2002, ApJ, 565, 773

Trager, S. C., Faber, S. M., Worthey, G., & Gonzalez, J. J. 2000, AJ, 120, 165

Tremaine, S., Gebhardt, K., Bender, R., Bower, G., Dressler, A., Faber, S. M., Filippenko, A. V., Green, R., Grillmair, C., Ho, L. C. et al. 2002, ApJ, 574, 740

Tinsley, B. 1980, Fundam. Cosmic Physics, 5, 287

van Albada, T. S., Bertin, G., & Stiavelli, M. 1995, MNRAS, 276, 1255

van Zee, L., Salzer, J. J., & Haynes, M. P. 1998, ApJ, 497, L1

Vanden Berk, D. E., Richards, G. T., Bauer, A., Strauss, M. A., Schneider, D. P., Heckman, T. M., York, D. G., Hall, P. B., Fan, X., Knapp, G. R. et al. 2001, AJ, 122, 549

Verner, E. M., Verner, D. A., Korista, K. T., Ferguson, J. W., Hamann, F., & Ferland, G. J. 1999, ApJS, 120, 101

Véron-Cetty, M.-P. & Véron, P. 2001, A Catalogue of Quasars and Active Nuclei, 10th edition

Vestergaard, M. 2002, ApJ, 571, 733

Vestergaard, M. 2004, ApJ, 601, 676

Vestergaard, M. & Wilkes, B. J. 2001,ApJS, 134, 1

Vila-Costas, M. B. & Edmunds, M. G. 1993, MNRAS, 265, 199

Wandel, A. 1999, ApJ, 519, L39

Wandel, A., Peterson, B. M., & Malkan, M. A. 1999, ApJ, 526, 579

Wang, T. & Lu, Y. 2001, A&A, 377, 52

Wang, J-M. 2003, AJ, 125, 2859

Warner, C., Hamann, F., Shields, J. C., Constantin, A., Foltz, C., & Chaffee, F. 2002, ApJ, 567, 68

Warner, C., Hamann, F., & Dietrich, M. 2003, ApJ, 596, 72

Warner, C., Hamann, F., & Dietrich, M. 2004, ApJ, 608, 136

Wheeler, J. C., Sneden, C., & Truran, J. W. 1989, ARA&A, 27, 279

Wills, B. J., Brotherton, M. S., Fang, D., Steidel, C. C., & Sargent, W. L. W. 1993, ApJ, 415, 563

Wills, B. J., Thompson, K. L., Han, M., Netzer, H., Wills, D., Baldwin, J. A., Ferland, G. J., Browne, I. W. A., & Brotherton, M. S. 1995, ApJ, 447, 139

Wilkes, B. J. 1984, MNRAS, 207, 73

Wilkes, B. J., Kuraszkiewicz, J., Green, P. J., Mathur, S., & McDowell, J. C. 1999, ApJ, 513, 76

Woo, J-H. & Urry, M. 2002, ApJ, 579, 530

Worthey, G., Faber, S. M. & Gonzalez, J. 1992, ApJ, 398, 69

Zaritsky, D., Kennicutt, R. C., & Huchra, J. P. 1994, ApJ, 440, 606

Zheng, W. & Malkan, M. A. 1993, ApJ, 415, 517

Zheng, W., Kriss, G. A., Telfer, R. C., Grimes, J. P., & Davidsen, A. F. 1997, ApJ, 475, 469

BIOGRAPHICAL SKETCH

I was born in Albuquerque, NM, and grew up in Clemson, SC, where I attended Seneca High School. I passed the BC level AP calculus exam my junior year of high school and took math and physics classes at Clemson University during my senior year. I was awarded a National Merit scholarship and decided to attend the University of Florida. I have always been interested in astronomy and have enjoyed programming computers ever since I got a Commodore 64 when I was six years old. I decided to pursue a degree in astrophysics because it combines these two interests. While I was at home during summers, I performed research on high mass stellar evolution models and gamma ray bursters for Brad Meyer and Mark Leising at Clemson University. I also developed softare in the IDL programming language and interactive web pages using java and javascript. I graduated from the University of Florida with a dual major in astronomy and physics in three years and decided to stay at UF for graduate school. The summer after my first year of graduate school, I started working with Fred Hamann, performing research on quasars. Quasars have always interested me because they allow us to study the universe when it was very young. While performing my research, I concurrently developed GatorPlot, my own software package. GatorPlot is written in IDL and performs every task I needed to do throughout my research. I received my M.S. degree in December 2002 with a major in astronomy and a minor in computer science, and will receive my Ph.D. in August 2004. I plan on pursuing a career as a software engineer. When I'm not doing research, I enjoy playing sports, watching sports (especially when the Gators are playing), programming computers, and hanging out and having a few beers with my friends.

I certify that I have read this study and that in my opinion it conforms to acceptable standards of scholarly presentation and is fully adequate, in scope and quality, as a dissertation for the degree of Doctor of Philosophy.

Fred Hamann, Chair
Professor of Astronomy

I certify that I have read this study and that in my opinion it conforms to acceptable standards of scholarly presentation and is fully adequate, in scope and quality, as a dissertation for the degree of Doctor of Philosophy.

Vicki Sarajedini

Vicki Sarajedini
Assistant Professor of Astronomy

I certify that I have read this study and that in my opinion it conforms to acceptable standards of scholarly presentation and is fully adequate, in scope and quality, as a dissertation for the degree of Doctor of Philosophy.

Rafael Guzman
Associate Professor of Astronomy

I certify that I have read this study and that in my opinion it conforms to acceptable standards of scholarly presentation and is fully adequate, in scope and quality, as a dissertation for the degree of Doctor of Philosophy.

Gary Ihas
Professor of Physics

I certify that I have read this study and that in my opinion it conforms to acceptable standards of scholarly presentation and is fully adequate, in scope and quality, as a dissertation for the degree of Doctor of Philosophy.

Beverly Sanders
Associate Professor of Computer and
Information Science and Engineering

This dissertation was submitted to the Graduate Faculty of the Department of Astronomy in the College of Liberal Arts and Sciences and to the Graduate School and was accepted as partial fulfillment of the requirements for the degree of Doctor of Philosophy.

August 2004

Kenneth J. Gerhardt
Interim Dean, Graduate School

BLACK HOLE MASSES, METALLICITIES, AND EMISSION LINE PROPERTIES OF QUASARS

Craig D. Warner
(352) 392-2052 x230
Department of Astronomy
Chair: Fred Hamann
Degree: Doctor of Philosophy
Graduation Date: August 2004

Quasars are among the brightest and most distant objects in the universe. They consist of a supermassive black hole at their center, surrounded by a disk of matter spiralling inward and clouds of gas. Studying quasars allows us to see the universe when it was very young because the light that we observe left the quasar billions of years ago. All elements heavier than helium can only be created in stars, so measuring the abundances of these elements in quasars can give us an idea of when the first stars must have started forming. In addition, I estimate the black hole masses of quasars. I conclude that a quasar's black hole mass plays a critical role in determining many properties of the quasar, including the amount of elements heavier than helium in the gas clouds surrounding the quasar and the intensity of the light emitted from specific elements within these gas clouds.